A Numerical Study of a Double Pipe Latent Heat Thermal Energy Storage System

by

Tonny Tabassum

Thesis submitted to the McGill University in Partial fulfillment of the requirements for the degree of **Master of Engineering**

Department of Mining and Materials Engineering
3610 University Street, M. H. Wong Building
McGill University
Montréal, Canada. H3A 2B2

ABSTRACT

Solar energy is an intermittent supply source of energy. To efficiently utilize this free renewable energy source some form of thermal energy storage devices are necessary. Phase change materials (PCMs), because of their high energy density storage capacity and near isothermal phase change characteristics, have proven to be promising candidates for latent heat thermal energy storage (LHTES) devices. Among the various LHTES devices for low temperature residential heating and cooling applications, the shell-and-tube type heat exchanging devices are the most simple to operate and can be easily fabricated. This work numerically investigates the buoyancy driven heat transfer process during melting (charging) of a commercial paraffin wax as PCM filling the annulus of a horizontal double pipe heat exchanger. The heated working fluid (water) is passing through the central tube of the annulus at a sufficiently high flow-rate and thereby maintaining an almost isothermal wall temperature at the inner pipe which is higher than the melting temperature of the PCM. The transient, two-dimensional coupled laminar momentum and energy equations for the model are suitably non-dimensionalized and are solved numerically using the enthalpy-porosity approach. Time-wise evolutions of the flow patterns and temperature distributions are presented through velocity vector fields and isotherm plots. In this study, two types of PCM filled annuli, a plain annulus and a strategically placed longitudinal finned annulus, are studied. The total energy stored, the total liquid fraction and the energy efficiency at different melting times are evaluated for three different operating conditions and the results are compared between the plain and finned annuli. The present study will provide guidelines for system thermal performance and design optimization of the shell-and-tube LHTES devices.

.

Résumé

L'énergie solaire est une source d'alimentation d'énergie intermittente. Pour utiliser efficacement cette source gratuite d'énergie renouvelable, une certaine forme de dispositifs de stockage d'énergie thermique est nécessaire. Les matériaux à changement de phase (PCMs) en raison de leur capacité d'énergie à haute densité de stockage et les caractéristiques quasi isothermes de changement de phase se sont révélés être des candidats prometteurs pour les dispositifs de stockage de la chaleur latente de l'énergie thermique (LHTES). Parmi les différents dispositifs LHTES pour le chauffage résidentiel à basse température et les utilisations possibles comme refroidissant, les dispositifs d'échange de chaleur du type à tubes et calandre[1] et les dispositifs de type à tubes sont les plus simples à faire fonctionner et peuvent être facilement fabriqués. Ce travail étudie numériquement le processus de flottabilité piloté par le transfert de chaleur lors de la fusion (stockage de la chaleur) d'une cire de paraffine commerciale utilisée comme PCM remplissant l'espace annulaire d'un échangeur de chaleur horizontal à double conduit. Le fluide chauffé (de l'eau) faisant action passe par le conduit central de l'espace annulaire à un débit suffisamment élevé et maintient ainsi une température quasi isotherme de la paroi du conduit intérieur qui est supérieure à la température de fusion du PCM. La dynamique laminaire couplée à deux dimensions et les équations énergétiques transitoires du modèle sont convenablement dédimensionnées et sont résolues numériquement en utilisant l'approche enthalpie-porosité. Les évolutions selon le facteur temps des modèles d'écoulement et des distributions de température sont présentées par des champs vectoriels de vitesse et des courbes isothermiques. Dans cette étude, deux types d'espaces annulaires remplis de PCM, un espace annulaire simple et un espace annulaire longitudinal à ailettes stratégiquement placé, sont étudiés. L'énergie totale stockée, la fraction totale de liquide et le rendement énergétique à des moments différents de fusion sont évalués pour trois différentes conditions de fonctionnement et les résultats sont comparés entre les espaces annulaires simples et ceux à ailettes. La présente étude fournira des lignes directrices pour la performance thermique du système et l'optimisation de la conception des dispositifs LHTES à tubes et calandre.

ACKNOWLEDGEMENTS

My deepest appreciation is extended to my thesis supervisor, Professor Mainul Hasan for his illuminating teaching, constant encouragement and invaluable help throughout the course of this research. I am truly indebted to him for introducing and teaching me the field of computational fluid dynamics. What I have learned from him through our numerous discussions is immeasurable. The time which my supervisor has spent in reviewing various chapters of my thesis is well acknowledged.

I would like to thank my husband Mr. Muhammad Mahbubur Rahman for his sacrifices, unfailing support and unwavering faith without which this work would not have been possible. My mother provided me with love, admiration and continuous mental support during my study period. Without her continuous inspiration it would have been almost impossible for me to pursue an M.Eng degree at McGill University. My father gave me courage and strength to follow my dream. With my everlasting gratitude, I dedicate this thesis to them as a token of my eternal indebtedness.

Contents

CHAPTER ONE: Introduction

CHAPTER TWO: Literature Survey

CHAPTER THREE: Mathematical Formulation and Numerical Approach

CHAPTER FOUR: Melting of a Commercial PCM in a plain horizontal cylindrical annulus

CHAPTER FIVE: Melting of a Commercial PCM in a finned annulus

CHAPTER SIX: Concluding remarks and suggestions for future work

List of Figures

CHAPTER ONE

CHAPTER THREE

CHAPTER FOUR

CHAPTER FIVE

List of Tables

NOMENCLATURE

Symbol	Description
A	Darcy coefficient
a_P	coefficient in the discretized governing equation
C_P	specific heat of the phase-change material, kJ.kg^{-1}.^{0}C^{-1}
D_e, D_w, D_n, D_s	diffusive conductance
F_e, F_w, F_n, F_s	strength of convection
g	gravitational acceleration, m. s^{-2}
h	sensible heat
H	fin height
k_f	fluid thermal conductivity, W.m^{-1}.^{0}C^{-1}
k_s	solid thermal conductivity, W.m^{-1}.^{0}C^{-1}
K_{eq}	local equivalent thermal conductivity = $\frac{Nu_L}{Nu_o}$
$\bar{K}_{eq_{inner}}$	Circumferential average equivalent thermal conductivity = $\frac{\bar{Nu}}{Nu_0}$
L	gap width of the annulus = ($r_o - r_i$) , m
Nu_0	Nusselt number for conduction between the annuli
Nu_L	local Nusselt number
$\bar{Nu}$	Circumferential average Nusselt number based on cylinder radius
P	pressure, Pa
Pr	Prandtl number = $\frac{\nu_f}{\alpha_f}$
r_i	radius of inner cylinder, m
r_o	radius of outer cylinder, m

R_i dimensionless radius of inner cylinder

R_o dimensionless radius of outer cylinder

Ra Rayleigh number = $\dfrac{g\beta_{PCM}(T_{WALL}-T_{SOLIDUS})D_i^3\rho}{\mu_{PCM}\alpha_{PCM}}$

Ra^* modified Rayleigh number = $\dfrac{Ra}{Ste}$

Ste Stefan number = $\dfrac{C_P(T_{WALL}-T_{SOLIDUS})}{\lambda}$

T temperature, ^{0}C

T_{WALL} inner cylinder wall temperature, ^{0}C

T_i initial temperature of the working materials, ^{0}C

ΔT temperature difference between the inner cylinder surface and solidus temperature of PCM, ^{0}C

T_{ref} reference temperature, ^{0}C

t time

h^* = Dimensionless enthalpy = $\dfrac{C_P(T-T_{SOLIDUS})}{\lambda}$

h^*_{WALL} dimensionless enthalpy at the inner wall

h^*_i initial dimensionless enthalpy in the domain

u, v interstitial velocity components along θ and r directions respectively, ms^{-1}

U, V dimensionless interstitial velocity components along θ and r directions respectively

θ , r Polar coordinates, degree and m

Greek symbols

α thermal diffusivity, m^2s^{-1}

β_f coefficient of thermal expansion, $-\left(\dfrac{1}{\rho}\right)\left(\dfrac{\partial\rho}{\partial T}\right)_P$, K^{-1}

ν_f	kinematic viscosity, m^2s^{-1}
ρ	density, $kg.m^{-3}$
μ	dynamic viscosity, $kg.m^{-1}.s^{-1}$
λ	latent heat of fusion , $kJ.kg^{-1}$
ΔH	nodal latent heat
F_o	Fourier number, $\frac{t\alpha_{PCM}}{D_i^2}$
f_l	fluid fraction

Subscripts

e, w, n, s	four surfaces of control volume centred at P
E,W,N,S,NE,NW,SE,SW	eight adjacent nodes to P
nb	neighbouring points in numerical molecule
P	nodal point to be solved in difference equation

eff	effective
L	liquid
s	solid
i	inner cylinder
o	outer cylinder
ref	reference value
f	fluid (PCM)

CHAPTER – ONE

Introduction

1.1 Introduction

Latent Heat Thermal Energy Storage (LHTES) devices have attracted considerable attention worldwide because of their large potential for energy savings and their ability to provide or absorb relatively large amount of thermal energy particularly, when there is a mismatch in the supply and demand of the energy sources (Dincer and Rosen, 2002). Any LHTES system mainly has three basic components: (a) a phase change material (PCM), (b) a suitable container to hold the PCM and (c) a conductive heat transfer surface or surfaces for exchanging heat from the heat source to the PCM and from the latter to the heat sink (Lacroix, 1993a, 1993b). One of the most popular heat exchanging devices for LHTES is a double-pipe heat exchanger. The latter stores/discharges thermal energy through the phase change process by melting (charge)/solidification (discharge) of a PCM embedded in the annulus gap of the double-pipe heat exchanger (Padmanahdan, 1986; Zang and Faghri, 1996; Sari and Kaygusuz, 2001, 2002). The thermal storage technology based on the use of PCMs has recently attracted an important practical interest because of its capacity to store relatively large amount of thermal energy through the solid-liquid phase-change process (Regin et al., 2008). Intermittent energy generation sources, such as solar and waste heat from industrial processes can be stored and later conveniently used through the LHTES devices. Because of their high storage capacity, these devices are advantageous in reducing thermal energy storage volume, heat loss and insulation cost.

A pure PCM with a high latent heat of fusion is capable of storing/releasing a large amount of energy during melting/solidification at a certain temperature. If the PCM is impure or is a reagent grade, it will melt and solidify over a temperature range. Thus, during the transient phase-change process there will be solid, liquid and mushy regions (mixture of solid and liquid) in the LHTES systems. The main criterion of selection of a PCM for a particular application is the melting temperature or the phase change temperature range of the PCM. Some other important parameters must also be taken into consideration for an appropriate usage of LHTES systems. These are: latent heat, stability to thermal cycling, and thermal conductivity. An extensive overview of PCMs used in low thermal energy systems has been given by Abhat (1983), Zalba et al. (2003), Farid et al. (2004).

With regard to latent heat applications with PCMs, the applications can be classified into two main areas: (a) protection or thermal inertia and (b) thermal energy storage. One main difference between these two areas is related to the PCM thermal conductivity. Low thermal conductivity is desirable for the thermal protection field. On the other hand, for thermal storage systems low thermal conductivity values of the PCMs are disadvantageous. In the latter applications if the thermal conductivity of a PCM is low then an adequate amount of energy may be available but the system may not be able to use it at the required rate. With regard to the low thermal conductivity problem of PCM, several ideas and systems have been proposed in the literature to enhance the heat transfer rate In this regard, several studies are available in the literature concerning the improvements of the thermal conductivity of the PCMs for thermal energy storage devices. Among the various ideas for heat transfer enhancement in LHTES systems, one of the ideas is to use tubes attached with fins and placed in embedded PCMs in different geometrical configurations (Sparrow et al., 1981; Smith and Koch, 1982; Eftekhar et al., 1984; Chow et al., 1996; Velraj et al., 1997, 1999; Ismail et al., 2001; Jegadheeswaran and Pokehar, 2009). .

Figure-1.1 presents heat storage capacity per kg for some sensible heat storage materials and a PCM where it is seen that the PCM is the one with the highest heat storage capacity compared to the sensible heat storage materials (such as water, stone, wood, and plastic). As it is mentioned before, due to the phase change a large amount of latent heat can be stored during solid-liquid phase transition of the PCM. A PCM, such as paraffin wax, offers four to five times higher heat capacity by volume or mass, than water at low operating temperature differences because of the latent heat transfer during phase transition (Farid et al., 2004). The saturated hydrocarbon series from $C_{14}H_{30}$ to $C_{40}H_{82}$ exhibits a suitable melting temperature range from 6^0C to 80^0C which is beneficial for domestic heating and cooling applications. The hydrocarbon compounds with more than 15 carbon atoms per molecule are waxy solids at room temperature. These hydrocarbons, popularly known as paraffin wax, are suitable for LHTES systems due to the following desirable characteristics:

1. High heat of fusion
2. Low melting point temperature
3. Show little volume changes on melting
4. Have low vapor pressure
5. It is safe, less expensive and non-corrosive

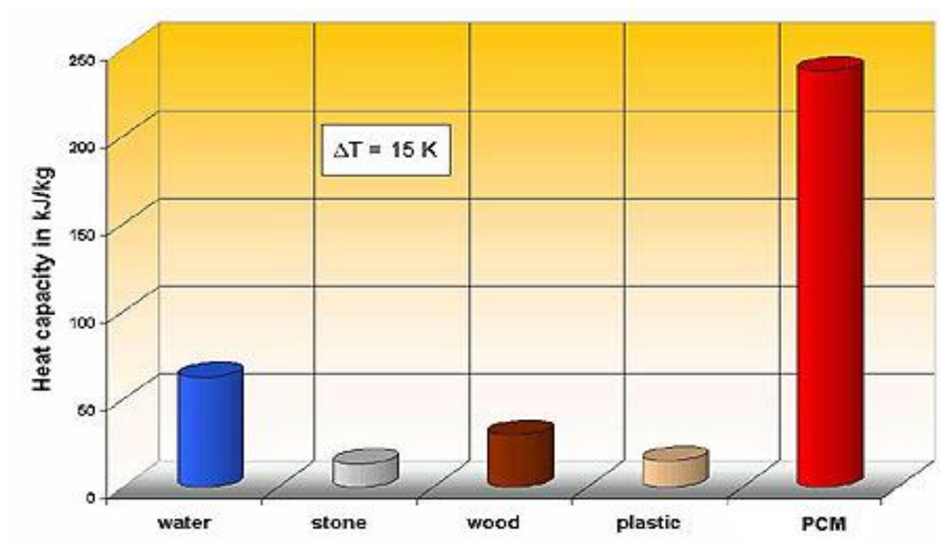

Figure 1.1: Heat capacity (kJ/kg) for different materials at ΔT=15 K.

Source: web.mit.edu/3.082/www/team2_s02/background.html

In selecting a paraffin wax its melting temperature has to be matched to the operating temperature of the solar energy storage system. A paraffin wax with a low melting point (within 60^{0}C) is of interest for solar energy storage system. Now, there is renewed interest in the usage of solar energy due to the fact that the price of non-renewable energy sources has recently sky-rocketed. Solar energy is one of the green types of energy for the following reasons:

a) It causes no air pollution whatsoever.

b) Energy from the sun is free.

c) Solar energy systems are technologically safe and easy to operate.

Solar energy is considered as an important renewable energy source globally. Recently the European parliament has passed a resolution recommending to all member countries to introduce legislation mandating the use of solar thermal systems in all new residential buildings **(source: http://www.greensunrising.com/thermal.htm)**. There is a broad consensus among solar energy researchers that in future forty to fifty percent of the annual hot water needs of a house-hold could be met from solar energy.

1.2 Proposed solar system for domestic hot water

Figure 1.2 presents a proposed latent heat storage arrangement from solar energy which can be used for domestic hot water supply source. The system consists of the following main components: (a) a flat plate collector, (b) a double-pipe LHTES heat exchanger, and (c) an insulated storage tank.

The flat plate collector can be placed on the top of a building or any other suitable structure which absorbs directly both the solar beam and the diffuse radiation. It can be used to absorb solar energy, convert it into heat and then to transfer that heat to the circulating cold water. The heated water (heat transfer fluid, HTF) passes through the inner pipe of the double-pipe heat exchanger to store the heat by melting a PCM placed in the annulus gap. During the charging phase, pump-1 and control valves 1, 3, 5 and 7 are open while pump-2 is inactive and valves 2, 4, 6 and 8 are closed. This flow control loop, named as an inner loop, should only work when the solar energy is available. When the solar energy is not available pump-2 is active and will circulate cold water from the insulated storage tank through the outer loop connecting the heat exchanger and the insulated storage tank. In this discharge period, while passing through the LHTES device, the circulating cold water in the outer loop will gain heat from the melted PCM by solidifying it. During this time, pump-1 is idle and control valves 1, 3, 5 and 7 are closed while pump-2 is active and valves 2, 4, 6 and 8 are opened. Here all the connecting pipes used between (a) collector and the heat exchanger and (b) the heat exchanger to the insulated storage tank are insulated and there is a minimum heat loss. Thus, there will be a minimum temperature drop for hot water flowing through the system. The inner loop and outer loop do not work simultaneously which should be controlled by an automatic control unit. In the insulated storage tank an electric heater can be placed as back up for low solar radiation or for overcast/rainy days or for night time. There could be a number of possible variations of the proposed solar energy storage and utilization facility.

As one can see, one of the important units in the proposed system is the heat exchanger. So, designing an optimum double pipe heat exchanger is important for thermal energy efficiency of a solar energy storage unit. The mathematical modeling is a justifiable option for designing an optimum LHTES device without performing a number of experimental runs. Thus, such a modeling exercise can save both energy and cost.

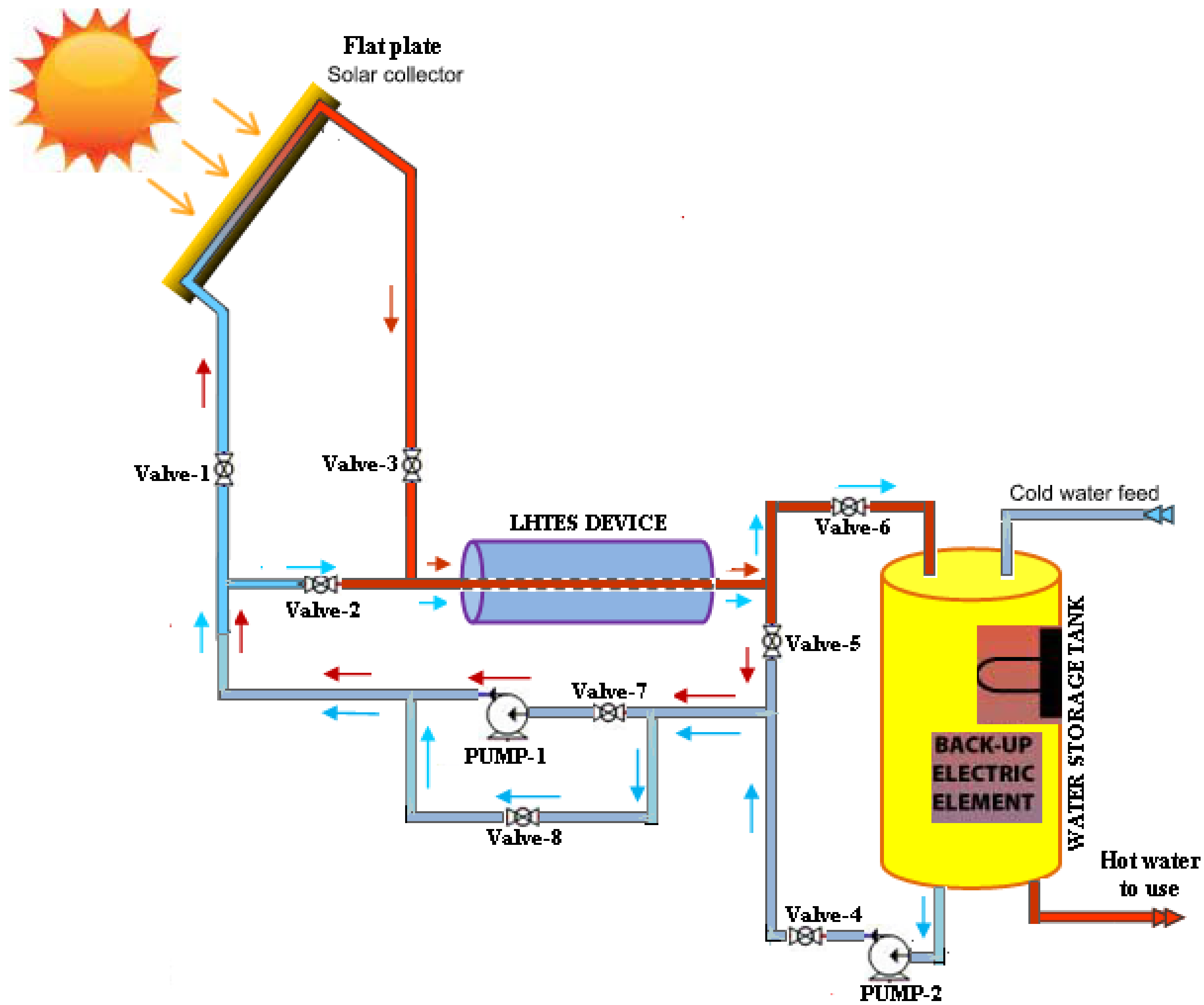

Figure 1.2: Schematic view of solar energy storage system for domestic hot water.

Melting of a PCM usually gives rise to natural convection and this significantly changes the flow patterns and affects the heat transfer process. The essential feature of melting of a pure PCM is the existence of a liquid-solid moving interface between liquid and solid phases which propagates with time (Hale and Viskanta, 1980; Reiger et al., 1982; Adetutu and Prasad, 1992). The convection influences the morphology of this liquid- solid interface. In 1831, Lame and Clapeyron (Viskanta, 1985) studied this problem. Later on, the author Stefan (Hu and Argyropoulos, 1996) mathematically analyzed these types of problems and hence after the phase-change moving boundary problems are known by the general name as “Stefan problem”. The problem of heat transfer with phase change can be formulated, considering either the temperature or enthalpy as the dependent variable (Voller and Swaminathan, 1991). When temperature is considered as dependent variable, the energy equations are to be written independently for both phases but these equations are coupled because of the interface energy balanced condition. In fact this technique applies only for pure PCM and requires *a priori* knowledge about the interface position for the determination of temperature, which makes the solution method more complicated. The moving boundary heat transfer problems can be relatively easily solved by the enthalpy-porosity method originally proposed by Voller and co-workers (Voller and Prakash, 1987; Brent et al., 1988; Swaminathan and Voller, 1993; 1997). For the heat transfer problems when the enthalpy is considered as the dependent variable, *a priori* knowledge about the interface position is not required and a single enthalpy equation for the whole domain suffices. Numerical solution of melting of a commercial PCM inside a fixed domain is a more complicated problem due to the existence of three phases such as solid, liquid and mushy regions. It is a challenge to adopt the enthalpy-porosity formulation to track the mushy region at every time instant particularly in the presence of natural convection. There seems to have no numerical work reported in the literature which has modeled the melting of a commercial PCM embedded inside a horizontal concentric annulus. Also, a thorough search of the pertinent literature did not reveal any work on a double-pipe LHTES system where the inner pipe is fitted with strategically placed high conductivity longitudinal fins.

1.3 Objectives of the Present Work

Fundamental understanding of phase change heat transfer processes that occur during the melting of a PCM is crucial in designing more practical and efficient thermal energy storage devices. The objective of this study is to develop a 2D mathematical model to study the melting and thermal energy storage characteristics of a reagent grade PCM in a horizontal double-pipe LHTES system. The purpose of using a commercial paraffin wax (reagent grade) in the model, as opposed to the pure paraffin wax (technical grade), is the fact that the former is relatively less expensive and is easily available compared to the latter one. The specific objectives of this research are the following:

1. Model the melting process of a commercial PCM placed in the annulus of a double-pipe LHTES exchanger.

2. Predict the velocity and temperature fields, as well as the melt fraction, the total energy stored and the energy storage efficiency of the LHTES system.

3. Model the melting characteristics of a PCM in the LHTES with strategically placed longitudinal fins.

4. Compare the energy storage capacity and thermal efficiency of the plain versus finned LHTES exchangers.

CHAPTER – TWO

Literature survey

2.1 Introduction

In this section, a detailed review of the previous work which is related to the current research is presented. A large number of theoretical and numerical investigations exist in the literature concerning the heat transfer and melting characteristics of various PCMs in LHTES systems (Chung and Yoo, 1997; Devahastin and Mujumdar, 1998; Gong and Mujumdar, 1998; Mbaye and Bilgen, 2001; Liu and Mah, 2002). The majority of the previous numerical studies focused on melting of pure PCMs. But in reality wrought commercial PCMs are much less costly than pure PCMs and the former are easily available and convenient to use. The behavior of a commercial PCM during melting and solidification are totally different than from a pure PCM and this is primarily because of the existence of a mushy region. In this chapter, a critical review of the relevant published work is provided. A closure is also provided at the end of this chapter outlining the gap in the field and it also discusses about the attempt made in this thesis to fill this gap.

2.2 Previous work

Before reviewing the relevant literature, the critical problem of modeling the melting characteristics in an annulus should be explained first. Earlier studies on natural convection of a single phase fluid in a concentric horizontal cylindrical annulus reveal that the flow disturbances are generated by the hydrodynamic instability for small Prandtl number fluids, while by the thermal instability for large Prandtl number fluids (Rao et al., 1985; Fant et al., 1990; Vafai and Ettefagh, 1991; Cheddadi et al., 1992; Kim and Rao, 1994;). The flow disturbances cannot be observed when the Rayleigh number is very small. Two-cell or three-cell flow patterns at high Rayleigh numbers have been observed to form during the initial stage of melting. For a melting of a PCM in a confined geometry, the Rayleigh number can't be changed arbitrarily, since the Rayleigh number depends on the characteristic dimension of the geometry, the boundary conditions imposed on the inner cylinder wall for two horizontal concentric cylinders and the melting temperature and thermo-physical properties of the PCM. To predict numerically the actual heat transfer phenomenon inside the annulus, a transient study must be undertaken where for a particular working fluid, one can estimate the Rayleigh number *a priori*. So, the critical problem is the thermal instability which can arise due to the use of a high Prandtl number PCM (Viskanta, 1985).

Ho and Lin (1986) numerically investigated the two-dimensional melting process of a pure PCM (n-octadecane), contained in a horizontal cylindrical annulus for laminar flow. The inner surface of the annulus acted as the thermal energy source, while the outer surface of the annulus acted as a heat sink for the extraction of thermal energy, which means both outward melting in the presence of both natural convection in the liquid and sub0cooling effect in the un-melted solid had been considered in their simulations. The finite-difference analog of the governing equations were derived by using a forward time, central-space difference scheme for the partial derivatives in the governing equations except for the convective terms for which the hybrid central/upwind difference scheme was employed. The movement of the irregular liquid-solid interface was evaluated explicitly from the energy balance conditions across the interface. A grid distribution of 21 x 21 grids was employed for each of the solid and liquid phase region. The radius ratio of the annulus was varied from 1.6 to 3.0. The simulations were carried out for a fixed Prandtl number, Pr = 50 and for Ra = 0 to 2.4 x 10^5 while Stefan number was varied from 0.05 to 0.15. They found that the development of natural convective circulation in the melt zone was suppressed due to sub-cooling of the un-melted solid and consequently the melting rate was significantly reduced. The authors concluded that in the presence of sub-cooling in the solid region, the melting proceeds rather efficiently in a cylindrical annulus of high radius ratio. This is because with the decreasing of the radius ratio of the annulus, the melting process reaches steady state quicker while yielding a smaller final molten volume ratio. In their paper the authors did not mention the value of the time step used. The grid and time independency tests were also not reported. For a high Prandtl number PCM, in order to avoid the thermal instability during numerical solution, more grid points should be employed near the boundaries. The model equations were solved using the stream function-vorticity method instead of primitive variables such as u and v velocities. For accurate numerical predictions, it is suggested that for stream-function and vorticity equations one should consider using more a denser grids near the boundaries. Since no comparison was made of their numerical results with others, it is difficult to judge how good and accurate the predictions are for the pre-selected grid distributions.

Fath (1991) experimentally investigated the transient behavior of a heat exchanger for thermal energy storage (TES) applications and also predicted the system's performance analytically. Pure paraffin wax was selected as a PCM to stored thermal energy. The heat storage container was a double pipe heat exchanger where the heat transfer fluid (hot water) flowed through the inner tube (made of copper of inner diameter = 14 mm and outer diameter = 15.4 mm, and length = 260 cm), while the heat sink (embedded PCM) filled the annulus gap of the exchanger (inner diameter of the outer cylinder = 80 mm). To reduce the heat losses the heat exchanger's outer surface was insulated with a 3.0-cm thick glass wool. From the experiments the author found that by increasing the heat transfer fluid inlet temperature and the flow rate, as well as by increasing the length of the heat exchanger both the heat transfer rate and accumulated (stored) energy increased. The author later concluded that convection in the molten zone is an important parameter which affected the heat exchanger's performance. An analytical model was also developed by the author for the prediction of the heat transfer rate and stored energy. The predicted results were compared with his own experimental findings and a good agreement was found. The developed model was also used to investigate the effects of various parameters like, convection in the molten region, initial PCM sub-cooling, and heat exchanger dimensions on the heat transfer rate and accumulated energy. The author concluded from the experiments that a single (full length) heat exchanger is thermally more effective than two (half length and equal heat capacity) parallel heat exchangers. Finally, the author suggested that more experiments were needed to make a definite conclusion of the latter aspect of the study.

Das and Dutta (1993) both experimentally and numerically investigated the melting characteristics of a pure paraffin wax encapsulated in the annulus of two concentric horizontal cylinders. Their experimental set-up consisted of a double-pipe heat exchanger with the inner pipe of ¾ inch diameter and the outer pipe of 3-inch diameter. By circulating hot water the inner pipe was kept isothermal while the outer pipe was kept insulated. A 2D transient conduction equation in r-θ coordinates was used as the model equation for the numerical simulations. They experimentally tracked the liquid-solid interface which developed between the molten and solid wax during the progression of melting. They compared their simulated results with the experiments and showed that the nature of the cooling curve during freezing and the heating curve during melting were identical. They observed an initial time lag in the experimental curves compared to the numerical ones. They explained that the time lag in the heating and cooling curves occurred due to the assumptions which were imposed in developing the theoretical model. Finally, the authors suggested that the melting time will be lower if the Rayleigh number is higher. As can be seen from their numerical simulation results, only the conductive mode of heat transfer was considered in the analysis. By solving only the conduction equation it is not possible to precisely predict the actual phenomenon that occurs in the annulus gap during the complex melting process. It is almost impossible to get the same numerical results as experiments without considering the natural convection effect in the melt zone in the numerical model.

Tong et al. (1996) numerically investigated the melting and freezing characteristics of ice/water system in a vertical annulus space which was homogeneously distributed with highly porous and permeable pure aluminum matrix. The inner wall was assumed isothermal and the other three boundaries were considered insulated. The flow in the melted region was considered as 2D laminar and unsteady. A grid system consisting of 27 x 27 grids were used for the calculations. The input parameters were Ra = 5 x 10^6, Ste=0.1, Da = 4.17 x 10^{-5}. Their numerical predictions show, compared to the plain vertical annulus, the heat transfer rate at the inner wall increased significantly when the metal matrix was inserted in the vertical annulus gap.

Chung et al. (1997) numerically studied the 2D unsteady laminar melting process inside an isothermally heated horizontal cylinder for a wide range of Rayleigh numbers (Ra was varied from 1.0 x 10^4 to 3.0 x 10^7). The cylinder wall temperature was above the melting temperature of the PCM. The enthalpy-porosity method was employed to handle the phase-change of a pure PCM (n-octadecane, $C_{18}H_{38}$). A uniform grid system, consisting of 36 x 72 grids, was used for low Ra and a non-uniform grid system consisting of 41 x 81 grids was used for high Ra. They predicted that at a low Ra, the flow in the liquid gap remained stable and only a single recirculation cell developed during the initial melting stage. At the intermediate Ra, the thermal buoyancy and the viscous forces were balanced in a neutrally stable state and a delicate interaction between the two flows determined the flow patterns. For a high Ra, the Bernard-type convection was found to develop within a narrow liquid gap between the un-melted solid surface and the cylinder bottom wall. The authors varied the Ra from 1.0 x 10^4 to 3.0 x 10^7 for a pure

PCM. It is to be realized that for the melting of a pure PCM, the Ra can't be arbitrarily varied since for a fixed wall temperature, Ra is also fixed.

Ng et al. (1998a, 1998b) numerically solved the problem of melting in a horizontal double-pipe heat exchanger for a pure PCM (99% pure n-octadecane) embedded inside an annulus. A streamline upwind/Petrov Galerkin finite element method (Brooks and Hughes, 1982) in combination with primitive variables was employed to solve the convection dominated melting problem for unsteady laminar flow of the melt. The well known enthalpy-porosity model was employed to track the irregular liquid-solid interface by employing a fixed-grid net. At the inner cylinder wall, a constant temperature boundary condition was applied which was higher than the melting point of the pure PCM and the outer cylinder wall was insulated. Two Rayleigh numbers were selected for simulation study, namely, 2.844×10^5 and 2.844×10^6, to find the melting rate as well as the evolution of the flow patterns. The authors observed that with the increase of Ra, the heat transfer rate and the melting rate increased. Moreover, they found that the melting of PCM in the bottom part was very inefficient because most of the energy charged to the system was mainly transferred to the upper part of the annulus by the convective flow of the melt. Multiple cellular patterns were observed at the melting zone for a high Ra = 2.844×10^6 during the dimensionless melting time from 0.043 to 0.389. In their paper, the authors neither mentioned the time step used nor the number of finite elements employed. Although the authors used a pure PCM and employed the enthalpy-porosity formulation, they did not clarify the way they implemented the latter scheme. There is no sensitivity analysis on the predicted results. Since without sensitivity analysis, it is difficult to rely on the predicted findings.

Khillarkar et al. (2000) numerically studied melting of a pure PCM (n-octadecane) in a concentric horizontal annulus of arbitrary cross-section using a finite element method. Specifically, they modeled two geometrical arrangements, in one case they considered a square outer tube with a circular inner tube (called annulus type-A) and in the second case they considered a circular external tube with a square inside tube (called annulus type-B). The effects of Ra as well as the heating of either the inside wall or the outside wall and in some cases both the walls for a temperature above the melting point of the PCM on the melting characteristics were considered. The enthalpy-porosity formulation was employed on a fixed grid to solve the phase-change problems. A streamline upwind/Petrov Galerkin finite element method in combination with the primitive variables was employed to solve the convection-dominated melting problems. For both the horizontal annuli of type-A and type-B, it was observed that the effects of heating both the walls was the same as the heating of the inside or the outside wall separately until there was an interaction between the two melted regions. It was observed that the melting rate was faster due to good mixing between the melt regions. This heating arrangement suppressed the thermal stratification attained in both type-A and type=B horizontal annuli. The thermal stratification occurred in the upper portion of the annulus due to the fact that the energy charged to the system was mainly carried in the upward direction by natural convection. In their paper the authors did not mention anything about grid and time independency tests. Also, neither the time step used nor it was specified the small temperature difference between the liquidus and solidus temperature which is required to implement the enthalpy-porosity method in modeling melting problems.

Ismail et al. (2003) numerically studied the melting of a pure PCM (n-octadecane) around a horizontal cylinder in the presence of natural convection in the melt. A two dimensional transient mathematical model was formulated in terms of the primitive variables and a coordinate transformation method was used to fix the moving interface which was later tracked from the interface boundary conditions and the governing equations. The finite volume approach was used to discretize the transformed equations. They compared their predicted results with the numerical results from others and claimed to have obtained a satisfactory agreement. These authors provided some correlations for calculating the melt volume fraction in terms of Ra, Stefan number and cylinder wall temperature. It was mentioned that with the increase of Ra the total melt volume increased until about Ra = 24000. With the further increase of Ra, the melt volume reached almost a steady condition. They found similar effects for the increase of Stefan number and cylinder wall temperature. The authors did not mention the limit of the parameters such as, Ra, Ste, and cylinder wall temperature for which their correlations are applicable. Also, a time component should be there in the correlations since melting is a transient process.

Hendra et al. (2005) developed physical and theoretical models to investigate the thermal behavior of the Mikro LHTES system during melting. Mikro is an Indonesia traditional substance, mixed from 60% Paraffin, 8% Damar (wood spices), 32% Kendal (animal fat) and

Vaseline with a latent heat of fusion of 1.14×10^5 J/kg. Their experimental container consisted of staggered aluminum tubes with heat transfer fluid (water) flowing inside the tubes. The tubes remained immersed in Mikro used as a PCM. Inside diameter of the tube and the container were 1.5×10^{-2} and 0.2625 m, respectively. Thermally controlled electrical heat source was embedded instead of the heat transfer fluid to heat-up the PCM. Their mathematical model is based on a 2D unsteady heat conduction equation. They found that the theoretical results matched fairly well with the experimental results. They concluded that the melting front moved from the top to the bottom in the axial direction in the PCM and it was mostly governed by convection heat transfer in the melted PCM. Although their experimental melting study was convection dominated but their model was based on 2D transient conduction equations. As a result, it is not clear how their experimental results matched the modeled results.

Liu et al (2005) conducted experiments on the melting process in an annulus filled with a pure PCM (stearic acid). A 20-mm diameter electric heating rod was placed into a 46-mm diameter cylindrical tube. The length of the tube was selected as 550-mm. The heating rod and the tube were placed in concentric position so as to mimic a double-pipe heat exchanger. The outside of the tube was well insulated with a porous polythene insulator. The liquid-solid transition temperature of the pure stearic acid was taken as 67.7^0C. By changing the supplied current to the heating rod, different heat flux conditions were created to determine the influence of heat flux on the melting process. In their experiments the authors designed and fixed a new type of fin onto the electrical heating rod to investigate the thermal response of the pure PCM. Their experimental results showed that the fin enhanced both heat conduction and natural convection in the melt.

Mesalhy et al. (2005) numerically investigated the melting process between two concentric cylinders considering that the annulus gap was filled with a high porosity high thermal conductivity metal matrix. The porous matrix was assumed to be fully saturated with low thermal conductivity but pure PCM. A two dimensional Brinkman, Forchiemer extended Darcy model was used for solving the PCM melting problem inside the porous matrix. A local non-equilibrium thermal condition was considered between the solid matrix and pure PCM. Compared to the plain annulus filled with a PCM, the presence of the porous matrix was found to have a great effect on the heat transfer and melting rate in term of energy storage. Their results show that the melting rate increased with the decrease of porosity of the matrix although it dampened the convective motion because of the reduction of the volume of the voids spaces. These authors suggested that to enhance the response rate and energy storage capacity, the best technique would be to use a high porosity and high thermal conductivity solid matrix filled with a PCM in the annulus.

Balikowski and Mollendort (2007) experimentally investigated the performance of two PCMs, namely, Climsel 28, and Thermasorb 83 in a horizontal double-pipe heat exchanger with smooth pipe and spined fins for various charging and discharging periods and flow rates. The phase change temperature range of C28 was 18-38^{0}C and for TY83 was 27.2-29.4^{0}C. The latent heat of C28 and TY83 was 126 kJ/kg and 186 kJ/kg, respectively while the thermal conductivity was 0.6 W/m/^{0}C and 0.15 W/m/^{0}C. The PCM was placed in the annular space of a double-pipe heat exchanger (inside cylinder diameter was about 0.49 in, and outside cylinder diameter was about 0.63 in) with hot water circulating through the inner pipe. For spined pipe, the curved fins were about 0.6 inches long, about 0.08 inches wide at the base, and about 0.032 inches thick. There were about 25 fins (spines) per spiral revolution and there were about 170 spiral revolutions on the copper tube used in the experiments. It was found that the presence of spined fins enhanced the rate of charging and discharging of thermal energy due to increased fin contact area with the outer layers of the PCM. Further it was found that TY83-PCM in the spined heat exchanger transferred more heat and at a faster rate compared to the C28-PCM embedded spined heat exchanger. Their experimental findings make a good argument with regard to the beneficial usage of fins in LHTES systems.

Dutta et al. (2008) recently studied both experimentally and numerically the liquid-solid phase change heat transfer in a paraffin wax encapsulated in the annulus of two coaxial circular cylinders under variable heat fluxes. They verified their numerical model with their own experimental findings and they claimed to have obtained a good agreement between their predicted and experimental results. For their experimental work they considered a hollow adiabatic steel cylinder of diameter 10.16 cm, length 30.48 cm and an internal pipe of diameter 1.905 cm which was placed coaxially and horizontally with the outer cylinder. T-type thermo-couples were placed in the radial direction in the annulus to record the temperature at 5 sec interval. For the numerical work they selected the annulus gap which was formed by a 1-m diameter inner cylinder and 5-m diameter outer cylinder. Their modeled annulus gap was much bigger than their experimental one. In their 2D unsteady state numerical model, the mesh consisted of 200 x 200 grids, the convergence criterion was taken as 10^{-5}, and the total time simulated was about 30,000 sec. The melt flow was considered to be laminar. From their experimental results they found that a higher rate of melting occurred in the upper half of the annulus. To verify their experimental results with their numerical predictions they had chosen the time-temperature relationship profile inside the annulus for the inner cylinder wall temperature of 75^0C as the verification criteria. Later, the authors numerically studied the effects of the eccentricity (varied from 0.0 to 0.50) as well as the angle of inclination of eccentricity (between -$\pi/2$ to $\pi/2$) in an annulus on the energy transfer enhancements for Ra = 5.77×10^7 and Pr = 46.5. The authors observed from their simulated results that both eccentricity and the variation in the angle of inclination of the eccentricity has dominant effect on the net circulation of the molten PCM and the heat flux at the outer surface of the inner cylinder forming the annulus. They also found that for a given eccentricity, the magnitude of the net circulation approached the maximum value when its angle of inclination approached to -30^0. Their analysis further showed that the heat flux along the inner cylinder wall for a fixed angle of inclination reached a maximum value for the highest eccentricity (ε=0.5) in the fourth quadrant and reached a minimum value when the eccentricity was the maximum in the first quadrant. Finally, the authors showed the heat flux on the inner cylinder surface enhanced in the eccentric annulus compared to the concentric annulus. This work is the most comprehensive thus far in the field. But in their work they used a pure PCM as mentioned in their Table-2. The enthalpy-porosity formulation method was used to indirectly handle the liquid-solid interface progression with time. The authors did not mention in their paper what arbitrary temperature difference between the solidus and liquidus temperatures they had considered in order to handle the mushy region required by the enthalpy-porosity formulation method for modeling a pure PCM. It is thus surprising that they got similar results for time-temperature relationship curves for experimental work which was a 3D problem with a diameter ratio of 10.16:1.905 as their numerical work which modeled a 2D problem with the diameter ratio of 5:1. The cylinder's length of the experimental set-up was only 30.48 cm, which obviously imposed end effects on the results. The time step used in the simulations was also not mentioned. One of the limitations of their work is that the geometrical dimensions of the numerical model do not match with the experimental dimensions as stated above. Since the annulus gap is very large in the model, a melting around the inner pipe is essentially similar to the situation of outward melting of a heated horizontal cylinder embedded in an infinite extent of PCM.

Recently, Medrano et al. (2009) experimentally investigated the heat transfer process during melting (charge) and solidification (discharge) of five small heat exchangers working as a LHTES systems. The three different types of heat exchangers were investigated, namely, a concentric tube heat exchanger, a compact tube-fin heat exchanger, and a plate heat exchanger. For the first type, three variations of heat storage arrangements were studied: (1) a simple double pipe copper tube heat exchanger with the PCM embedded in the annular space, (2) the same double pipe heat exchanger as in case (1) but with the PCM embedded in a graphite matrix to increase the heat transfer rate, and (3) a double pipe heat exchanger with 13 radial copper fins and with the same PCM in the annular space as in cases (1) and (2). The pure PCM (RT35 PCM) which has a melting point of 35^0C was selected for these five different heat storage devices. In all cases, PCM was filled in one side of the heat exchanger and water was circulated as the heat transfer fluid through the other side. In the experiments the water flow rate and water inlet temperature were varied. Comparisons were made among the heat exchangers in terms of effectiveness of energy storage on the basis of average power per unit area and per average temperature gradient. Results showed that double pipe heat exchanger with the PCM embedded in a graphite matrix was the most favorable, registering heat transfer rates in the range of 700-800 W/m^2-K, which were an order of magnitude higher than the ones presented by the second best. The compact heat exchanger offered the highest average thermal power (above 1 kW), as it had the highest ratio of heat transfer area to external volume.

Very recently, Agyenim et al (2009) experimentally studied the melting and solidification characteristics of a PCM (Erythritol) in a double pipe heat exchanger where the PCM was embedded in the horizontal annulus gap. Three geometrical configurations of the heat transfer surface, namely a plain, a circular finned and a longitudinal finned annuli were investigated for both melting (charging) and solidification (discharging) cycles. For the circular and longitudinal finned cases, eight circular and eight longitudinal copper fins were braised onto the outer surface of the inner tube, In each of the finned experimental setup, 3 mm gap was left between the tip of the fin and the inner surface of the outer tube. The effect of the mass flow rate of the HTF (hot oil for melting and cold water for solidification) on the thermal performance of the PCM was investigated. Their temperature measurements in the radial, circumferential and longitudinal directions revealed that in the latter direction the gradients were below 5% of the temperature gradients in the radial direction and the authors postulated that for the heat transfer analysis, it is not necessary to take into consideration the variations in temperatures in the flow direction of the HTF. Therefore, a 2D analysis considering buoyancy driven melting should be accurate enough for predicting the melting behavior of the PCM in the horizontal annulus. The authors further found that the longitudinal finned annulus provided the best thermal efficiency compared to the other two cases.

2.3 Closure

From the above literature review and discussion it is clear that no CFD modeling work exists concerning the problem of melting of a commercial PCM embedded inside the annulus of two horizontal concentric cylinders. During melting and solidification processes of a multi-component material, a complicated structure named "mushy region" develops in the domain. The phase change problem with a mushy region in a complex geometry, like an annulus formed by concentric horizontal cylinders, is a difficult problem to solve numerically. In most of the numerical studies reviewed above nothing was mentioned concerning the time step used for the simulation runs. Also, if the grid size and time step independency were carried out or not were not reported in none of the reviewed works. Although, not mentioned in the papers reviewed, it appears that to model the melting problems many authors have used commercial codes, as a result they could not provide details about the numerical scheme and the associated factors which are necessary to execute the codes. It is also not clear how some authors numerically handled the arbitrary annulus geometries in their models. As will be seen in chapters four and five, the present numerical model was able to provide converged results in every instant of time for both plain and finned annuli for a commercial PCM when the melt flow is laminar and two-dimensional. The developed model offers the advantage by the fact that the entire domain can be treated as a single-region problem which is governed by one set of conservation equations. In other words, the same equation can be used for the melt, solid and mushy region as well as for the fins. The results showed that a conduction dominated region developed at the lower part of the geometry. This suppressed the thermal stratification attained in the horizontal annulus. In the present study, in order to avoid any thermal storage penalty and to accelerate the melting rate, three longitudinal divergent fins were attached at the lower part of the geometry. It is expected that due to the fins the conduction-convection mode of heat transfer will be enhanced at the lower portion of the annulus. The employment of longitudinal fins at strategic locations of the annulus is new and has not been analyzed before.

CHAPTER – THREE

Mathematical Formulation and Numerical Approach

3.1.1 Introduction

Mathematically, the problem of solid-liquid phase change is known as a “moving boundary problem”. If the temperature of the inner cylinder is higher than the melting temperature of the PCM then melting will initiate around the inner cylinder surface and for a commercial PCM a mushy region will move into the annulus. In this study, an emphasis has been placed on the analysis of the progression of melting. During melting of a PCM the density variations inside the liquid phase do occur due to temperature gradients. As a result, buoyancy-driven convective flows develop in the melt which make the melting process quite complex, specially, for a horizontal cylindrical annulus. During solidification, freezing will start around the inner cylinder wall and the solid layer will grow outward into the melt. Unless a constant heat source is maintained, in the solidification process the effect of natural convection only prevails during the early part of solidification and most of the time there is conduction dominated heat transfer. As a result, the modeling of the solidification problem is drastically simplified.

It is noteworthy to point out that during the melting process in the annulus the effect of natural convection current at the top of the annulus is significantly prominent whereas the heat transfer mechanism at the bottom half is governed predominantly by the conduction heat transfer process. The “pure” buoyancy-driven convective effect i.e., natural convection induced by temperature gradient in the melt can be enhanced by introducing internal fins at the lower part of the annulus. A melting problem with fins attached to the specific locations of the inner cylinder seems not to have been investigated yet for an annulus. In the present analysis, a single-domain enthalpy formulation approach is utilized which is applicable for the whole domain.

The development of the governing equations used to simulate the melting process of a commercial PCM in a horizontal concentric annulus with and without internally attached fins on the outer surface of the inner cylinder is discussed in this chapter. The model equations are presented in Section 3.2 while Section 3.3 is devoted to their numerical solution procedure. Other associated numerical items such as, convergence criterion, under relaxation factors, code validation tests, grid and time independency tests results are presented sequentially in Sections 3.4 to 3.8.

3.2 Mathematical Formulation

As depicted in Figure 3.1, the physical domain is selected to be two horizontal concentric cylinders in which the volume located between them is filled with a phase-change material. Here, r_0, and r_i are the radius of the outer and inner cylinders respectively. Due to symmetry in the θ-direction, the computation has been conducted on the right-half of the domain. Initially, the solid PCM

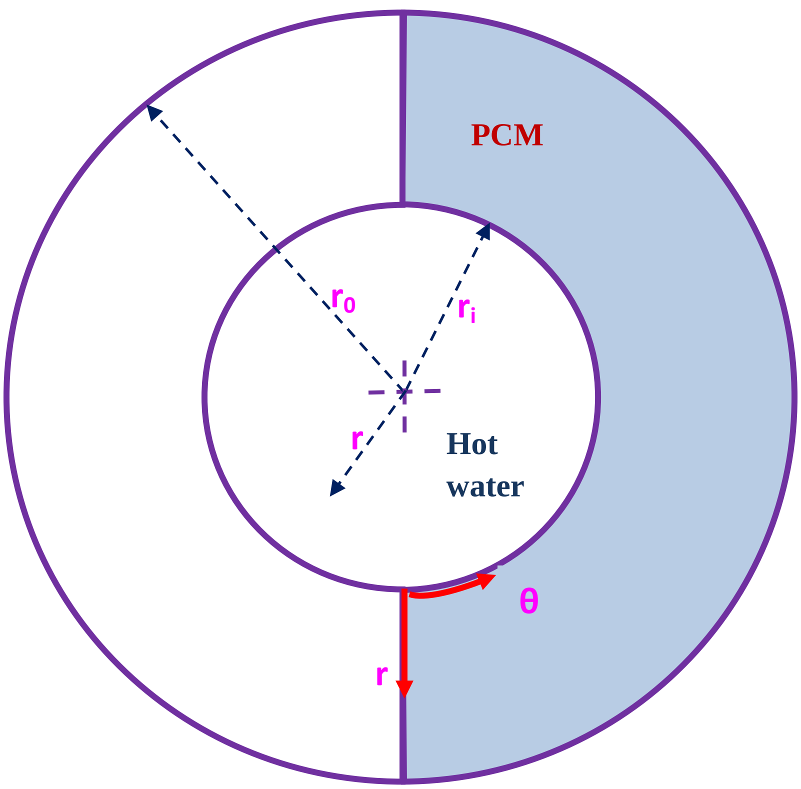

Figure 3.1: Schematic view of the cross-section of the double-pipe heat exchanger with the blue part representing the computational domain.

is embedded in the plain cylindrical annulus is at a uniform temperature (T_i) that is either equal to or below the solidus temperature (T_S) of the PCM. When the initial temperature is below the solidification temperature of the PCM, this thermal condition is designated as sub-cooled condition. For time $t > 0$, a constant temperature (T_W) is imposed on the surface of the inner cylinder, which is greater than the liquidus temperature (T_L) of the PCM, i.e., $T_W > T_L$. The outer wall of the annulus is maintained at the adiabatic condition throughout the whole melting process. A constant wall temperature (T_W) is maintained at the outer surface of the inner cylinder.

Figure 3.2 shows the identical physical model presented in Figure-3.1, the only exception here is three longitudinal divergent round tips fins are attached on

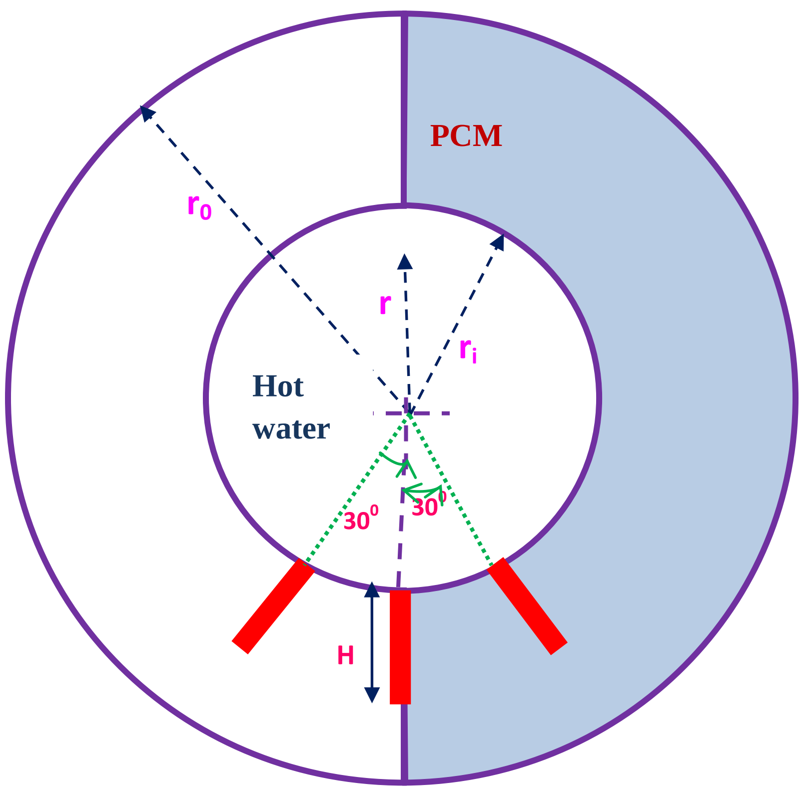

Figure 3.2: Schematic view of the cross-section of the finned annulus with the blue part representing the computational domain.

the outer surface of the inner cylinder's wall. One fin is placed at the angle $\theta = 0^0$, that is at the lower symmetry plane and the other two are placed at angular positions $\theta = 30^0$ and 330^0. It is expected that these high thermal conductivity aluminum fins will increase the natural convention intensity at the bottom portion of the annulus.

3.2.1 Model Assumptions

The following idealizations are made in developing the current mathematical model of the physical problem for the phase-change process with mushy region in the presence of the buoyancy driven convective flows:

1. The melt behaves as an incompressible Newtonian fluid.
2. The convective motion in the melt is laminar and two-dimensional. Compared to the radii of the two cylinders, the length of the cylinders are long such that there are no end effects on the selected cross-section along the longitudinal direction.
3. No-slip conditions are applicable for the velocity components at the boundaries.
4. Thermo-physical properties of the PCM are assumed to be constant in both solid and liquid phases except for the density variations in the melt are considered insofar as they contribute to the buoyancy forces.
5. Buoyancy forces are incorporated in the momentum equations based on the Boussinesq approximations.
6. The physical properties of the PCM are temperature independent within each phase and are evaluated at the liquidus temperature.
7. No viscous dissipation occurred in the calculation domain.
8. Variation of liquid fraction in the mushy region is assumed to be a linear function of temperature.
9. The effects of volume change associated with the solid-liquid phase change are neglected.
10. There is no heat loss or gain from the surroundings.

With the above assumptions, the temperature distribution within the solid, liquid, and mushy regions and the fluid motion in the liquid and the mushy zones are governed by the standard Navier-Stokes and energy equations.

3.2.2 Governing Equations

A general conservative form of dimensional governing equations such as mass, momentum and energy equations for plain and finned annulus in r- θ coordinates are given as follows:

Continuity equation:

$$\frac{\partial \rho_r}{\partial t} + \frac{1}{r}\frac{\partial(\rho_r r v)}{\partial r} + \frac{1}{r}\frac{\partial(\rho_r u)}{\partial \theta} = 0 \text{ --- (1)}$$

(1)

U-momentum equation:

$$\frac{\partial(\rho_r u)}{\partial t} + \frac{1}{r}\frac{\partial}{\partial r}(\rho_r r u u) + \frac{1}{r}\frac{\partial}{\partial \theta}(\rho_r u v) = \frac{1}{r}\frac{\partial}{\partial r}\left(\mu r\frac{\partial u}{\partial r}\right) + \frac{1}{r}\frac{\partial}{\partial \theta}\left(\frac{\mu}{r}\frac{\partial u}{\partial \theta}\right) - \frac{1}{r}\frac{\partial \mathrm{p}}{\partial \theta} + 2\frac{\mu}{r^2}\frac{\partial v}{\partial \theta} - \mu\frac{u}{r^2} - \rho_r\frac{uv}{r} - \rho g \sin\theta - \mathrm{Au} \text{ --- } \quad (2)$$

V-momentum equation:

$$\frac{\partial(\rho_r v)}{\partial t} + \frac{1}{r}\frac{\partial}{\partial r}(\rho_r r u v) + \frac{1}{r}\frac{\partial}{\partial \theta}(\rho_r v v) = \frac{1}{r}\frac{\partial}{\partial r}\left(\mu r\frac{\partial v}{\partial r}\right) + \frac{1}{r}\frac{\partial}{\partial \theta}\left(\frac{\mu}{r}\frac{\partial v}{\partial \theta}\right) - \frac{\partial \mathrm{p}}{\partial r} - 2\frac{\mu}{r^2}\frac{\partial u}{\partial \theta} - \mu\frac{v}{r^2} - \rho_r\frac{u^2}{r} + \rho g \cos\theta - \mathrm{Av} \text{ -- } \quad (3)$$

Energy equation:

$$\frac{\partial(\rho_r C_{\mathrm{P}}\mathrm{T})}{\partial t} + \frac{1}{r}\frac{\partial}{\partial r}(\rho_r r v C_{\mathrm{P}}\mathrm{T}) + \frac{1}{r}\frac{\partial}{\partial \theta}(\rho_r u C_{\mathrm{P}}\mathrm{T}) = \frac{1}{r}\frac{\partial}{\partial r}\left(\frac{K}{C_P} r\frac{\partial(C_{\mathrm{P}}\mathrm{T})}{\partial r}\right) + \frac{1}{r}\frac{\partial}{\partial \theta}\left(\frac{K}{C_P}\frac{1}{r}\frac{\partial(C_{\mathrm{P}}\mathrm{T})}{\partial \theta}\right) \text{ ------------- } \quad (4)$$

The continuity, momentum and energy equations in the r- θ coordinates for the phase-change problem in the finned annulus are the same as the plain annulus, which are written above. For the solid fins, one additional energy balance equation should be solved which can be written in the following form:

$$\frac{\partial(\rho_r C_P \mathrm{T})}{\partial t} = \frac{1}{r}\frac{\partial}{\partial r}\left(\frac{K}{C_P} r \frac{\partial(C_P \mathrm{T})}{\partial r}\right) + \frac{1}{r}\frac{\partial}{\partial \theta}\left(\frac{K}{C_P}\frac{1}{r}\frac{\partial(C_P \mathrm{T})}{\partial \theta}\right) \text{------------------------------------} \quad (5)$$

The variables are non-dimensionalized as follows:

$$R = \frac{r}{D_i}\ ;\ U = \frac{u}{\alpha/r_i}\ ;\ V = \frac{v}{\alpha/\mathrm{D}_i}\ ;\ \mathrm{h}^* = \frac{C_P(\mathrm{T} - \mathrm{T}_{SOLIDUS})}{\lambda}\ ;\ Ra = \frac{D_i^3 \beta_\mathrm{T} g(\mathrm{T}_{WALL} - \mathrm{T}_{\mathrm{SOLIDUS}})}{\nu\alpha}$$

$$p^* = \frac{PD_i^2}{\rho\alpha^2}\ ;\ \tau = \frac{\alpha t}{D_i^2}\ ;\ \nabla H^* = \frac{\nabla \mathrm{H}}{\lambda} \text{---} (6)$$

The non-dimensionalized conservative form of the governing equations, applicable in the computational domain, can be written as follows:

Continuity equation:

$$\frac{\partial \rho_r}{\partial \tau} + \frac{1}{R}\frac{\partial(\rho_r RV)}{\partial R} + \frac{1}{R}\frac{\partial(\rho_r U)}{\partial \theta} = 0 \quad \text{---} \quad (7)$$

U-momentum equation:

$$\frac{\partial U}{\partial \tau} + \frac{1}{R}\frac{\partial}{\partial R}(RUU) + \frac{1}{R}\frac{\partial}{\partial \theta}(UV) = \mathrm{Pr}\frac{1}{R}\frac{\partial}{\partial R}\left(R\frac{\partial U}{\partial R}\right) + \mathrm{Pr}\frac{1}{R}\frac{\partial}{\partial \theta}\left(\frac{1}{R}\frac{\partial U}{\partial \theta}\right) - \frac{1}{R}\frac{\partial P^*}{\partial \theta} + 2\frac{\mathrm{Pr}}{R^2}\frac{\partial V}{\partial \theta} - \mathrm{Pr}\frac{U}{R^2}$$
$$-\frac{UV}{R} + Ra^* \,\mathrm{Pr}(h^* - h^*_{REF})\sin\theta - \mathrm{A}^*\mathrm{U} \text{--} \quad (8)$$

V-momentum equation:

$$\frac{\partial V}{\partial \tau} + \frac{1}{R}\frac{\partial}{\partial R}(RUV) + \frac{1}{R}\frac{\partial}{\partial \theta}(VV) = \mathrm{Pr}\frac{1}{R}\frac{\partial}{\partial R}\left(R\frac{\partial V}{\partial R}\right) + \mathrm{Pr}\frac{1}{R}\frac{\partial}{\partial \theta}\left(\frac{1}{R}\frac{\partial V}{\partial \theta}\right) - \frac{\partial P^*}{\partial R} - 2\frac{\mathrm{Pr}}{R^2}\frac{\partial U}{\partial \theta} - \mathrm{Pr}\frac{V}{R^2}$$
$$+\frac{U^2}{R} - Ra^* \,\mathrm{Pr}(h^* - h^*_{REF})\cos\theta - A^*\mathrm{V} \text{---} \quad (9)$$

Energy equation:

$$\frac{\partial h^*}{\partial \tau}+\frac{1}{R^2}\frac{\partial}{\partial R}\left(RVh^*\right)+\frac{1}{R}\frac{\partial}{\partial \theta}\left(Uh^*\right)=\frac{1}{R}\frac{\partial}{\partial R}\left(R\frac{\partial h^*}{\partial R}\right)+\frac{1}{R}\frac{\partial}{\partial \theta}\left(\frac{1}{R}\frac{\partial h^*}{\partial \theta}\right)-\frac{1}{\mathrm{R}}\frac{\partial\left(RV\nabla H^*\right)}{\partial \mathrm{R}}-\frac{1}{R}\frac{\partial\left(U\nabla H^*\right)}{\partial \theta}-\frac{\partial \nabla H^*}{\partial \tau}\quad\text{--(10)}$$

Energy equation for solid fin:

$$\frac{\partial h^*}{\partial \tau}=\frac{\alpha_{Fin}}{\alpha_{PCM}}\frac{1}{R}\frac{\partial}{\partial R}\left(R\frac{\partial h^*}{\partial R}\right)+\frac{\alpha_{Fin}}{\alpha_{PCM}}\frac{1}{R}\frac{\partial}{\partial \theta}\left(\frac{1}{R}\frac{\partial h^*}{\partial \theta}\right)-\frac{\partial \nabla H^*}{\partial \tau}\quad\text{---------(11)}$$

3.2.3 Boundary conditions

Because of symmetry, the right-half of the annulus is chosen as the solution domain and the non-dimensional form of the boundary conditions corresponding to this problem are presented in Figure 3.3 for easy visualization. The dimensionless boundary conditions are:

1. At time, $\tau=0$: $\mathrm{h}_{\mathrm{i}}^*=\frac{C_{\mathrm{P}}\left(\mathrm{T}_i-\mathrm{T}_{SOLIDUS}\right)}{\lambda}$

   At time, $\tau>0$:

2. On the inner cylinder surface, i.e., $R_i=0.5$; U=V=0 ; $\mathrm{h}_{\mathrm{W}}^*=\frac{C_{\mathrm{P}}\left(\mathrm{T}_W-\mathrm{T}_{SOLIDUS}\right)}{\lambda}$
3. On the outer cylinder surface, i.e., $R_o=1.3$; U=V=0 ; $\frac{\partial h^*}{\partial R}=0$
4. Lower plane of symmetry; i.e., $\theta=0$; U=0 ; $\frac{\partial V}{\partial \theta}=\frac{\partial h^*}{\partial \theta}=0$
5. Upper plane of symmetry; i.e., $\theta=\pi$; U=0 ; $\frac{\partial V}{\partial \theta}=\frac{\partial h^*}{\partial \theta}=0$

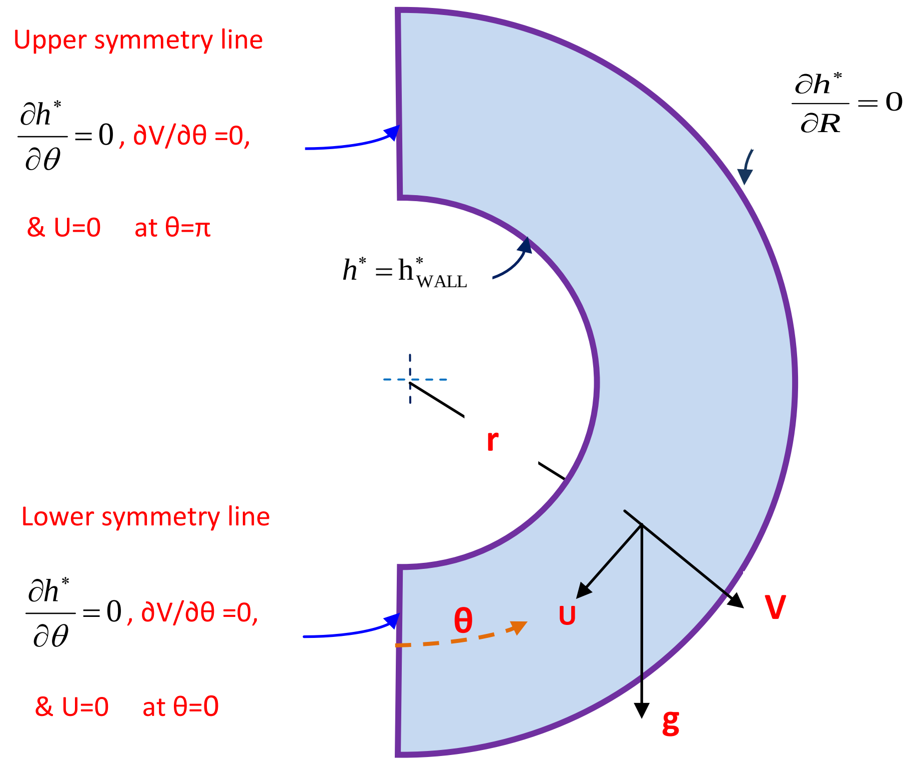

Figure 3.3: Schematic illustrations of the configuration with the boundary conditions.

The developed non-dimensionalized model for this complex annular geometry is used for a high Prandlt number commercial paraffin wax to generate the numerical simulation results of the melting process. The thermo-physical properties of wrought paraffin wax (Farid et al., 2004) and diameters of the inner and outer cylinders are given in Table 3.1

Table 3.1: Thermo-physical properties of PCM (Paraffin wax) and geometrical parameters

Properties	Value
Thermal conductivity (liquid or solid) (k)	0.22 W / m K
Density (liquid or solid) (ρ)	790 kg/m^3
Specific heat (liquid or solid) (C_P)	2.15 kJ/kg K
Latent heat of melting (λ)	190 kJ/kg
Liquidus temperature (T_L)	59.9 °C
Solidus temperature (T_S)	51.2 °C
Kinematic viscosity (μ)	5.2 x 10^{-6} m^2/ s
Liquid thermal expansion coefficient (β)	1.0E-03 1/^{0}C

Geometrical dimension	
Inner cylinder diameter (d_i)	0.04 m
Outer cylinder diameter (d_0)	0.104 m

3.3 Numerical Solution

3.3.1 Solution Procedure

All the two-dimensional equations presented above can be expressed in a general form of dimensional partial differential equation. The conservation equations in the general form can be written as follows:

$$\frac{\partial(\rho_r\varphi)}{\partial t}+\frac{1}{r}\frac{\partial}{\partial r}\left(\rho_r ru\varphi-\Gamma_\varphi r\frac{\partial\varphi}{\partial r}\right)+\frac{1}{r}\frac{\partial}{\partial\theta}\left(\rho_r v\varphi-\frac{\Gamma_\varphi}{r}\frac{\partial\varphi}{\partial\theta}\right)=S_\varphi \quad (12)$$

where φ , Γ_φ ,and S_φ are the general dependent variable, the generalized diffusion term, and the source term, respectively. The values of φ corresponding to mass, momentum and energy equations are 1, U, and V, and h^*. The associated variables Γ_φ and S_φ for all of the transport equations written earlier can be obtained by comparing the general conservative equation (equation 12) and equations 1-4.

In order to achieve the numerical solution, all of the partial differential equations have to be set in an algebraic form, this is called discretization. The discretized equations are derived by integration of differential equations over each control volume of the calculation domain by using an implicit time-step method. Power-law difference scheme of Patankar (1980) is used to discretize the convection-diffusion terms. Here, the SIMPLE algorithm, which stands for Semi-Implicit Method for Pressure-Linked Equations, has been employed for resolving the pressure-velocity coupling in the momentum equations (Patankar,1980). In the following section the solution procedure is briefly explained.

Each of the above derived-discretized equations is incorporated in the following form:

$$a_p\phi_p = a_E\phi_E + a_W\phi_W + a_N\phi_N + a_S\phi_S + b_\phi \tag{13}$$

where, a_E, a_W, a_N, and a_S are the coefficients of the four neighboring nodes of node P shown in a two-dimensional grid in Figure 3.4. b_Φ is the source term. The coefficients entail the diffusion and convection terms while the source term may involve various terms such as pressure gradient, buoyancy force, and Darcy terms. The developed computer program is an in-house code based on the control volume finite difference scheme and uses the power-law scheme for the discretization of the diffusion-convection terms. The whole domain is described by a displaced or staggered grid system. This algorithm is explained in detail by Patankar [1980].

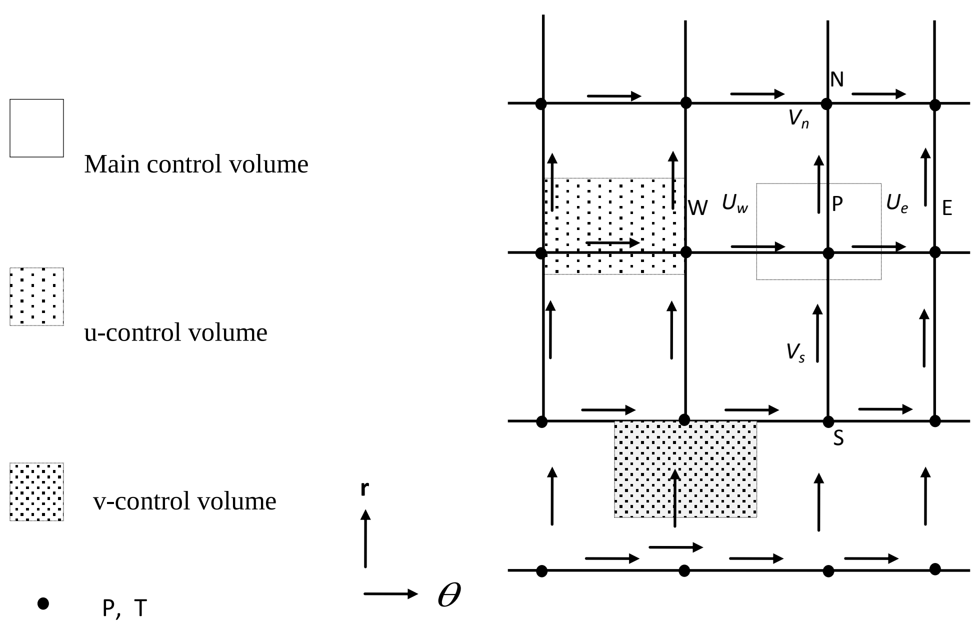

Figure 3.4: Staggered grid

The generalized formula for the neighbor point coefficients for each schemes are as follows:

$$a_E = D_e A(|Pe_e|) + \| -F_e , 0 \|$$

$$a_W = D_w A(|\mathrm{P}e_w|) + \|- \mathrm{F_w} , 0\|$$

$$a_N = D_n A(|\mathrm{P}e_n|) + \|- \mathrm{F_n} , 0\|$$

$$a_S = D_s A(|\mathrm{P}e_s|) + \|- \mathrm{F_s} , 0\|$$

Here, D_e is diffusion conductance at interface e between P and E, and D_w , D_n and D_s are similar values in w, n, and s interfaces, respectively. F_e denotes the strength of convection at interface e between P and E and F_w , F_n and F_s are similar values in w, n, and s interfaces, respectively. Pe is Peclet number defined by the ratio of strength of convection to diffusion conductance. The operator $\|a , \mathrm{b}\|$ is equivalent to AMAX (A,B) in FORTRAN.

For power-law difference scheme the formula for the function $A(|\mathrm{P}e_e|)$ is given by (Patanker,1980). The general form of linearized source term is: $S_\Phi = S_C + S_\mathrm{P}\Phi_\mathrm{P}$

where, S_C becomes the contributor to b and S_P a contributor to a_P in the discretized equation. An in-house CFD code developed over the years by Professor Hasan's group at McGill University was modified to solve the two problems presented in this thesis.

3.3.2 Solidification Modeling

For a phase change material having a melting range instead of a single melting point, the latent heat release would be a function of the fraction melted. The major barrier in analyzing phase change problems is the occurrence of an interface or interfaces whose location is (are) unknown *a priori*, and across which the latent heat is to be released. At the phase boundary, continuity of velocity and temperature is required. Also, at the phase boundary a jump in the heat flux occurs, which is proportional to the latent heat (Kim and Kaviany, 1992).

Here, the single domain approach is followed in the present simulation since it does not require the tracking of the unknown interface (melting front). In the current work, the enthalpy based method is implemented (Voller, 1990; Voller et al., 1990; Date, 1991; Savnarskil et al., 1993). The technique is characterized by decomposing the enthalpy into sensible and nodal latent heat in the energy equation:

$$H=h+\Delta H \tag{14}$$

where h is the sensible heat defined as:

$$\int_{h_{ref}}^{h} dh = \int_{T_{ref}}^{T} c_p \, dT \tag{15}$$

For constant c_p, and taking h_{ref}=0 at T_{ref}, the above equation can be integrated to obtain the sensible heat as:

$$h= c_p (T-T_{ref}) \tag{16}$$

In order to establish the region of phase change, the latent heat contribution is specified as a function of temperature, i.e. $\Delta H= f(T)$.

Since the energy equation is valid in the entire calculation domain including solid, liquid, and mushy regions, the nodal latent heat can be related to the liquid fraction. It becomes zero in the solid phase and equals the latent heat of fusion (λ) in the liquid phase. In the mushy region, the latent heat can be any function of liquid fraction. In the current model, it is assumed to be linear.

$$\Delta H= \lambda \, f_l \tag{17}$$

where f_l is the liquid fraction, which is related to temperature as:

$$f_l = \begin{cases} 1 & when \quad T \geq T_L, \\ \dfrac{T - T_s}{T_L - T_s} & when \quad T_L \geq T \geq T_s, \\ 0 & when \quad T \leq T_s. \end{cases} \tag{18}$$

where T_L and T_s are the liquidus and solidus temperatures, respectively.

3.3.3 Modeling of fluid flow in the mushy region

In the current model, the Darcy law for porous media is adopted to model the flow of PCM in the mushy region. The law is based on the empirical measurement of the permeability. Darcy's law for a porous media can be written as:

$$u_i = -\frac{K}{\mu}\left(\frac{\partial P}{\partial x_i} - \rho g_{xi}\right) \tag{19}$$

where K is the permeability, which is a function of porosity, or in the case of a mushy region of a commercial material, a function of liquid fraction. In the model, the permeability decreases with decreasing liquid fraction and ultimately it forces all the velocities to become zero in the case of a stationary solid. The coefficient $\frac{\mu}{K}$ decreases from a large value in the solid phase to zero in the liquid phase. Consequently, the Darcy source term vanishes as the liquid fraction becomes one. The Carman-Koseny equation is adopted for the relation between the permeability and the liquid fraction (Voller and Prakash, 1987).

$$\frac{\mu}{K} = \frac{C(1 - f_l)^2}{f_l^3 + q} \tag{20}$$

where q is a small positive number introduced to avoid division by zero in the numerical calculations. C is a constant that depends on the morphology of the porous media. The value of C has been estimated from the expression given by Minakawa et al. (1987) as:

$$C=180/d^2 \tag{21}$$

where d is assumed to be constant and is equal to the secondary dendrite arm spacing. In this study, the value of d has been arbitrarily taken as 1x 10^{-4} m.

3.3.4 Modeling of the Buoyancy term

Natural convection effects are incorporated into the numerical code verification part of the current study through the use of Boussinesq approximation for a single phase fluid at steady state. In order to assess the role of buoyancy-driven convection during melting as per Boussinesq approximation, the density is assumed to be constant in all terms except the buoyancy term, which is given by:

$$\rho = \rho_{ref}\left[1 - \beta\left(\mathrm{T} - \mathrm{T}_{ref}\right)\right] \tag{22}$$

where β is the thermal volumetric expansion coefficient defined as:

$$\beta = -\frac{1}{\rho}\left(\frac{\partial \rho}{\partial T}\right)_P \tag{23}$$

For the sake of simplicity, the u-momentum equation is written in the following short from as:

$$\rho_r\left(\frac{\partial u}{\partial t} + \frac{1}{r}\frac{\partial (ruu)}{\partial r} + ...\right) = -\frac{1}{r}\frac{\partial p}{\partial \theta} - \rho\, g \sin\theta + \frac{1}{r}\frac{\partial}{\partial r}\left(\mu r \frac{\partial u}{\partial r}\right) + ... \tag{24}$$

where the second term on the R.H.S. represents the body force term. The flow of the molten PCM is gravity driven. Therefore, the pressure gradient and buoyancy term can be written in the following form:

$$-\frac{1}{r}\frac{\partial p}{\partial \theta} - \rho g \sin\theta = -\frac{1}{r}\frac{\partial \mathrm{P}}{\partial \theta} + \rho_r\, \beta g\left(\mathrm{T} - \mathrm{T}_r\right)\sin\theta \tag{25}$$

After substituting Equation (25) into Equation (24), one obtains the following equation:

$$\rho_r\left[\frac{\partial u}{\partial t}+\frac{1}{r}\frac{\partial(ruu)}{\partial r}+..................\right]=-\frac{1}{r}\frac{\partial \mathrm{P}}{\partial \theta}+\rho_r\beta\, g(\mathrm{T}-\mathrm{T}_r)\sin\theta+\frac{1}{r}\frac{\partial}{\partial r}\left(\mu r\frac{\partial u}{\partial r}\right)+...... \tag{26}$$

The above equation can be written in a dimensionless form using the non-dimensional parameters discussed in Section 3.3.2 in equation (6), as follows:

$$\frac{\partial U}{\partial \tau}+\frac{1}{R}\frac{\partial}{\partial R}(RUU)+----=\frac{\lambda\beta g D_i^3}{\alpha^2 C_P}\left(h^*-h^*_{REF}\right)\sin\theta+\frac{\mu}{\rho_r\alpha}\frac{1}{R}\frac{\partial}{\partial R}\left(R\frac{\partial U}{\partial R}\right)+-------------- \tag{27}$$

The above equation can be further simplified in the following form:

$$\frac{\partial U}{\partial \tau}+\frac{1}{R}\frac{\partial}{\partial R}(RUU)+----=\frac{Ra\,\mathrm{Pr}}{Ste}\left(h^*-h^*_{REF}\right)\sin\theta+\frac{\mu}{\rho_r\alpha}\frac{1}{R}\frac{\partial}{\partial R}\left(R\frac{\partial U}{\partial R}\right)+---------------- \tag{28}$$

where Ra is the Rayleigh number, which is the ratio of buoyancy force to change of momentum flux, $Ra=\frac{g\,\beta(\mathrm{T}_{WALL}-\mathrm{T}_{SOLIDUS})\ D_i^3}{\upsilon\alpha}$

Pr is the Prandlt number and is define by: $\mathrm{Pr}=\frac{\mu}{\rho_r\alpha}$.

Ste is the Stefane number and is define by: $Ste=\frac{C_P(\mathrm{T}_{WALL}-\mathrm{T}_{SOLIDUS})}{\lambda}$.

The first term on the R.H.S. of Equation (28) represents the buoyancy term. This term is implemented in the model as a linear source term (S) in the U-momentum equation. This source term can be written in the following form:

$$S = S_c + S_p\,\Phi_p \tag{29}$$

where S_c stands for the constant part of the source (S), while S_p is the coefficient of Φ_p (the dependent variable). Since in this case, the source term is not a function of the dependent variable (U), therefore it can be linearized in the following way:

$$S_c = \frac{Ra \Pr}{Ste}(h^* - h^*_{REF})\sin\theta\,, \tag{30}$$

and $S_p = 0$.

It is to be noted that h^* *and* h^*_{REF} represent the non-dimensional enthalpies of each scalar cell in the calculation domain (variable) and reference enthalpy, respectively. Unless a suitable adhoc method is used in the solution procedure of the momentum equations, the buoyancy term in the above discretized form can give rise to serious numerical instabilities in the solution process. In the present analysis, small under-relaxation factors were required to compute the buoyancy force terms.

3.4 Convergence Criteria

The discretized equations were solved iteratively using an implicit relaxation technique and by employing the well-known line-by-line Tri-Diagonal Matrix Algorithm (TDMA) solver until a converged solution was obtained for each time step. The termination of an iteration loop depended on the value of residuals for U, V, ∇P and T at any instant of time. At every time step, the iterations were terminated when the relative change to maximum values of the absolute residuals at every grid points for each calculated variable (R_Φ) was less than 10^{-5}. Mathematically, the convergence criterion described above can be defined as follows:

$$R_\Phi = \left|\frac{\Phi^{k+1} - \Phi^k}{\Phi^k_{Max}}\right| \tag{31}$$

where, k in the number of iterations. At each time step, the number of iterations needed to achieve convergence varied between 1000 and 500. The CPU time per iteration was about 1.5 s. The computations were performed on a personal computer having a speed of 1.83 GHz and fitted with a RAM of 2 Gigabytes. A block correction procedure (Patankar, 1980) was used to enhance the convergence of the solution procedure.

3.5 Under-relaxation factor

The nonlinearity and inter-linkage of the governing equations may appreciably change the results from iteration to iteration for every time step. These rapid changes influence the magnitude of the coefficients of the tri-diagonal matrix which then generally yields to the divergence. To prevent the program from divergence under-relaxation parameters were introduced for velocities and temperature. Use of the implicit form of under-relaxation before solution of the algebraic equations, changes the coefficients of these equations as follows:

$$\frac{a_{\mathrm{P}}}{\alpha_{\Phi}}\Phi_{\mathrm{P}} = \sum_{nb} a_{nb}\Phi_{nb} + b_{\Phi} + (1-\alpha_{\Phi})\frac{a_{\mathrm{P}}}{\alpha_{\Phi}}\Phi_{\mathrm{P}}^{\bullet} \quad (32)$$

where, α_{Φ} is the under relaxation factor for the general variable Φ. The suitable values of the relaxation factor were found from earlier modeling experience since they depend upon a number of factors (grid resolution, Rayleigh number, etc.). In the present study, much effort has been paid to find the relevant under-relaxation factors. Various combinations of under-relaxation factors were examined and after numerous runs the following under-relaxation factors were selected for the production runs:

α_u =0.3; α_v = 0.3; and α_T =0.3.

3.6 Code validation

To validate the code, it is necessary to compare the present predicted results with the experimental or numerical results of the same phase-change problem during melting under identical operating conditions provided by other researchers. Unfortunately, in the literature there is no suitable study, either experimental or numerical, for the same phase-change problems modeled here. In the existing numerical studies in most of the cases the authors neither mentioned the time steps used nor did they provided the small difference of temperature between the liquidus and solidus temperatures which they used in order to handle the artificial mushy zone necessary for the implementation of the enthalpy-porosity method for pure phase-change materials.

In order to verify the present code, the accuracy of the present numerical results was investigated by computing the steady state natural convection heat transfer in a concentric horizontal annular for a single phase fluid for which both experimental and numerical results are available in the literature. Various authors have studied this configuration in detail and established to an extent that is used as a source of comparison for validating the CFD codes. In this section, the present numerical code is defaulted to steady state for a non-phase change natural convection problem and is extensively validated against the experimental and numerical results of Kuhen and Goldstien (1976, 1978) and numerical results of Hessami et al. (1984), Yang et al. (1988), Marie-Isabelle et al. (1997). In Table 3.2 the present numerical results are compared with the available experimental results of Kuhen and Goldstien (1976) and numerical results of others. In generating results using the present code, the exact numerical values of the dimensionless parameters were chosen as others so as to make a direct comparison with the available experimental and numerically predicted data. An equivalent thermal conductivity K_{eq} on the outer surface of the inner cylinder and inner surface of the outer cylinder was used to compare the accuracy of the present computations. This dimensionless parameter is defined as the ratio of actual heat flux to the heat flux that would have occurred due to pure conduction without the convective motion of the working fluid.

Many authors have used the value of K_{eq} on the inner and outer cylinders as a suitable criterion for testing the accuracy of their numerical procedures. This choice may yield an error in computing the actual heat transfer rate since various authors have used various expressions for calculating conductive heat transfer rates. The definition of circumferential average equivalent thermal conductivity ($\bar{K}_{eq_{inner}}$) and local equivalent thermal conductivity K_{eq} along the inner cylinder is given below:

$$\overline{K}_{eq_{inner}} = \frac{\overline{Nu_{avg}}}{Nu_0} \quad \text{and} \quad K_{eq} = \frac{Nu_L}{Nu_0}$$

$\overline{Nu}_{avg}$ = circumferential average Nusselt number based on cylinder radius, is calculated as

$$\overline{\mathrm{Nu}}_{avg} \text{ at r=r}_{\mathrm{i}} = \frac{\int_0^L \int_0^\pi (Nu_L)_{r=r_i} r_i d\theta dZ}{\int_0^L \int_0^\pi r_i d\theta dZ} \text{; and } Nu_{L\ at\,r=r_i} = \frac{h(\theta) r_i}{k} \text{; where, } h(\theta) = \frac{q_w}{\mathrm{T}_w - \mathrm{T}_{ref}} \text{;}$$

$$q_{w \text{ at r=r}_{\mathrm{i}}} = -k \frac{\partial \mathrm{T}(r_i, \theta)}{\partial r}$$

Nu_0 = Nusselt number for conduction between the annuli. The subscript "o" indicates Nusselt number for conduction heat transfer in the annulus. This is obtained by solving the one-dimensional conduction equation at steady state which is given by

$$\frac{1}{r} \frac{\partial}{\partial r} \left(kr \frac{\partial \mathrm{T}}{\partial r} \right) = 0$$

The Nusselt number for conduction is evaluated as

$$Nu_0 = \frac{1}{\ln \frac{R_0}{R_i}}$$

In this study, one-dimensional radial heat conduction equation was solved to compute the heat flux by neglecting the fluid motion in the annulus. In the literature, Nusselt number for conduction is evaluated by solving the steady state two-dimensional heat conduction equation by some of the authors. It can be seen from Table 3.2 that the present numerical results are in very good agreement with the experimental results of Kuhen and Goldstien (1976) for Ra = 5×10^4, Pr = 0.7 and non-dimensional diameter ratio of 2.6. The percentage of error was calculated with respect to the experimental results reported by Kuehn & Goldstein. The difference between the available experimental and the present numerical results for Nusselt numbers is seen to be less than about 1.5% for the inner cylinder and about 2.2% for the outer cylinder. The errors in the numerical results may be due to the constant-property assumption or the finite number of nodes or the convergence criterion used, etc. The numerical modeling has the advantage of obtaining and observing the velocity field in the cylindrical annulus which is difficult to observe experimentally. In addition, an overall energy balance was made at steady state, i.e., the integrated heat transfer rate through the inner cylinder must be equal to that of the outer cylinder. The discrepancy in the integrated total heat transfer at the inner and outer cylinders was found to be less than 3.6%.

Table 3.2: Comparison between numerical results for Ra=5.0X10^4 and Pr=0.7 (air)

	Kuehn & Goldstein exp. (1976)	Kuehn & Goldstein num. (1976)	Hessami et al num. (1984)	Yang et al num. (1988)	Marie et al num. (1997)	Present numerical computation
Ra_L	4.7X10^4	5.0X10^4	5.0X10^4	4.7X10^4	5.0X10^4	5.0X10^4
Pr	0.706	0.7	0.7	0.7	0.7	0.7
$\bar{K}_{eq_{inner}}$ on inner cylinder	3.0	3.024	3.26	2.943	2.955	3.044
Percent error	0.0%	0.8%	8.7%	1.9%	1.5%	1.5%
$\bar{K}_{eq_{outer}}$ on outer cylinder	3.0	2.973	3.05	2.901	2.955	2.935
Percent error	0.0%	0.9%	1.7%	3.3%	1.5%	2.2%

In Figure 3.5 a comparison is made between the results obtained from the present code and Kuhen and Goldstien's (1976) numerically predicted local equivalent thermal conductivities along the inner and outer cylinders for Pr numbers 0.7, 1.0 and 5.0; L/D_i=0.8; all for a fixed Rayleigh number of 10^4. The present results were obtained using the control volume finite difference scheme and by employing a uniform grid distribution system of 42 x 42 (r-θ) grids. It is observed from Fig. 3.5 that the present results are very similar to the ones presented by Kuhen and Goldstien. These authors also published results of averaged equivalent thermal conductivity for the same conditions and these results are compared in Table 3.3. There is an excellent agreement between the present results and the results reported by Kuhen and Goldstien; the average equivalent conductivities differ by less than 5% (1.99% for the inner cylinder and about 3.59% for the outer cylinder). This small difference may be due to the lower convergence criterion used by Kuhen and Goldstien which was 10^{-3} and in the present simulation study a stricter convergence criterion (10^{-4}) was used. Besides the above difference, Kuhen and Goldstien used an arbitrary set of non-uniform grids while in the present simulation a higher density but uniform grid system was used.

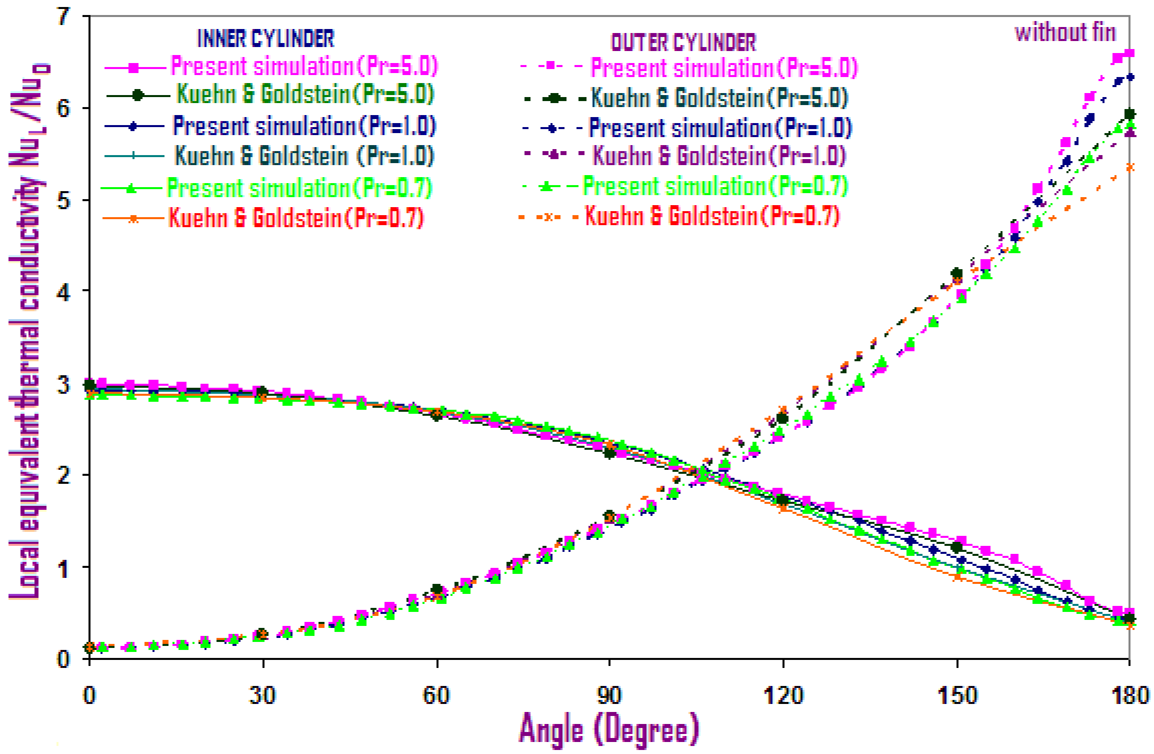

Figure 3.5: Present numerical predictions versus numerically predicted data of Kuehn and Goldstein (1976) for Pr= 0.7, 1.0 and 5.0 at Ra=10^4 and L/D_i=0.8

Table 3.3: Comparison between numerical results of average equivalent thermal conductivity for annulus width to inner cylinder diameter ratio (L/D_i) of 0.8

	Kuehn & Goldstein num. (1976))	Present numerical computations	Kuehn & Goldstein num. (1976)	Present numerical computations	Kuehn & Goldstein num. (1976)	Present numerical computations
Ra_L	10^4	10^4	10^4	10^4	10^4	10^4
Pr	**5.0**	**5.0**	**1.0**	**1.0**	**0.7**	**0.7**
$\bar{K}_{eq_{inner}}$ on inner cylinder	2.069	2.119	2.038	2.089	2.010	2.05

Percent error	0.0%	**2.42%**	0.0%	**2.50%**	0.0%	**1.99%**
$\bar{K}_{eq_{outer}}$ on outer cylinder	2.066	1.994	2.039	1.951	2.005	1.933
Percent error	0.0%	**3.48%**	0.0%	**4.32%**	0.0%	**3.59%**

3.7 Grid independency tests

In order to determine an appropriate grid density distribution for the solution domain, the grid independency tests were performed. In this study, the grid distribution in the r-θ coordinates was uniform, except near the walls where non-uniformity was due to the employment of B-type staggered grids (Patankar, 1980). In order to tests the grid independency of the generated numerical solution for the convective phase-change melting problem, the total energy accumulated during the melting process in the domain for a total time of 41 minutes was used as a verification criterion. Four grid distributions were selected for the tests. These were 62 x 62, 82 x 82, 102 x 102, 122 x 122 grids, where the first number represents the number of grids in the r-direction and the second number represents the number of grids in the θ direction. All of the grid independency tests were carried out for a fixed inner cylinder wall temperature of 69.9 ^{0}C and the corresponding Rayleigh number, and Stefan number were 1.09x10^6, and 0.2116, respectively. The non-dimensional time step was taken as 5 x 10^{-4}, which corresponds to the dimensional time of 6.2 seconds. The initial temperature of the solid PCM was taken as 41.2^{0}C which translated to a sub-cooling parameter (initial Stefan number), Ste_i = 0.113. As can be seen from the Table 3.4, less than 2% differences in the total energy stored were found with respect to the grid distributions of 122 x 122 during the melting process. To lend credibility in the results and for the sake of numerical accuracy, the highest grid system having 122x122 grids was chosen for all production runs.

Table 3.4: Effect of grid points on total energy at time 41 min when the time step ($\Delta\ \tau$) was 5x10^{-4}

Grid points	62x62	82x82	102x102	122x122
Total stored energy (kJ)	430.1034	426.6417	425.3563	421.6918
Percent error	**1.99%**	**1.17%**	**0.87%**	**0.0%**

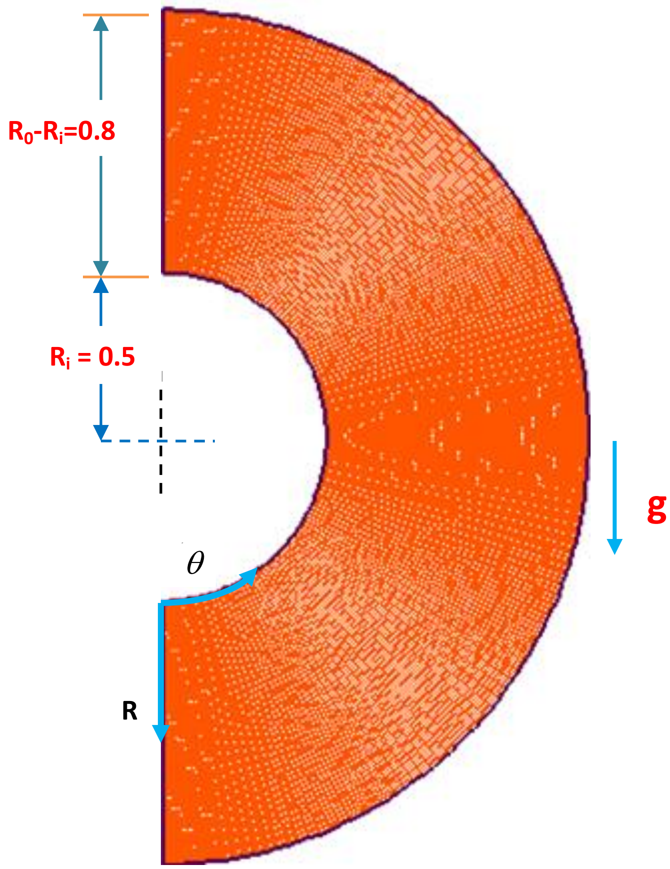

Figure 3.6: Sample grid arrangements for 122 x 122 grids in the calculation domain

3.8 Time independency tests

Before embarking on production runs, the time independency tests were also carried out. The aim of such an exercise is to obtain an optimum time step that will generate results which will not change the results significantly if the time step is further decreased. As mentioned earlier, an equally spaced B-type staggered grid meshes of 122x122 grids were used to discretize the governing equations for the phase-change melting problem. The parameters selected for the tests were Ra = 1.09×10^6, and Ste = 0.2116 (which corresponds to inner cylinder wall temperature of 69.9^0C for the commercial PCM, paraffin wax) and initial sub-cooling, Ste_i = 0.113. Three different dimensionless time steps, namely, 1.25×10^{-4}, 2.5×10^{-4}, and 5×10^{-4} were tested for the time step independency test. The total energy accumulation in the annulus for an elapsed dimensional time of 41 minutes was selected as a basis for the time-step independency tests. The tests results are shown in Table 3.5. Only about 3% variations in results were obtained for a non-dimensional time step of 2.5×10^{-4} compared to the dimensionless time step of 5×10^{-4}. For the sake of the computational economy and costs, all simulation runs were carried out using the bigger dimensionless time step ($\Delta\tau$) of 5×10^{-4}. The latter dimensionless time step corresponds to the dimensional time (Δt) of 6.2 seconds.

Table 3.5: Effect of time step on the total stored energy for 41 min of melting with 122x122 grids.

Time step ($\Delta\tau$)	1.25×10^{-4}	2.5×10^{-4}	5×10^{-4}
Total stored energy (kJ)	425.326	409.4935	421.6918
Percent error	**0.86%**	**2.89%**	**0.0%**

CHAPTER – FOUR

Melting of a Commercial PCM in a Plain Horizontal Cylindrical Annulus

4.1 Introduction

In this section, the numerical simulation results have been presented for the buoyancy-driven melting of a commercial PCM (paraffin wax) encapsulated between two concentric horizontal cylinders. The relevant thermo-physical properties of the PCM are taken from the literature and are given in the previous section in Table-3.1. The developed numerical model and the associated CFD code are able to track the transient progression of the melting process for any commercial PCM. The code is particularly able to handle the irregular movements of mushy zone due to natural convection and the interaction between the solid and liquid phases under laminar flow conditions. The mushy region is the region between the liquidus and solidus isotherms, where solid and liquid coexist in thermal equilibrium (Viskanta, 1988). During numerical simulation, it is quite difficult to track the mushy region at every instant of time. The present numerical code is written to solve the dimensionless form of the governing equations and hence the code is fairly general. The code can be used to investigate the melting phenomenon for multiple PCMs in the annulus. The model developed here takes into account both conduction in the three phases (unmelted solid, liquid, mushy zone) and induced natural convection in the two phases (melt and mushy region) where solid-liquid coexist.

In this section, the melting results are explained in terms of temperature distributions, velocity vectors, the total stored energy, the total liquid fraction, and the thermal efficiency at different time spans for various operating conditions for a plain annulus.

The total stored thermal energy equation can be derived by splitting the total energy stored in the melt into the sensible energy ($M_{PCM}C_P\Delta T$) component and the latent heat energy ($M_{PCM}\lambda$) component during the melting process for a fixed time span. In the present study, since phase change of a commercial material is the main concern, the volume of liquid melted is evaluated by summing the volume fraction of melt in every cell in the liquid phase and in the partially melted mushy zone at each time step. For the above calculations, correct identification of the mushy region is important to correctly account for the liquid fraction in that region. Because of the existence of the mushy region, the total liquid fraction can be derived as follows:

$$\text{Total liquid fraction} = \frac{\text{Total volume of liquid}}{\text{Volume of the annulus}}$$

$$\text{Total volume of liquid} = \sum_{i=1}^{n} f_i CV_i$$

$$f_i = \frac{\text{Volume of liquid in a i}^{\text{th}} \text{ cell}}{(\text{Volume of liquid} + \text{Volume of solid})\text{ in the i}^{\text{th}} \text{ cell}}$$

Here, 'n' represents the total number of control volumes.

$$\text{Thermal efficiency} = \frac{\text{Total stored energy at a fixed time period}}{\text{Maximum energy which can be stored in the calculation domain}} \text{ x } 100\,\%$$

The maximum stored energy within half of the annulus can be evaluated from the following expression.

Maximum storable energy, $Q_{max} = M_{PCM} [C_{PS} (T_S-T_i) + \lambda + C_{PL}(T_W-T_L)]$

For example, for an initial 10^0C sub-cooling and with the inner cylinder wall temperature at 69.9^0C for a commercial PCM, the maximum energy that can be stored is 666.18 kJ. It is to be noted that the PCM used here has a Prandtl number of 40.15 and the mass of this PCM (M_{PCM}) for half of the annulus is 2.86 kg when the length of the cylinders is assumed to be one meter.

Numerical simulations have been conducted by varying the various parameters associated with the model under consideration. The basic governing parameters of the system include Rayleigh number Ra, Stefan number Ste, radius ratio of the annulus R_0/R_i, initial sub-cooling parameter Ste_i, and Prandtl number Pr. The parameters, such as Rayleigh number, Stefan number, and Prandtl number appear in the non-dimensional governing equations. The radius ratio of the annulus and Stefan number appear in the boundary conditions. For the initial condition, the initial sub-cooling parameter Ste_i appears in the modeled equations. For all the production runs reported here the Prandtl number is assigned a value of 40.15, which corresponds to commercial paraffin wax used in this study. The ratio of the outer radius to the inner radius of the pipes is assigned a value of 2.6. The remaining two parameters, namely, Rayleigh number and the initial Stefan number are varied.

As mentioned earlier, in the present study emphasis is placed in asserting the melting behavior of paraffin wax for the purpose of thermal energy storage. For a fixed phase-change material (fixed Prandtl number), the Stefan number and Rayleigh number cannot be varied independently. During parametric study the diameter of the inner cylinder (D_i) is fixed to a value of 0.04 m and the temperature differential ($\Delta T = T_{inner\ cylinder\ wall} - T_{Solidus}$) is varied in order to assess the role of buoyancy-driven convection during melting. Table-4.1 gives the pertaining process parameters for the computed cases. When the Rayleigh number is fixed, the Stefan number is also consequently fixed, as a result for a specific PCM only inner cylinder wall temperature dictates the value of the Rayleigh number. The initial temperature of the PCM is also a parameter to be specified. When the initial temperature of the PCM is below the solidus temperature, this condition is referred to here as the sub-cooled condition. The initial temperature of the PCM is assumed to be at 41.2^{0}C which is 10^{0}C ($\Delta T = T_{solidus} - T_{initial}$) lower than the solidus temperature for one case and for the second case the initial temperature of the PCM is assumed to be at the solidus. The latter case is referred to as the zero sub-cooling condition. Following other researchers in this field, the porosity constant C in the Darcy term is set to 10^6 kg/(m^3 s) so that the fluid velocity in the momentum equation becomes zero in the solid region.

Table 4.1: Computational cases studied (Pr = 40.15, diameter of the inner cylinder, D_i = 0.04m)

Inner cylinder wall temperature T_W [^{0}C]	ΔT = ($T_{wall} - T_{Solidus}$) [^{0}C]	Rayleigh number (Ra)	Stefan number (Ste)	Melting time (t / τ) [min/dimensionless]
69.9	18.7	1.09×10^6	0.2116	(a) 20/0.1 (b) 41/0.2 (c) 62/0.3 (d) 83/0.4
74.9	23.7	1.38×10^6	0.2682	(a) 20/0.1 (b) 41/0.2 (c) 62/0.3 (d) 83/0.4

79.9	28.7	1.67×10^6	0.3248	(a) 20/0.1 (b) 41/0.2 (c) 62/0.3 (d) 83/0.4

A set of simulations are carried out for the plain annulus considering the fixed initial sub-cooling [i.e., $\Delta T = T_{solidus} - T_{initial}$] of 10^0C, and 0^0C and for various process parameters listed in Table-4.1. Numerical simulations results are presented pictorially in the form of velocity vectors and temperature contours. The quantitative values for the total stored energies, the total liquid fractions and the energy fractions are also provided. It is to be noted that, in selecting the various ranges of the relevant parameters, the primary consideration has been to clarify the influences of the sub-cooling parameter and the Rayleigh number. Accordingly, the simulations are carried out for three Rayleigh numbers, namely, 1.09×10^6, 1.38×10^6, and 1.67×10^6. In order to avoid confusion, the simulation results for three Rayleigh numbers are discussed separately. The discussion of the velocity fields will be followed by a discussion of the temperature fields. The total stored energy, the total liquid fraction and the energy efficiency for the melting process are explained subsequently for three situations.

4.2 Flow structure and melt shape for different Rayleigh numbers

Instantaneous velocity fields in the liquid and mushy regions and the temperature distributions in both liquid and solid regions during the melting process in a plain annulus are given in Figs. 4.1 (a-c) for $\Delta T = 18.7^0$C; in Figs. 4.2 (a-c) for $\Delta T = 23.7^0$C; and in Figs. 4.3 (a-c) for $\Delta T = 28.7^0$C. In each figure three instantaneous plots are provided for dimensionless time of τ = 0.2, 0.3 and 0.4 which correspond to the dimensional time of t = 41 min, 62 min, and 83 min, respectively. The velocity patterns are shown on the left-half of each circular cross-section whereas the temperature contours are presented on the symmetric right-half separated by a vertical line passing through $\theta = 0^0$ and $\theta = 180^0$. The simulations are carried out for a sub-cooling parameter, $Ste_i = 0.113$.

4.2.1. Case (a) (Ra = 1.09×10^6, which corresponds to the inner cylinder wall temperature of 69.9^0C):

Velocity and temperature fields for $\Delta T = 18.7^0$C and $Ste_i = 0.113$ (inner cylinder wall temperature of 69.9^0C) are given in Figs. 4.1(a-c) for three dimensionless time instants ($\tau = 0.2$, 0.3, and 0.4).

Velocity field

Since the inner cylinder wall temperature for this case is 69.9^0C, which is 10^0C higher than the melting temperature of the PCM, the solid starts to melt initially due to conduction. As melting time progresses, the natural convection is intensifying, as a result, convection currents in the melt start to move around the inner cylinder wall from the bottom to the top until it reaches the upper symmetry plane. At this point, the melt is forced to bend and flows downward along the relatively cold outer cylinder prevailing on the inner surface of the outer cylinder. The heated downward melt meets with colder solid when moving down along the outer cylinder. The resistance force created by the solid causes the deceleration of the downward motion of the melt and melting proceeds on the top of the annulus in the angular and radial directions due to conduction and buoyancy driven convection. The velocity profile shows that throughout the melting process the natural convection flow in the melt region remains unicellular i.e., has only a single recirculation zone. Due to the small annulus gap, the Rayleigh number is relatively low for this case and the established buoyancy-driven convection is not strong in comparison to conduction. Thereafter, the recirculation zone do not shift downward with increase in melting time as needed, and as a result, the shape of the mushy region did not expand in the downward direction, thus hampering the progression of melting in the lower region of the annulus. From the velocity field it is clear that melting has been more intense in the top portion of the annulus. Figures 4.1a to 4.1c also show the history of the resultant maximum velocity in the melt. The maximum velocity represents the strength of the buoyancy force which appears at around 41 minutes. At the beginning, the fluid flow is weak all over the thin circular annulus. As the melting process marches on, the melt gets hotter and gain strength, thereby the maximum resultant velocity increases with time. The melt velocity reaches approximately its maximum value at around 41 minutes. After this melting time the recirculation fluid cell at the top region

(θ ~90^0 to 180^0) of the annulus remains more or less stagnant due to the development of stratified temperature field there. The manifestation of the latter fact is that, with the increase of melting time the magnitude of the maximum velocity inside the annulus decreases.

Temperature field

Figures-4.1(a-c) show the temperature contours in a flooded format for the half of the cross-section of the annulus including the liquidus (59.9^0C) and solidus (51.2^0C) isotherms. The mushy layer, presented by the blue color, is located between these two isotherms. The concentrated temperature contours on the lower part of the inner cylinder wall indicates that the maximum heat transfer rate occurs in this part. This perfect cylindrical shape of the temperature contours during melting process indicating the dominance of the conduction mode of heat transfer. As the isotherms begin to follow the inner cylinder wall boundary, it starts to separate from the inner cylinder surface and deviate from the concentric ring patterns to form a pear-shaped melted region, indicating that convection begins to affect the melting process. The separation of the isotherms from the inner cylinder wall indicates that the heat transfer between the melt and the inner wall decreases smoothly. Since the melting temperature is lower than the inner cylinder wall temperature and the isothermal boundary condition is imposed on the inner cylinder surface, the larger temperature difference between the melt and the heated surface results in a larger heat transfer rate near the lower portion of the inner cylinder wall. As the melt moves upward along the inner cylinder wall, the melt is being heated up. The temperature difference between the wall and the melt is reduced gradually during upward movement of the melt and as a consequence the heat transfer rate decreases. Convective current leads to the movements of the isotherms outward from the inner cylinder wall and thereby distorting the isotherms in the upper part of the annulus. While going down from the top of the annulus to bottom, the pear-shaped isotherms start to turn to become horizontal in shape suggesting that the convection has been replaced by the conduction mode of heat transfer. At the lower part of the annulus the heat transfer is controlled predominantly by conduction for all the three dimensional time instants (t = 41 min, 62 min, and 83 min) as shown in Figs. 4.1(a-c).

Figure 4.1(c) shows that for a melting time of 83 min, the convective motion of the melt starts intensifying at the top. For example, the 68.15^0C isotherm near the top of the annulus

(θ~180^0) is pear shaped and it is gradually decreasing in the downward direction, as is evidenced by the isotherm at 67.11^0C (θ~150^0), which is a deformed and almost horizontal-shaped isotherm in the melt region. From the nature of the predicted isotherms one can clearly identify the established conductive and convective regimes inside the annulus. A further examination of this figure reveals that with the increase of melting time, the densely packed isotherms manifest in the same direction as gravity and as a result the heat transfer rate is enhanced in this region.

With the increase of melting time the hot melt comes down along the cold mushy region. It then loses energy and thereby gets colder and finally arrives at the bottom of the solid zone. In the bottom region (θ~0^0 to 90^0), the conduction mode of heat transfer is significant due to the horizontal geometrical configuration of the annulus and this conduction mode of heat transfer is further aggravated by the low thermal conductivity of the PCM. Looking at the point of onset of melting inside the annulus [Figs. 4.1(a-c)], it can be seen that as time progresses from 41 min to 83 min, the mushy layer remains practically stagnant at the lower portion of the annulus (θ~80^0). As a result, the melting rate in the bottom region (θ~80^0) is significantly slower than any other regions within the annulus. A similar phenomenon has been reported by other researchers in the literature during melting of a pure PCM within horizontal concentric cylinders.

These figures clearly demonstrate that with the progression of melting time the phase-change process practically stops. This is not beneficial for energy storage since only sensible energy, which is much less compared to the latent energy, is stored during this time.

4.2.2. Case (b) (Ra = $1.38\text{x}10^6$, which corresponds to the inner cylinder wall temperature of 74.9^0C):

Velocity and temperature fields for $\Delta T = 23.7^0$C and initial sub-cooling parameter, $Ste_i = 0.113$ (case (b) inner cylinder wall temperature of 74.9^0C) are given in Figs. 4.2(a-c) for three dimensionless time instants (τ = 0.2, 0.3, and 0.4).

Velocity field

Figs. 4.2(a-c) show the resultant maximum velocity in the melt is enhanced compared to the case (a). The figures are indicating more intense melting in the top portion of the annulus gap. Since the Rayleigh number is high, fluid motion is stronger, which can be seen from the resultant values of the maximum velocities in the above mentioned three cases. For example, the resultant value of the maximum velocity is 0.00163 m/sec at the time instant of 41 min for Ra = 1.38×10^6 depicted in Fig. 4.2(a), whereas at Ra = 1.09×10^6, the resultant value of the maximum velocity is only 0.0015 m/sec for the same time instant [Fig. 4.1(a)]. It is noted that the counter-clockwise-rotating recirculation cell in the melt is relatively stronger when compared to case (a). The pattern of velocity field is similar to that of case (a).

Temperature field

As the inner cylinder wall temperature is enhanced by 5^0C compared to case (a), a strong thermal plume originates near the top of the annulus and impinges perpendicularly on the top of the outer cylinder wall (θ~180^0), shown in Figs. 4.2(a-c). Consequently, the progress of the melt front in the top region is greatly enhanced. At 41 min, the 68.15^0C isotherm for Ra = 1.38×10^6 is at the middle of the annulus (θ~90^0) and has appeared as a horizontal line which is seen in Fig. 4.2(a). The same isotherm for the same time instant for Ra = 1.09×10^6, which has appeared at the top of the annulus (θ~180^0), is a pear shaped melted regime which is seen in Fig. 4.1(a). It is evident from these figures that melting rate enhances with increase of Rayleigh number. The right-hand sides of the above mentioned figures [Figs. 4.2(a-c)] display the transient progressions of the temperature contours in the melt, mushy region and solid PCM.

Next, attention is turned to the lower part of the annulus. Due to conduction dominated heat transfer in the bottom region, the mushy region represented by the blue color is practically stagnant. At this stage, the qualitative features of the movement of the mushy zone appear to be at the same position similar to case (a). Conduction dominated bottom regime of the annulus remains unaffected for a higher Rayleigh number, seen in case (b).

4.2.3. Case (c) ($Ra = 1.67x10^6$, which corresponds to the inner cylinder wall temperature of 79.9^0C):

Velocity and temperature fields for $\Delta T = 28.7^0C$ and $Ste_i = 0.113$ are given in Figs. 4.3(a-c) for three dimensionless time instants (τ = 0.2, 0.3, and 0.4).

Velocity field

This case represents a relatively high Rayleigh number, so the effects of buoyancy-driven convection are more pronounced compared to the previous two cases. At the highest Ra = $1.67x10^6$, the velocity field in the melt shows a stronger convection pattern compared to the cases (a) and (b). Although the recirculation zone is found to be almost in the same location as cases (a) and (b), but the strength of the recirculation zone is enhanced for this case. The resultant value of the maximum velocity is found to be 0.00194 m/sec at the melting time of 41 min as seen in Fig. 4.3(a), which is the greatest compared to the previous two cases (a) and (b).

Temperature field

Compared to case (a) when the inner cylinder wall temperature is enhanced by 10^0C, an accelerated melting occurs in the very top region and the melting rate is the greatest compared to the cases (a) and (b). This is due to the fact that because of the higher wall temperature there exist a high temperature gradient in the melt for the same time span compared to the other two cases. It follows that the most sensible energy is stored in the liquid region for this case. The Rayleigh number for this case being the largest among the three cases studied, but the mushy region which is bounded by the liquidus (59.9^0C) and solidus (51.2^0C) isotherms remains practically at the same angular and radial positions due to conduction-controlled zone prevailing in that region which can be seen from Figs. 4.3(a-c) and is very similar to cases (a) and (b).

4.3. Total stored energy, total liquid fraction and energy efficiency for different Rayleigh numbers in plain annulus

In order to assess the overall role of convection on the melting process, the total stored energy, the total liquid volume fraction and the thermal efficiency for three cases (a)-(c) are plotted in

Figs. 4.4(a,b) for case (a), in Figs. 4.5(a,b) for case (b), and in Figs. 4.6(a,b) for case (c). The numerical calculation procedure for the total stored energy, the total melt volume fraction and the fraction of energy stored are all given in Section 4.1 of this chapter. Figures 4.4(a), 4.5(a), and 4.6(a) present in graphical form the total stored energy and the total liquid volume fraction as a function of dimensional time for three prescribed temperatures of the inner cylinder wall. Figures 4.4(b), 4.5(b), and 4.6(b) present the curves of energy fraction as a function of dimensional time for the same wall boundary conditions as Figs. 4.4(a), 4.5(a), and 4.6(a) respectively. An inspection of the above figures reveal that at the early stage of the melting process the rate of melting is almost linear and the total stored energy, the total melt volume fraction, and the energy efficiency all increase rapidly as the melting time increases. This happens due to conduction and convection induced melting process. With time, as the melt gets heated the temperature difference between the inner cylinder wall and the melt reduces. As a result the heat transfer rate from the inner cylinder to the melt also decreases. With the further progression of time the melting rate of the PCM is greatly reduced, which can be seen from the flattening of the curves in the figures for all the three cases. It can be concluded that the melting proceeds efficiently in a concentric cylindrical annulus up to a fixed melting time. After this threshold time the thermal efficiency, total stored energy and the rate of melting increases very slowly because of the marked suppression of natural convection. The threshold melting time is found to be about 41 minutes for the three cases studied here. It has been found that for $1.09 \times 10^6 \leq Ra \leq 1.67 \times 10^6$, the influence of the Rayleigh number on the amount of energy storage after this threshold melting time is insignificant because the heat transfer process is dominated by the conduction mode of heat transfer during which time predominantly sensible energy is stored in the melt and the above statement is particularly true for the bottom of the annulus. A quantitative comparison of the total stored energy, the total melt volume fraction and thermal efficiency is made in Table 4.2, showing the effect of Rayleigh number (wall temperature) for initial sub-cooling parameter, $Ste_i = 0.113$ for a melting time of 41 minutes. From this table it is evident that for cases (b) and (c) representing wall temperature of 74.9^0C, and 79.9^0C respectively, at the threshold time of 41 min, all of the predicted quantities are enhanced considerably compared to the base case (a) ($Ra = 1.09 \times 10^6$, $T_{WALL} = 69.9^0$C). After the threshold time and at t = 62 min, the total stored energy is 442 kJ for case (a) ($Ra = 1.09 \times 10^6$), which in comparison to the melting time of 83 min, is only 0.9 % less. Whereas, at threshold time, t = 41 min, the total stored energy is 422 kJ for the same case (a), which in comparison to the lower melting time of 20 min, is 40 % higher and in comparison to the higher melting time of 62 min, it is only 5% lower. From the above quantitative analysis it can be concluded that for the studied plain annulus it is not beneficial to store energy beyond the threshold melting time of about 41 minutes, since after this time mainly sensible heat storage takes place.

Table-4.2: Effect of Rayleigh number (wall temperatures) on total stored energy, total liquid fraction and fraction of possible maximum sorted energy compared to the base case (a) for a melting time of 41 min.

Quantity	Ra = 1.09×10^6	Ra = 1.38×10^6	Ra = 1.67×10^6
Total stored energy (kJ)	422	6 % higher than case (a)	12% higher than case (a)
Total liquid fraction (%)	68	3 % higher than case (a)	5% higher than case (a)
Energy fraction (%)	64	2 % higher than case (a)	3% higher than case (a)

The overall findings for the plain annulus are summarized below in Table-4.3.

Table-4.3: Summery of the findings along with the general remarks from the numerically predicted results for a plain annulus with initial sub-cooling parameter, $Ste_i = 0.113$.

Geometry	**Parameters studied**	**Effect of melting time**	**Effect of inner cylinder wall temperature**	**Remarks**
Plain annulus	The inner cylinder wall temperature is assigned to 69.9^0C, 74.9^0C, and 79.9^0C.	With the increase in time, initially the melting rate increases but the rate progressively decrease with time and reach almost a plateau with time in each case.	For the increase of the inner wall temperature, the melting rate increases, and also the total energy stored and the energy fraction increases.	Conduction dominated zone at the lower part of the annulus drastically inhibits the development of convection in the melt in all the three cases.

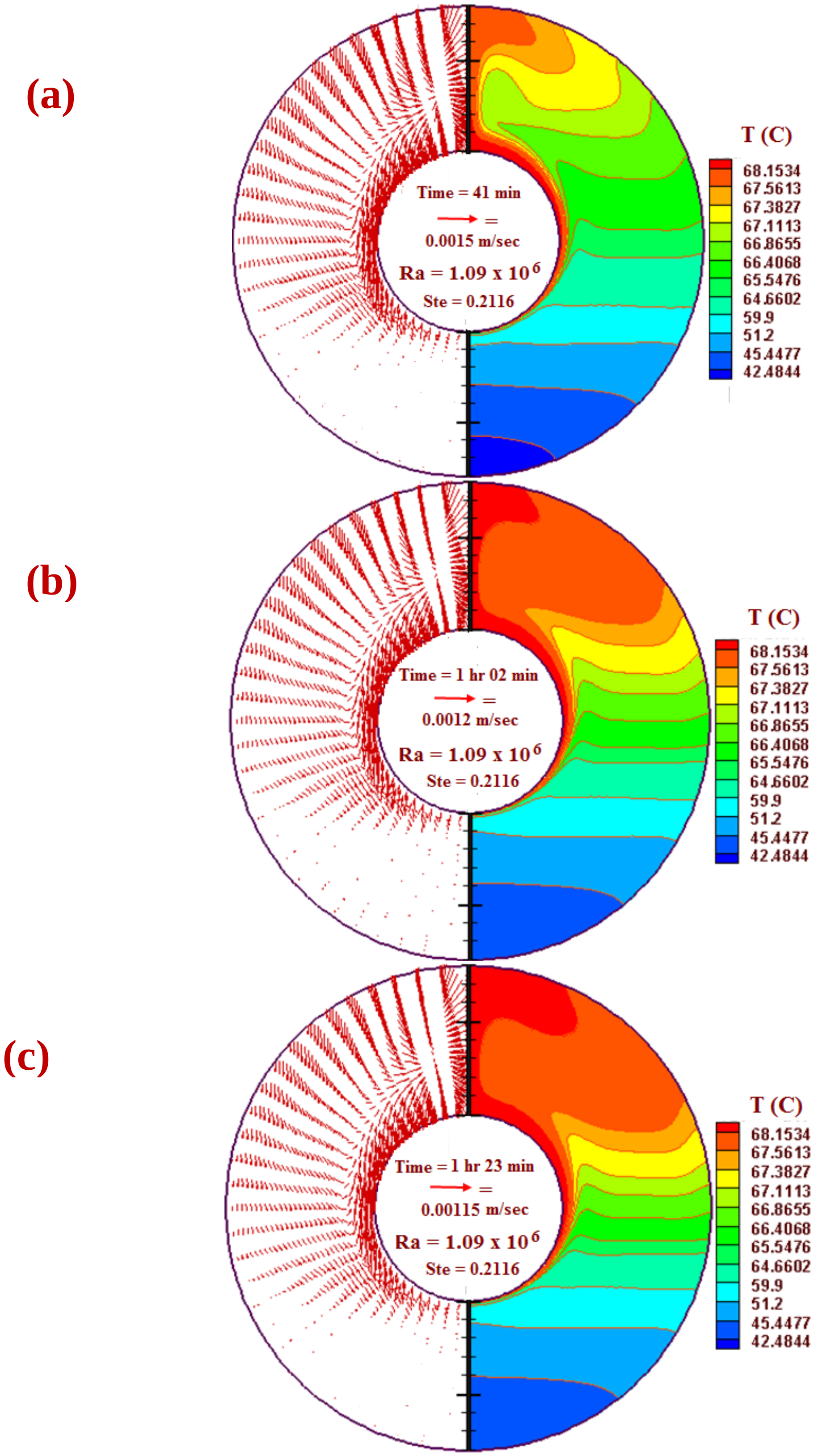

Figure 4.1: Temperature contours (right) and velocity vectors (left) for inner wall temperature of 69.9^0C for a plain annulus: $Ste_i = 0.113$, at time, (a) 41min; (b) 62min; (c) 83min.

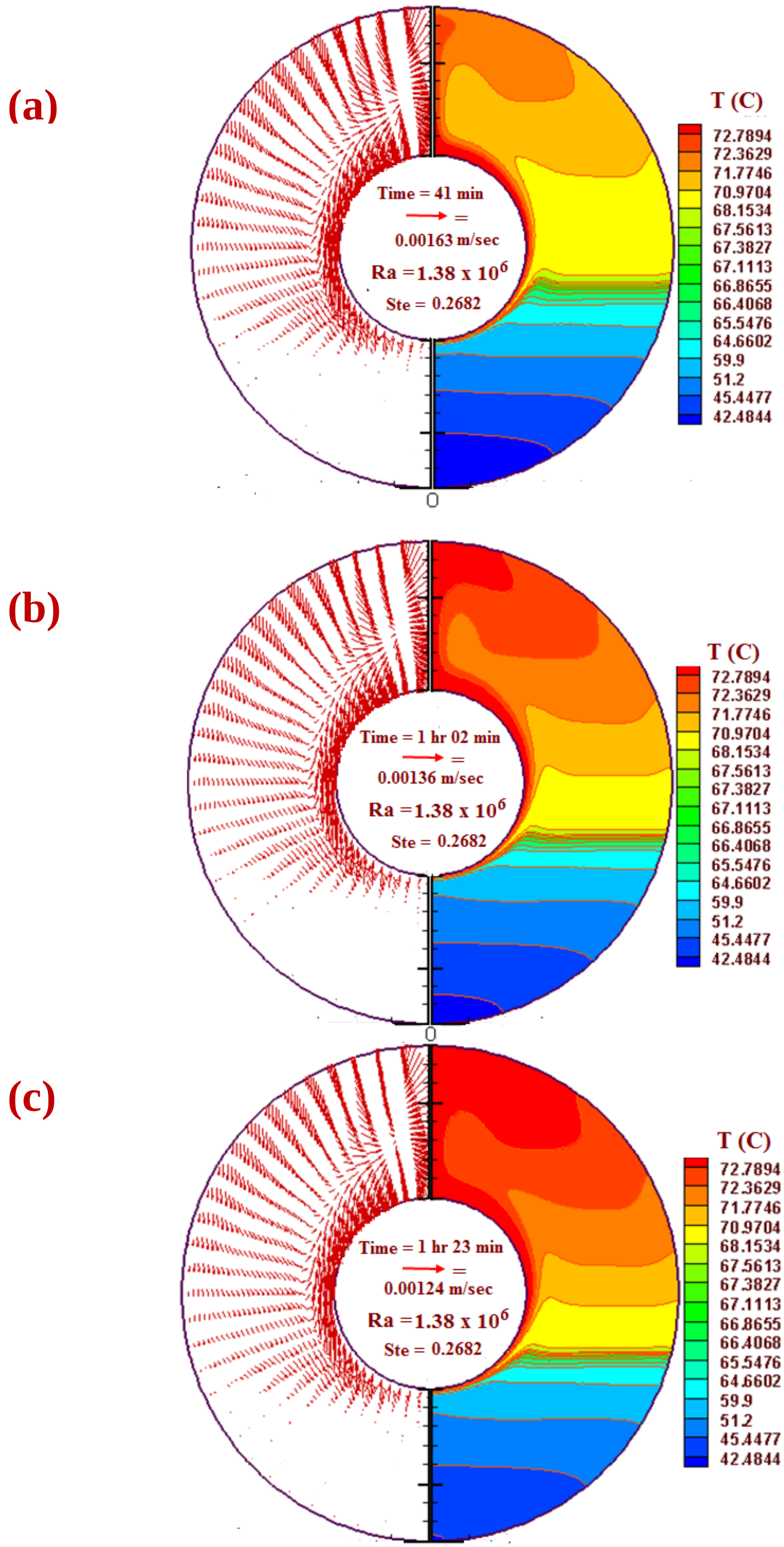

Figure 4.2: Temperature contours (right) and velocity vectors (left) for inner wall temperature of 74.9^{0}C for a plain annulus: Ste$_i$ =0.113, and at time, (a) 41min; (b) 62min; (c) 83min.

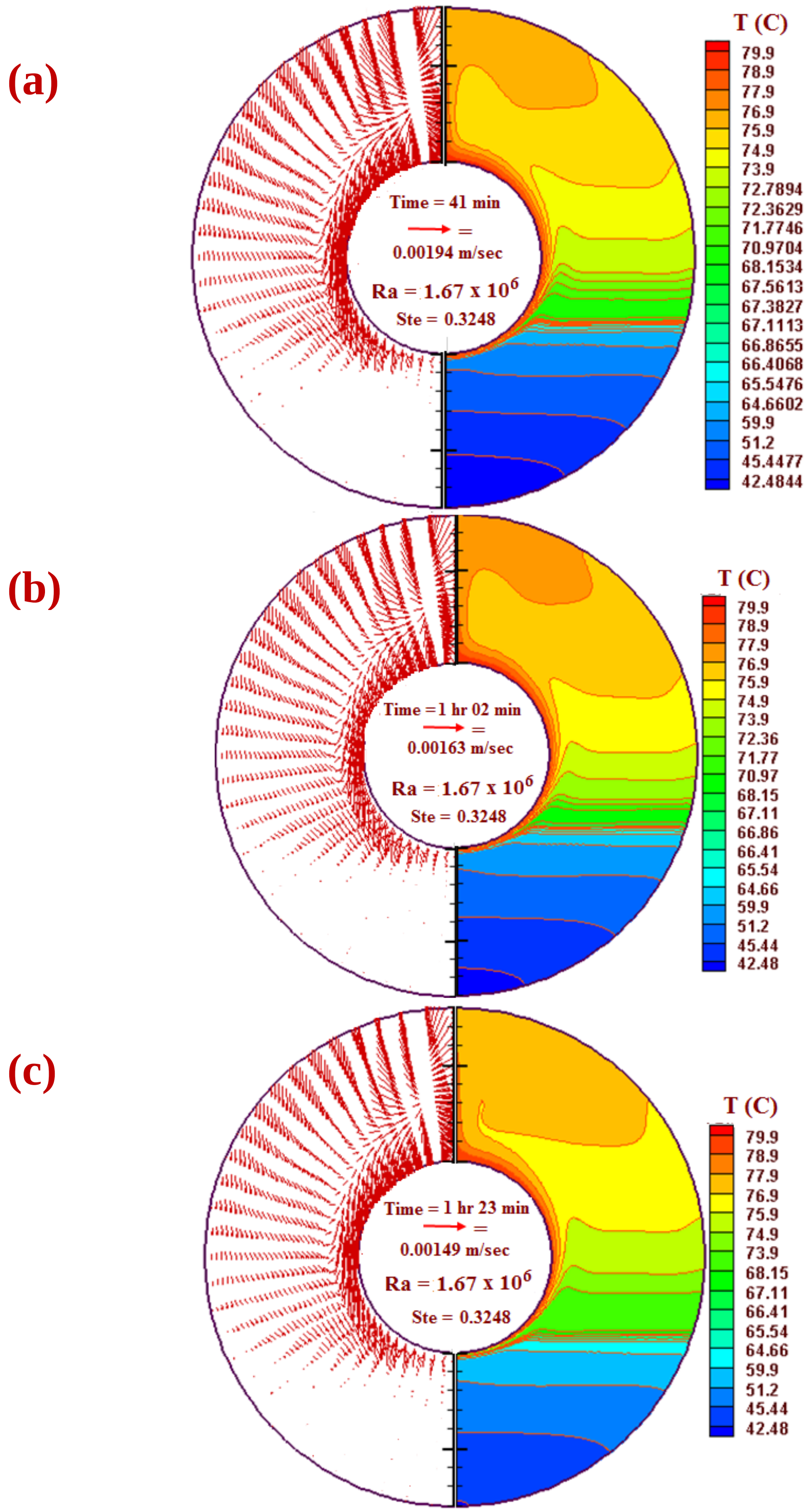

Figure 4.3: Temperature contours (right) and velocity vectors (left) for inner wall temperature of 79.9^0C for a plain annulus: $Ste_i = 0.113$, and at time, (a) 41min; (b) 62min; (c) 83min.

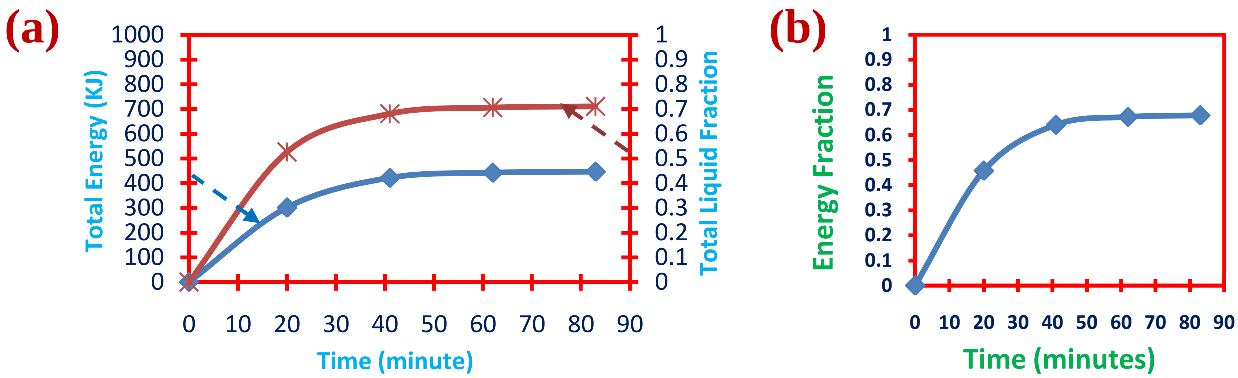

Figure 4.4: For T_{WALL}= 69.9 ^{0}C, Ste_i = 0.113 for a plain annulus: (a) transient evolutions of total stored energy (kJ) and total liquid fraction; (b) transient evolutions of energy fraction.

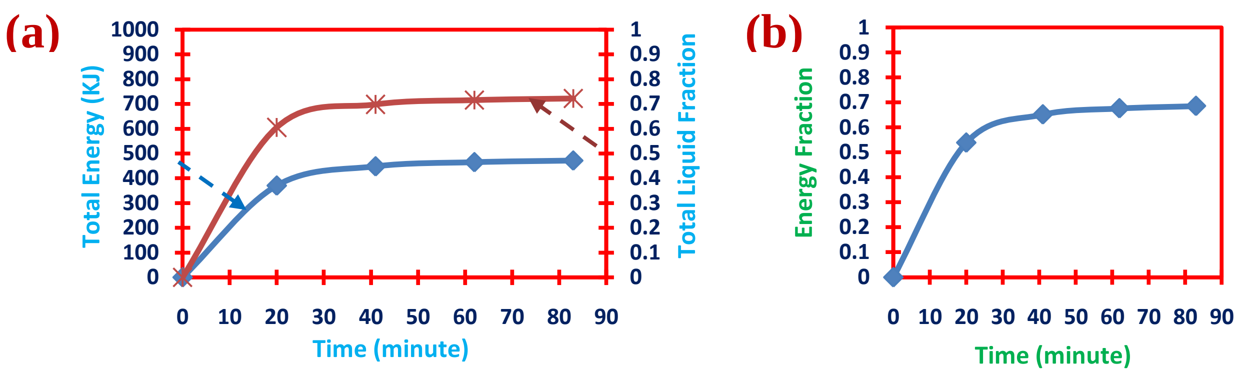

Figure 4.5: For T_{WALL}= 74.9 ^{0}C, Ste_i = 0.113 for a plain annulus: (a) transient evolutions of total stored energy (kJ) and total liquid fraction; (b) transient evolutions of energy fraction.

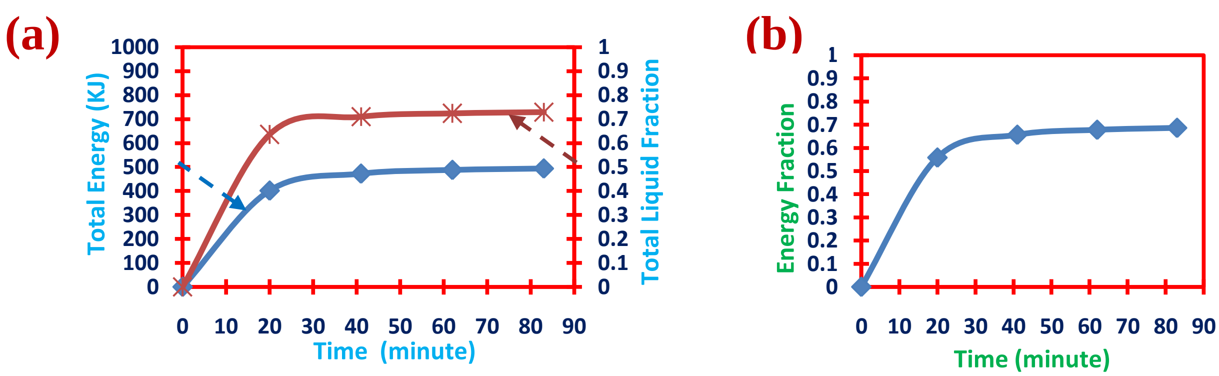

Figure 4.6: For T_{WALL}= 79.9 ^{0}C, Ste_i = 0.113 for a plain annulus: (a) transient evolutions of total stored energy (kJ) and total liquid fractions, (b) transient evolutions of energy

CHAPTER – FIVE

Melting of a Commercial PCM in a Finned Annulus

5.1 Introduction

Numerical results for a commercial paraffin wax embedded in a plain annulus are presented in Chapter-Four. For the horizontal concentric plain annulus it is found that the mushy region, which is bounded by the liquidus (59.9^0C) and solidus (51.2^0C) isotherms, is almost horizontal in shape and occupies a region close to the inner cylinder starting from about $\theta \sim 80^0$ for all three different dimensional time spans, t = 41 min, 62 min, and 83 min. The shape and position of the mushy zone remains almost stagnant after the threshold dimensional melting time of 41 min. In the concentric plain annulus case, it is noticed that the increase of Rayleigh number which indicates the enhancement of the strength of buoyancy-driven convection, the angular position of the mushy region did not shift in the gravitational direction. This means that with the increase in melting time, the melt in the upper core of the plain annulus approaches the inner cylinder wall temperature more quickly due to the development of the conduction dominated zone at the bottom of the annulus (about $\theta \sim 0^0$ to 80^0). For this reason, the double-pipe heat exchanger forming a horizontal plain annulus is an inefficient heat storage device.

To resolve this inefficient heat transfer problem, the present study has specifically focused on a possible enhancement of the energy storage by convection at the bottom part of the annulus. It is well-known that heat transfer in a horizontal annulus is limited by the heated inner cylinder when the outer cylinder is insulated. Hence, fins can be attached to the outer surface of the inner cylinder to increase the heat transfer area. A number of experimental and numerical studies exist in the literature concerning singe-phase natural convection heat transfer in a finned annulus of various configurations of the fins. In this study, in order to alleviate the effect of dominant conduction mode of heat transfer in the lower part of the annulus, three longitudinal divergent radial fins with round tips are attached on the inner cylinder wall at the conduction dominated zone of the annulus. These fins are placed at the symmetry plane ($\theta = 0^0$), at $\theta = 30^0$, and at $\theta = 330^0$ at the bottom part of the annulus. Unfortunately, with regard to the numerical modeling of natural convection melting of a commercial PCM, no study seems to exist concerning a finned annulus. The reason for this is probably due to the complexity that arises in the numerical solution procedure for placing solid fins of high thermal conductivity in the solid or liquid PCM of low conductivity undergoing a convective-conductive meting process.

In the present study concerning finned annuli, all the relevant process parameters are kept identical as presented in Chapter-Four. Computational cases which are given in Table-4.1 and studied for plain annulus, are also studied for the finned annuli. In this chapter two cases, where the fin height inside the annulus is arbitrarily set to 30% and 50% of the fixed annulus gap, are simulated. For the convenience of discussion, the fin height of 30% of the annulus gap will be referred to as the short-finned annulus and the fin height of 50 % of the annulus gap will be referred to as the long-finned annulus.

Simulations were carried out for three Rayleigh numbers and for two values of the initial sub-cooling parameter for each of the two fin heights. This was done in order to isolate the effect of the fin height on the computed results. For the short-finned geometry, the effect of the governing parameter, such as Ra with $Ste_i = 0.113$ are discussed as cases (a), (b), and (c). For the long-finned geometry, the effect of the governing parameter, such as Ra with $Ste_i = 0.113$ are discussed as a whole. In both the cases, the predicted results are presented pictorially and quantitatively. Next, a comparison of the melting characteristics is made for the initial sub-cooling and saturated conditions of the PCM for both plain and short-finned annuli. Finally, a comparison is made between the short-finned and plain annuli for $Ste_i = 0.113$ to assess the role of fins on the melting process. To improve the melting rates, aluminum is chosen for its high thermal conductivity as the fin material for both short and long solid fins. The physical properties and dimensions of the solid aluminum fins are given in Table 5.1 below:

Table-5.1: Physical properties and thickness of the solid aluminum fin

Properties	Value
Thermal conductivity (solid) (k)	0.1799 kW / (m-K)

Density (solid) (ρ)	2712.6 kg/m^3
Specific heat (solid) (C_P)	0.96 kJ/(kg-K)
Width of the radial divergent solid fins	
Thickness (at base)	1.05 mm
Thickness (at tip)-for long-fin	1.885 mm
Thickness (at tip)-for short-fin	1.131 mm

5.2 Short-finned Annulus

When the fin height is considered as 30 % of the annulus gap (H=0.3L), this geometry is referred to as a short-finned annulus. For three cases, namely cases (a), (b), and (c), the instantaneous velocity vectors and temperature fields are shown pictorially for three non-dimensional times, τ = 0.2, 0.3, and 0.4. The total cumulative stored energy, the total melt volume fraction, and the thermal energy efficiency are also depicted quantitatively as a function of dimensional time.

5.2.1. Flow structure and melt shape in the short-finned annulus for different Rayleigh numbers

Instantaneous velocity fields in the liquid and mushy regions and the temperature distributions in both liquid and solid regions in short-finned annulus during the melting process are given in Figs. 5.1(a-c) for $\Delta T = 18.7^0C$; in Figs. 5.2(a-c) for $\Delta T = 23.7^0C$; and in Figs. 5.3(a-c) for $\Delta T = 28.7^0C$. Three instantaneous plots are provided for each case at dimensionless time (τ) = 0.2, 0.3 and 0.4 which correspond to the dimensional time of 41 min, 62 min, and 83 min, respectively. The velocity patterns are shown on the left half of each circular cross-section whereas the temperature contours are presented on the right half with a vertical line passing through $\theta = 0^0$ and $\theta = 180^0$ separating the two fields. The simulations are carried out for the Ste_i = 0.113.

5.2.1.1. Case (a) (Ra = 1.09×10^6, which corresponds to the inner cylinder wall temperature of 69.9^0C)

Velocity field

Initially, commercial paraffin wax melts near the inner cylinder due to conduction heat transfer but as the melt layer starts to grow the convection heat transfer gradually takes over. Starting from the bottom fin placed at the symmetry axis ($\theta = 0^0$), the melt gains heat and moves along the wall of the inner cylinder until it reaches the second fin at $\theta = 30^0$. At this point, the melt is forced to bend and flows downward along the second fin. Figures 5.1a to 5.1c show that the melt in between the fins are trapped and is unable to follow the contour of the surface. This is due mainly to the blockage effect by the fins in the short-finned annulus. The lower surface of the second fin transfers heat only by conduction, preventing melt movement from the bay. The upper surface of the second fin enhanced the melt flow by convection and this can be clearly seen by focusing the attention on the vector plots in Figs. 5.1(a-c) adjacent to the inner cylinder wall. Because of the high thermal conductivity of aluminum, the two fins quickly attain the inner cylinder wall temperature. Due to the temperature difference, heat exchange takes place between the fins and melt and solid PCM by conduction and convection in between the fins and around the fins. The continuous heating of the downward moving melt faces an upward force as can be seen near the tip of the second fin in Figures 5.1(a-c), causing deceleration of the downward motion. As the melt approaches near the top of the inner cylinder the flow starts to bend and move downward along the outer cylinder. As a result, with the increase in melting time a recirculation cell starts expanding sideways as well as downwards. Figures 5.1a to 5.1c show the history of the resultant maximum velocity in the melt. At the melting time of 41 min, the maximum resultant velocity is 0.00133 m/sec, whereas with the increase in melting time (t=83 min), the resultant maximum velocity decreases to 0.00051 m/sec. This is due to the fact that, for a fixed inner cylinder wall temperature, with the progress of the melting time, the melt temperature inside the annulus increases, as a consequence the buoyancy force decreases, thereby causing the magnitude of the velocity vector to decrease.

Temperature field

Figures 5.1a to 5.1c display the transient progression of the isotherms for various time instants. The beneficial effect of the fins in the concentric annulus can be seen by comparing among the Figures 5.1(a), 5.1 (b), and 5.1 (c). It is evident from these figures that for finned annulus the mushy region propagates with time and gets thicker at the bottom part of the annulus. The thick mushy region ultimately settles at the lower portion of the annulus. The reason for this behavior is due to the greater convection currents in the melt at the bottom annulus zone created by the fins. The distorted melting front around the fin tip is also observed. The progress of isotherms in between the fins can be seen to have taken parabolic shape, indicating the blockage effect created due to the fins. The local heat transfer rate is high in the blockage region. Below the middle part of the annulus, a closely packed isotherms are found at a longer melting time (t=83 min) which results in a high heat transfer rate in this region.

5.2.1.2. Case (b) (Ra = 1.38×10^6, which corresponds to the inner cylinder wall temperature of 74.9^0C)

Velocity and temperature fields for $\Delta T = 23.7^0$C and initial Stefan number, $Ste_i = 0.113$ representing case (b) (inner cylinder wall temperature of 74.9^0C) are given in Figs. 5.2(a-c) for three dimensionless time instants (τ = 0.2, 0.3, and 0.4).

Velocity field

Due to the fact that Ra is relatively high in this case compared to case (a), t the buoyancy-driven convection manifests a bit earlier and is stronger in comparison to the previous case. In this case, fluid flow is strong and a single recirculation cell develops in the melt which is spreading more inside the annulus with time. The magnitude of the maximum resultant velocity vector inside the annulus increases compared to case (a) but decreases with the increase of melting time from t= 41 min to t = 83 min, presented in Figs. 5.2 (a-c).

Temperature field

The movement of the mushy region represents the progression of melting inside the annulus. Here, additional heat is transferred from the inner cylinder wall compared to case (a) and leads the mushy region to march on in the gravitational direction. These results also indicate the difference between the low and high Ra. The blockage effect of the fins is evident here too.

5.2.1.3. Case (c) (Ra = 1.67x10^6, which corresponds to the inner cylinder wall temperature of 79.9^{0}C)

Velocity and temperature fields for ΔT = 28.7^{0}C and initial Stefan number, Ste_i = 0.113 representing case (c) (inner cylinder wall temperature of 79.9^{0}C) are given in Figs. 5.3(a-c) for three dimensionless time instants (τ = 0.2, 0.3, and 0.4).

Velocity field

Compared to the previous two cases as Ra increases further, the convective motion of the melt is intensifying as is evidenced by the velocity vectors inside the annulus, depicted in Figs. 5.3(a-c). The magnitude of the maximum velocity is also enhanced compared to the previous two cases. The high temperature difference $\Delta T = (T_{wall} - T_{Solidus})$ inside the annulus causing the unicellular melt recirculation zone to expand sideways as well as downwards.

Temperature field

When Ra increases, the more closely packed isotherms found inside the annulus and shown in Figs. 5.3(a-c), indicate that the local heat transfer rate is enhanced in this region. These densely packed isotherms also move toward the lower part of the annulus with the increase of melting time. The position of the mushy region is shifted more downward compared to cases (a) and (b), due to the increased convection. The blockage effect of the fin at $\theta = 30^0$ is also prominent here.

5.2.2. Total stored energy, total liquid fraction and energy efficiency in short-finned annulus for different Rayleigh numbers

Transient evolutions of the total stored energy, the total liquid volume fraction and the thermal energy storage efficiency for cases (a), (b) and (c) for the short-finned annulus are given in Figs. 5.4(a, b) – 5.6(a, b) for different Rayleigh numbers. The numerical values of Rayleigh number and of the total melting time are summarized in columns 3 and 5, respectively of Table 4.1 in Chapter-Four. In order to gain a better understanding of the role of the fins during the melting process, the process parameters such as the Prandtl number, radius ratio and the initial Stefan number were all kept the same as the plain annulus studied earlier. The trend's of the curves of the total stored energy, the total liquid fraction and the energy storage efficiency as a function of dimensional time are similar in nature to those seen in the plain annulus case. Comparisons of the three cases [Ra = $1.09x10^6$**,** Figs. 5.4(a,b); Ra =$1.38x10^6$, 5.5(a,b); Ra = $1.67x10^6$, 5.6(a,b)] indicate significant variations in each of the above quantities are achieved for a fixed time span. There is a threshold time for the three cases. This time is about 41 min and is identical to the plain annulus situation. After this threshold time, the curves show very slow rate of increase with time, which in comparison to the plain annulus shows a bit more upward trend. After an elapsed time of 62 min, the total stored energy is 537 kJ for case (a) (Ra = $1.09x10^6$), which in comparison to the melting time of 83 min, is only 5 % less. Whereas, at threshold time of 41 min, the total stored energy is 490 kJ for this case, which in comparison to the lower melting time of 20 min, is 36 % higher and in comparison to the higher melting time of 62 min, is only 9% less. In other words, after the elapsed melting time of 41 min, the total energy stored is only 9% and 5% higher for the subsequent two additional incremental time span of 21 min. The total stored energy is 490 kJ at a melting time of 41 min for case (a) [Ra = $1.09x10^6$], which in comparison to the plain annulus is 16 % higher.

Table-5.2 shows the effect of Ra in terms of quantitative analysis of the total stored energy (kJ), the total melt volume fraction and the thermal efficiency for initial sub-cooling, Ste_i = 0.113. From this table it is evident that in the three cases where the inner cylinder wall temperatures are arbitrarily set at 69.9^0C, 74.9^0C, 79.9^0C, all of the above mentioned quantities are enhanced considerably for the higher values of Ra in comparison to the base case with Ra = 1.09×10^6.

Table-5.2: Total stored energy, total liquid fraction and energy efficiency at time t=41 min for short-finned annulus at various Rayleigh numbers.

Quantity	Ra = 1.09×10^6 case (a)	Ra =1.38×10^6	Ra = 1.67×10^6
Total stored energy (kJ)	490	10 % higher than case (a)	19% higher than case (a)
Total liquid fraction (%)	78	5 % higher than case (a)	9% higher than case (a)
Energy fraction (%)	74	5 % higher than case (a)	8% higher than case (a)

The overall findings for the short-finned geometry are summarized in Table 5.3.

Table-5.3: Overall findings and remarks on the numerically predicted results for the short-finned annulus for 10^0C initial sub-cooling of the PCM.

Geometry	**Governing parameters**	**Effect of melting time**	**Effect of inner cylinder wall temperature**	**Remarks**
Short-finned annulus	The inner cylinder wall temperature are assigned to 69.9^0C, 74.9^0C, and 79.9^0C	With the increase in time, the increase in melting rate depends on the temperature difference (T_{Wall}-$T_{Solidus}$).	Increasing the inner wall temperature increases the melting rate.	As melting progressed, up to the threshold time of about 41 min during which convection is the predominant mode of heat transfer. Beyond that time, the conduction mode of heat transfer progressively takes over convection and the thickness of the mushy region moves downward very slowly along the lower part of the annulus.

5.3 Long-finned Annulus

When the fin height is considered as 50 % of the annulus gap (H=0.5L), this fin arrangement is referred to as long-finned annulus. The instantaneous velocity and temperature fields are shown pictorially in Figs.5.7(a-c)-5.9(a-c) at three non-dimensional times, τ = 0.2, 0.3, and 0.4 for three Rayleigh numbers ranging from 1.09x10^6 to 1.67x10^6 all for an initial sub-cooling parameter, Ste_i = 0.113. The velocity patterns are shown on the left-half of each circular cross-section whereas the temperature contours are presented on the right-half with the vertical line passing through $\theta = 0^0$ and $\theta = 180^0$ separating the two fields.

5.3.1. Flow structure and melt shape in the long-finned annulus for different Rayleigh numbers

In this part, the analysis is based on the velocity and temperature fields that are presented to clarify the flow and heat transfer characteristics inside the domain during the melting process for different operating conditions. Figures 5.7(a-c), 5.8(a-c), and 5.9(a-c) depict the computed results at dimensional time, t = 41, 62, and 83 minutes for Ra = 1.09x10^6, 1.38x10^6, and 1.67x10^6, respectively. In general, the increase in the fin surface area which is employed to transfer the heat into the domain is supplying increased heat, as a consequence the melting rate as well as the melt flow is enhanced. Here, the convection flow is accelerated by the increase of fin height which can clearly be seen from the increase in length of the velocity vectors prevailing near the upper surface of the second fin. The long fins with identical conditions and process parameters as the short-finned annulus bring almost similar flow and melting patterns. The magnitude of the maximum resultant velocity is enhanced compared to the short-finned geometry due to the increased in fin length and also due the increase of Rayleigh number. Figures 5.7(a-c) show that for an increase in melting time from τ = 0.2, to τ = 0.4, the melting front shifted downward, which can be observed by following the 64.4^{0}C isotherm. The melting front is changed from being the classical pear-shaped to the more horizontally-uniformed profile at the middle of the annulus. The profile takes this horizontal shape if only a conduction mode of heat transfer is considered. With the increase of melting time and with the increase of Ra for the long-finned annulus, the mushy region presented by the blue color has changed the position considerably in the gravitational direction (downward), which is a very desirable characteristic for this process. All of the temperature distribution figures show that the accelerated heat which is imposed at the inner cylinder wall pushes the mushy region more downward than does the short-finned annulus, which can be seen by comparing the Figures 5.7(a-c)-5.9(a-c) , for long-finned annulus with those of the corresponding Figs.5.1(a-c)-5.3(a-c) for short-finned annulus.

5.3.2 Transient evolution of total stored energy for different Rayleigh numbers for the long-finned annulus

The quantitative values of the total stored energy in kJ for Ra = 1.09×10^6, 1.38×10^6, and 1.67×10^6, for the case of a long-finned geometry are given in Fig. 5.10 in the form of a bar chart for four non-dimensional times, τ = 0.1, 0.2, 0.3, and 0.4. In order to gain a better understanding of the role played by the fins during the melting process, the process parameters such as the Prandtl number, the radius ratio and the initial Stefan number are all kept same as the plain annulus. A comparison of the three Rayleigh numbers (Ra = 1.09×10^6**,** 1.38×10^6, and 1.67×10^6) indicates that the total energy storage increases with the increase of buoyancy effect at each time span. The total stored energy is 496 kJ for the melting time of 41 min for Ra = 1.09×10^6, which in comparison to the plain annulus, is 17 % higher. Table-5.4 shows the effect of Rayleigh number in terms of the total stored energy for initial Stefan number, Ste = 0.113. Results in Table-5.4 show that for the three cases where the inner cylinder wall temperature is arbitrarily set to either 69.9^0C or 74.9^0C or 79.9^0C, the total energy storage capability of the PCM filled annulus space is enhanced remarkably at dimensional time span of 41 min with respect to the base case of Ra = 1.09×10^6.

Table-5.4: Total stored energy in kJ at instantaneous time t = 41 min for long-finned annulus at various Rayleigh numbers.

Quantity	Ra = 1.09×10^6	Ra =1.38×10^6	Ra = 1.67×10^6
Total stored energy (kJ)	496	17 % higher than Ra = 1.09×10^6	26% higher than Ra = 1.09×10^6

5.4. Comparison between short-finned and long-finned geometry (in terms of total stored energy at Rayleigh number, Ra = 1.09×10^6 and initial Stefan number, $Ste_i = 0.113$)

In order to get a clear understanding of the role played by the fin height inside an annulus during the melting process, two cases are run with two different fin heights, and the process parameters for these cases are listed in Table 4.1 of Chapter-Four. The other basic parameters such as the Prandtl number, the radius ratio and the initial sub-cooling parameter are all kept constant as mentioned in the plain annulus study. Figure 5.11 shows the transient evolution of the total stored energy through a bar chart for both short-finned and long-finned geometries for a $\Delta T = 18.7^0$C. The results presented in the Table-5.5 can explain the transient phenomenon more clearly which is shown in graph 5.11. From Table-5.5 it is seen that an increase in fin height causes a substantial amount of increase in total stored energies for the melting time span, t = 20 and 83 minutes. In time, t = 41 and 62 minutes the rate of increments are insignificant compared to the melting time of 20 min and 83 min. This may be due to the blockage effect on the melt flow created by the fin. Similar to earlier geometries, one can see from Table 5.5 that the threshold time is also approximately 41 min for the long-finned geometry.

In the long-finned annulus, after a melting time of 62 min, the total stored energy is 540 kJ for Ra = 1.09×10^6, which in comparison to the melting time of 83 min, is only 10 % less. Whereas, at threshold time, t = 41 min, the total stored energy is 496 kJ for Ra = 1.09×10^6, which in comparison to the lower melting time of 20 min, is 30 % higher and in comparison to higher melting time at t = 62 min, is only 8% less for same time difference of 21 min. So, in the case of long-finned geometry, after an elapsed melting time of t = 41 min, the total stored energies are 10% and 8% higher for the subsequent two incremental melting time difference of 21 minutes.

The influence of fin height on the melting flow and front patterns for Ra = 1.09×10^6 are presented in Figs. 5.1(a-c) for short-finned annulus and in Figs. 5.7(a-c) for long-finned annulus. An inspection of the temperature isotherms clearly indicates the effect of blockage in between the fins. Before the threshold time, the development of natural convection in the melt for the short-finned annulus appears to be substantially more than long-finned annulus due to the smaller blockage created by the short fins. In short-finned annulus for a time span of 21 min (from 20 min to 41 min) the total heat stored is 130 kJ, whereas in the long-finned annulus for the same time span the total stored energy is 116 kJ, which is 12 % higher in comparison to the long-finned annulus. In short-finned geometry, 6.8 % more and 44% less total energies are stored in between the melting time of 41 and 62 min and in between the melting time of and 62 and 83 min, respectively compared to the long-finned annulus. The opposite phenomena occur in the case of storing of energies in short-finned annulus up to the time difference between 20 and 63 minutes. As melting proceeds in the short-finned geometry, with the increase in time due to the smaller fin height, the melt at the bottom of the annulus can mix with the melt in the upper part of the annulus without any flow resistance offered by the fin height, as a consequence the heat transfer rate is increased between these initial time differences. These phenomena have changed with the time difference in between 62 and 83 min, as it is observed that the total stored energy is 44 % higher in long-finned annulus than short-finned annulus due to well mixing of the melt between the bottom and top parts of the annulus in long-finned geometry at the higher melting time (t = 83 min).

Therefore, in terms of energy storage, the long-finned annulus is always more profitable for the melting process than the short-finned annulus. When fin cost is of a concern, the short-finned is more advantageous than long-finned during the initial stages of melting. If melting takes place for a longer time, the long-finned geometry should be more desirable than the short-finned geometry.

Table-5.5: Total stored energy in kJ for short-finned and long-finned annuli for Rayleigh number, Ra = 1.09×10^6 at four melting time spans.

Geometry	t = 20 min	t = 41 min	t = 62 min	t = 83 min
Total stored energy in short-finned annulus (kJ)	360	490	537	566
Total stored energy in long-finned annulus (kJ)	380	496	540	592
Percentage enhancement with respect to short-finned annulus	5.5	1.2	0.6	4.6

5.5. Effect of initial sub-cooling parameter at Ra = 1.09×10^6

From a more practical point of view, it is also interesting to determine the influence of the degree of initial sub-cooling of the PCM during the melting process. For this purpose, two cases for plain and finned annuli comparable to case (a) in subsection 4.2.1 for plain annulus and case (a) of subsection 5.2.1.1 for short-finned annulus are simulated and the process parameters for these cases are listed in the first row of Table 4.1. In order to observe the initial sub-cooling parameter effect, the Prandlt number, the radius ratio, the Rayleigh number and the Stefan number are all kept constant for both annuli. The Ste_i is only changed, assigned a value of 0 (no sub-cooling) and 0.113 (10^0C sub-cooling). Figures 5.12(a-c) and Figs. 5.13(a-c) illustrate the melt flow patterns and temperature distributions for plain and short-finned annuli for $Ste_i = 0$, for three non-dimensional times, τ = 0.2, 0.3, and 0.4 and for Ra = 1.09×10^6. The velocity patterns are shown on the left half of each circle whereas the temperature contours are presented on the right half with the vertical line passing through $\theta = 0^0$ and $\theta = 180^0$ separating the two fields. Upon examination of the results for these cases and of those of the corresponding cases presented in Figs.4.1(a-c) for plain annulus and in Figs.5.1(a-c) for short-finned annulus with $Ste_i = 0.113$, it can be concluded that the flow and thermal fields are very similar for both of these two cases. The only differences are in the radial and angular positions of the mushy region for the two cases. Although, the initial sub-cooling parameter plays a significant role in the melting process, but it's influence is much less on the melt flow patterns than the Rayleigh number. For both plain and finned annuli, a thicker mushy region formed, which is located near the lower part of the geometry, for $Ste_i = 0$ compared to the case for $Ste_i = 0.113$. In the following subsection a comparative study is made for both plain and short-finned annuli in terms of transient evolution of total stored energy (kJ):

1. Comparison between plain and short-finned annuli with an initial sub-cooling parameter, $Ste_i = 0$.
2. Comparison of two different initial sub-cooling parameter, $Ste_i = 0$, and 0.113 for plain and short-finned annuli.

5.5.1. Comparison between plain and short-finned annuli with no sub-cooling, $Ste_i = 0$

Figure 5.14 shows the total energy stored in kJ as a function of dimensional total melting time in minutes in the form of a bar chart for a plain and short-finned annuli for $Ste_i = 0$. The quantitative values of the total stored energy for both annuli are given in Table 5.6. From Fig. 5.14 and Table-5.6, it is evident that for the zero initial Stefan number, the short-finned annulus stores much more heat than plain annulus at every time instant for an inner cylinder wall temperature of 69.9^0C and the rate of the total stored energy increases with the progression of melting. The total stored energy is 593 kJ for a melting time of 83 min for short-finned annulus, which in comparison to the plain annulus is 28% higher, suggesting that a stronger overall convection effects are at play during the melting process for the short-finned annulus.

Table-5.6: Total stored energy in kJ for Ra = $1.09x10^6$ at four time spans for plain and short-finned annuli with $Ste_i = 0$.

Geometry	t = 20 min	t = 41 min	t = 62 min	t = 83 min
Total stored energy in plain annulus (kJ)	347	445	458	463
Total stored energy in short-finned annulus (kJ)	396	506	549	593
Percentage of enhancement in short-finned annulus	14	13.7	20	28

5.5.2. Effect of two different initial Stefan numbers, Ste = 0, and 0.113 for plain and finned annuli

Figures 5.15 (a) and (b) represent the time history of the total stored energy in kJ in a bar chart format for the minimum initial Stefan number $Ste_i = 0$ and for the maximum initial Stefan number $Ste_i = 0.113$ for plain and short-finned annuli. From the bar charts it is found that when the initial temperature of the PCM is assumed to be at the solidus temperature (Ste = 0), the higher is the total stored energy for both plain and finned annuli in comparison to the case with the initial temperature of the PCM 10^0C lower than the solidus temperature (Ste = 0.113).

The total stored energy for Ste_i = 0 is 13 % higher at melting time, t = 20 min; 5.5 % higher at melting time, t = 41 min; 3.6 % higher at melting time, t = 62 min; 3.8 % higher at melting time, t = 83 min; when compared to the corresponding values for Ste_i = 0.113 for the plain annulus.

The total stored energy for Ste_i = 0 is 10 % higher at melting time, t = 20 min; 3.3 % higher at melting time, t = 41 min; 2.2 % higher at melting time, t = 62 min; 4.8 % higher at melting time, t = 83 min; when compared to the corresponding cases for Ste_i = 0.113 for short-finned annulus.

From the above predicted results, it can be concluded that for Ste_i = 0 for both plain and finned annuli, the melting rate is enhanced because for this case right from the beginning the heat supplied through the inner cylinder wall and the fins has gone to melt the PCM, thereby storing more energy in the form of latent heat, With the initial sub-cooling of the PCM some sensible energy is required to achieve the solidus temperature before the solid PCM starts to melt. During this time heat is transferred through the solid PCM via the slow conduction mode of heat transfer.

5.6. A comparative study between plain and short-finned annuli with 10^0C sub-cooling temperature

The comparative studies between the plain and finned annulus have been performed in this section on the following aspects:

1. Effect of melting time for both plain and short-finned annuli.
2. Effect of Rayleigh and Stefan numbers for both plain and short-finned annuli.
3. Difference in melting characteristics between plain and short-finned annuli.

Two cases are chosen to compare the predicted results for plain and finned annuli. These cases are listed in the second and fourth rows in Table 4.1. For the initial sub-cooling parameter, Ste_i =

0.113, the Prandtl number and the radius ratio are both kept constant and are identical to the parametric values reported in Chapter-Four.

5.6.1. Effect of melting time for both plain and short-finned annuli

For comparison purposes, the temperature distributions are shown on the left-half of each circular cross-section at non-dimensional time, τ = 0.2 whereas the temperature contours are presented on the right-half at non-dimensional time, τ = 0.4 with a vertical line passing through $\theta = 0^0$ and $\theta = 180^0$ separating the two temperature fields. Figures 5.16(a) and 5.16 (b) illustrate the temperature patterns for plain and short-finned annuli for Ra = $1.09\text{x}10^6$. Figure 5.16(a) shows the 67^0C isotherm as well as the mushy region movement for the case of plain annulus at two melting times, t = 41, and 83 min. A comparison of these two cases (τ = 0.2, and 0.4) indicates that the 67^0C temperature contour moves significantly in the downward direction with the increase in melting time, and the shape and position of the mushy region practically remains the same throughout the melting progression from time 41 to 83 minutes. Figure 5.16(b) shows the 67^0C isotherm as well as the mushy region's location and thickness for the case of short-finned annulus at two melting times, t = 41, and 83 min. A comparison of these two cases (τ = 0.2, and 0.4) indicates that the 67^0C isotherm and the shape and position of the mushy region move significantly downward in the gravitational direction with the increase in melting time from 41 to 83 minutes.

Figures 5.17(a) and 5.17(b) show the total stored energy and the total liquid fraction versus melting time for plain and short-finned annuli. The total energy stored and the total melt volume fraction are 6 % and 3 % higher, respectively for the melting time of 83 min compared to the melting time of 41 min for the plain annulus geometry. Whereas, for short-finned annulus, the total stored energy is 16 % higher and the total melt volume fraction is 14 % higher for the melting time of 83 min when compared to the melting time of 41 min, as shown in Fig. 5.17 (b).

The higher the melting time, the larger is the progression of melting in both plain and short-finned annuli. For the finned annulus, the total stored energy is much greater than the plain annulus for the same time span. This enhancement occurs due to the increase in natural convection intensity with the increase in melting time for the fins.

5.6.2. Effects of Rayleigh and Stefan numbers in plain and short-finned annuli

To ascertain the effect of the Rayleigh number on the melting process, two cases are simulated, one for Ra = $1.09\text{x}10^6$, and other for Ra = $1.67\text{x}10^6$. The temperature distributions are shown on the left-half of each circle for Ra = $1.09\text{x}10^6$, whereas the temperature contours are presented on the right-half for Ra = $1.67\text{x}10^6$ with the vertical line passing through $\theta = 0^0$ and $\theta = 180^0$ separating the two temperature fields. Figures 5.18(a) and 5.18 (b) illustrate the temperature patterns for plain and short-finned annuli for a melting time of 83 min. Figure 5.18(a) shows the 67^0C isotherm as well as the mushy region represented by the blue color for the case of plain annulus for two Rayleigh numbers, Ra = $1.09\text{x}10^6$, and $1.67\text{x}10^6$. A comparison of the two cases (Ra = $1.09\text{x}10^6$, and $1.67\text{x}10^6$) indicates that the 67^0C isotherm moves significantly in the downward direction with the increase in Ra, and the shape and position of the mushy region do not change much throughout the melting progression for the increase in Ra from $1.09\text{x}10^6$ to $1.67\text{x}10^6$. Figure 5.18(b) shows the 67^0C isotherm as well as the mushy region's location and thickness for the case of short-finned annulus for the same two Rayleigh numbers as the plain annulus. A comparison of the two cases indicates that the 67^0C isotherm and the shape and position of the mushy region all changed, all have moved significantly downward in the gravitational direction with the increase in Ra.

Figures 5.19(a) and 5.19(b) show in the form of a bar chart the transient evolution of total stored energy for the plain and short-finned annuli. For a melting time of 83 min, the total stored energy is 11 % higher for Ra = $1.67\text{x}10^6$ when compared to the Ra = $1.09\text{x}10^6$ for the plain annulus geometry (Fig. 5.19 (a)). For short-finned annulus, the total stored energy is 13 % higher for Ra = $1.67\text{x}10^6$ compared to Ra = $1.09\text{x}10^6$ (Fig. 5.17 (b)) for the same melting time.

So, the higher the Rayleigh number, the larger is the melting of PCM in both plain and short-finned annuli. For the finned annulus, the total stored energy is larger than the plain annulus for the same melting time. This enhancement has occurred due to the increase in natural convection intensity with the increase in Ra and also for the fins.

5.6.3. Difference between plain and short-finned annuli in terms of temperature patterns and transient evolution of total stored energy

In order to compare the predicted results between the plain and short-finned annuli, contours of the instantaneous temperature fields and total stored energies have been selected. Here, temperature patterns are shown on the left half of each circular cross-section for plain annulus whereas the temperature contours are presented on the right half for short-finned annulus with the vertical line passing through $\theta = 0^0$ and $\theta=180^0$ separating the two temperature fields. Figures 5.20(a) and 5.20 (b) illustrate the temperature patterns at non-dimensional time, $\tau = 0.2$, and 0.4 for Rayleigh number, Ra = $1.09\text{x}10^6$. Figure 5.20(a) shows the 67^0C isotherm, as well as the position of the mushy region at the melting time of 41 min for the case of plain and short-finned annuli. A comparison of these two cases at two instantaneous melting times of 41 and 83 min, indicate that the 67^0C isotherm moves only a little-bit more in the downward direction and the mushy region shifts downward compared to the plain annulus. The mushy region expanded sideways as well as downwards and appeared in the bottom zone and consequently this has lead to cause an enhanced melting of the PCM in the bottom region for the short-finned annulus.

Figures 5.21(a) and 5.21(b) show a graphical comparison of plain and finned annuli in terms of the total energy stored and the total melt fraction for four non-dimensional times, τ = 0.1, 0.2, 0.3, and 0.4 for Ra = $1.09\text{x}10^6$ and initial Stefan number $Ste_i = 0.113$. From these bar charts it is observed that the total stored energy and the total melt volume fraction are much more higher in finned annulus than in the plain annulus at each time period This is due to the replacement of conduction regime which prevails near bottom region of the plain annulus with the convection mode of heat transfer favored by the fins.

The total stored energy for short-finned annulus is 20 % higher at melting time, t = 20 min; 16 % higher at melting time, t = 41 min; 22 % higher at melting time, t = 62 min; 27 % higher at melting time, t = 83 min; compared to the corresponding values for plain annulus.

The total liquid fraction for short-finned annulus is 15 % higher at melting time, t = 20 min; 15 % higher at melting time, t = 41 min; 20 % higher at melting time, t = 62 min; 23 % higher at melting time, t = 83 min; when compared to the corresponding values for plain annulus.

From the above quantitative findings it is clear that a finned annulus is much more advantageous than a plain annulus. The longer the fin, the better is the thermal efficiency. The fins increased the natural convection intensity at the bottom zone of the annulus, thereby leading to the enhancement of the thermal efficiency of the LHTES devices.

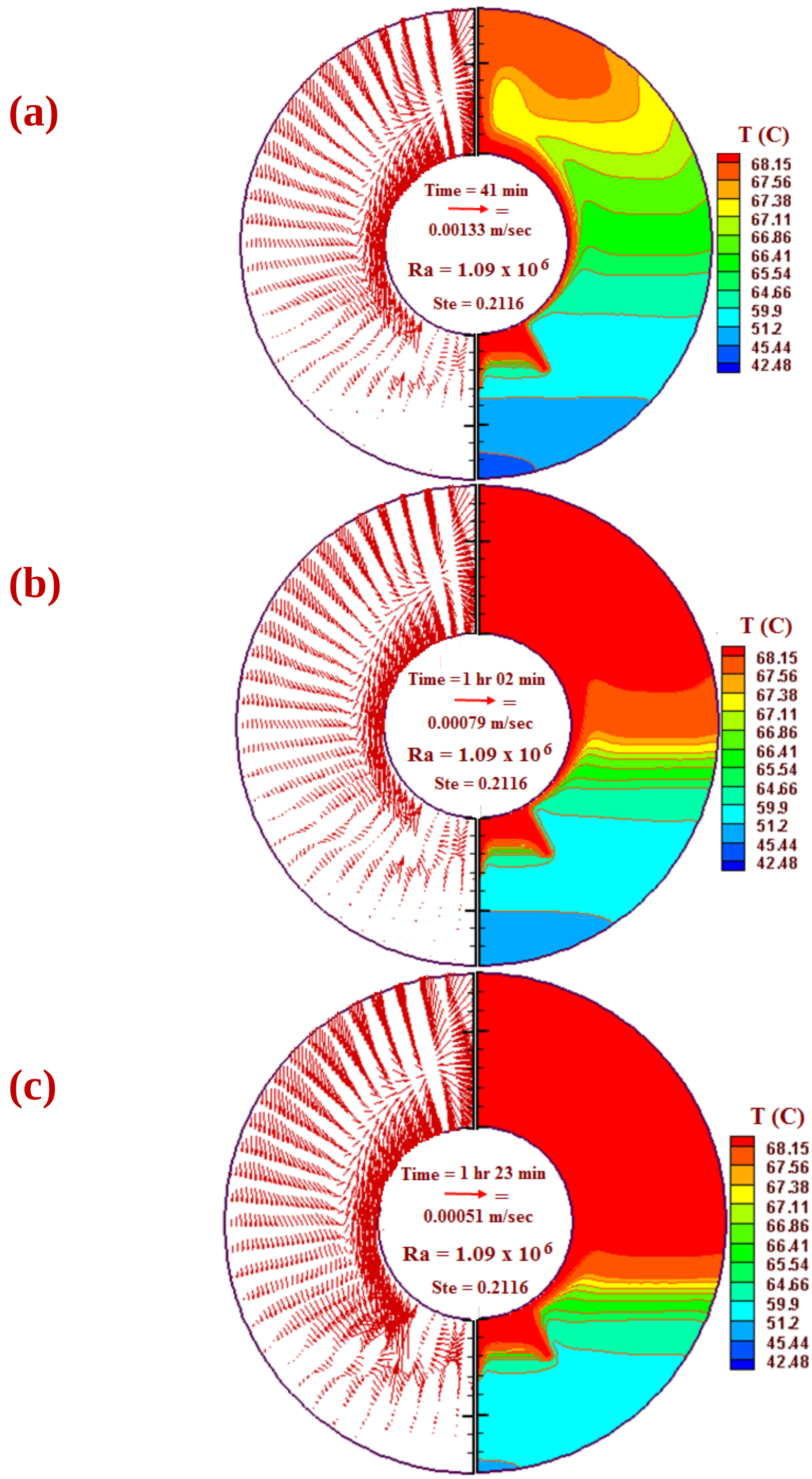

Figure 5.1: Temperature contours (right) and velocity vectors (left) for inner wall temperature of 69.9^0C for short-finned annulus: $Ste_i = 0.113$, and at time, (a) 41min; (b) 62min; (c) 83 min.

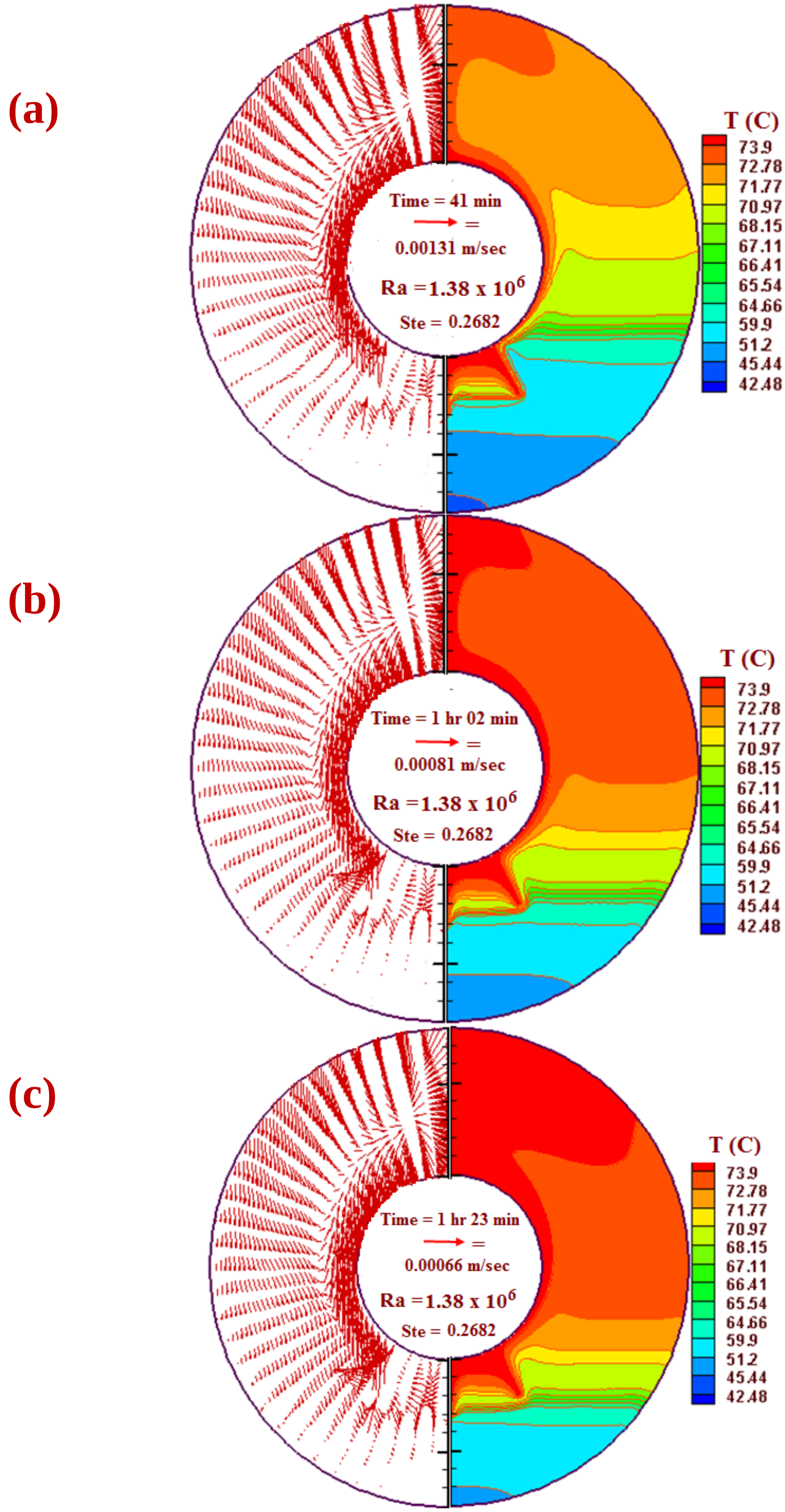

Figure 5.2: Temperature contours (right) and velocity vectors (left) for inner wall temperature of 74.9^0C for short-finned annulus: Ste_i =0.113, and at time, (a) 41min; (b) 62min; (c) 83min.

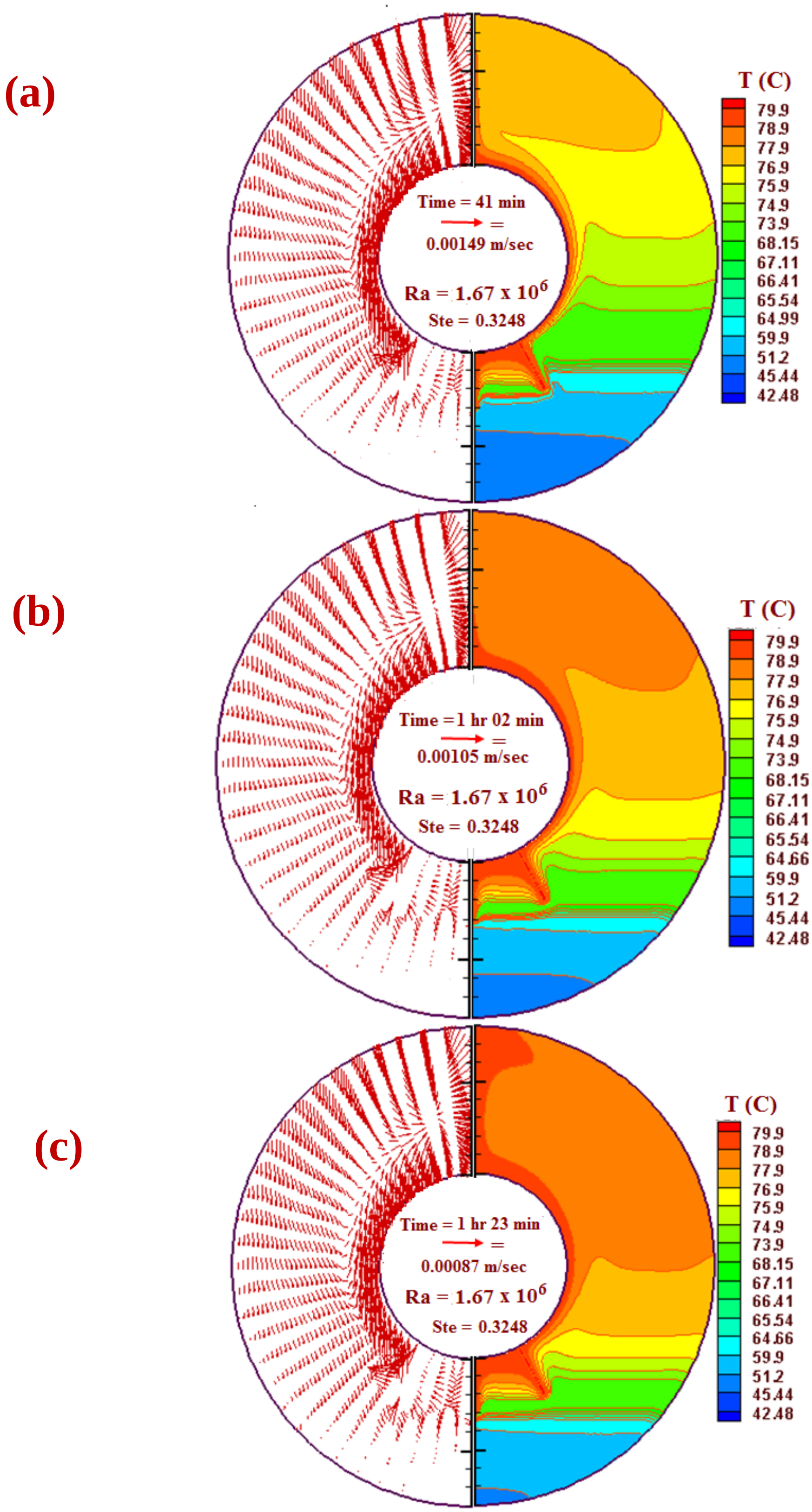

Figure 5.3: Temperature contours (right) and velocity vectors (left) for inner wall temperature of 79.9^{0}C for short-finned annulus: Ste$_i$ =0.113, and at time, (a) 41 min; (b) 62 min; (c) 83 min.

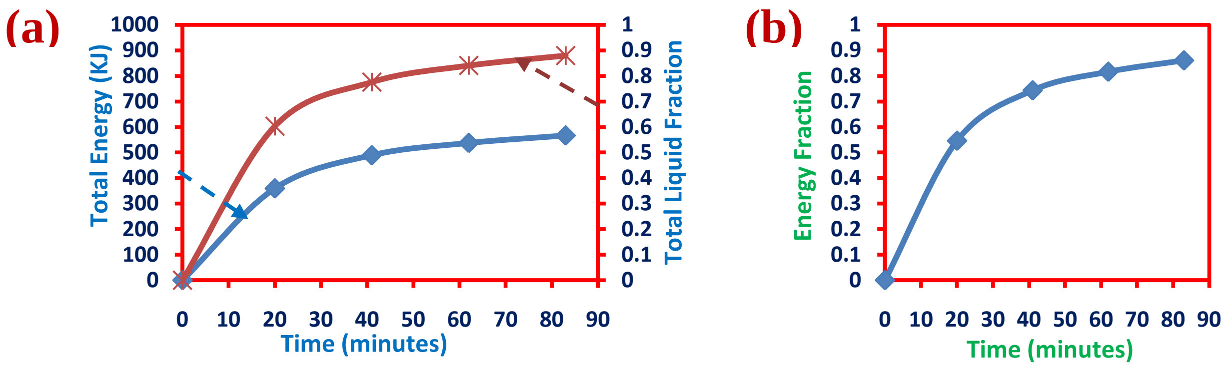

Figure 5.4: For T_{WALL}= 69.9 ^{0}C, Ste_i = 0.113 for short-finned annulus: (a) transient evolutions of total stored energy (kJ) and total liquid fraction; (b) transient evolutions of energy fraction.

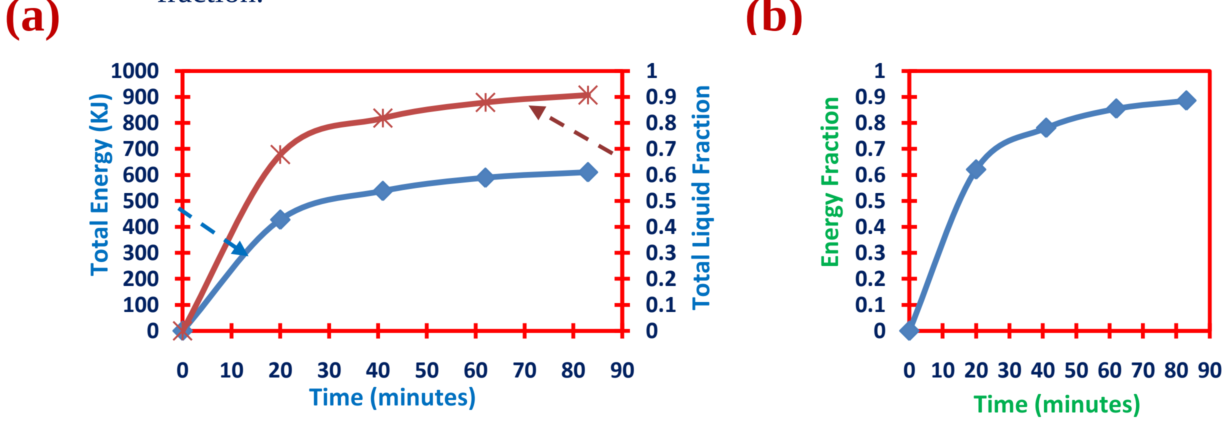

Figure 5.5: For T_{WALL}= 74.9 ^{0}C, Ste_i = 0.113 for a plain annulus: (a) transient evolutions of total stored energy (kJ) and total liquid fraction; (b) transient evolutions of energy fraction.

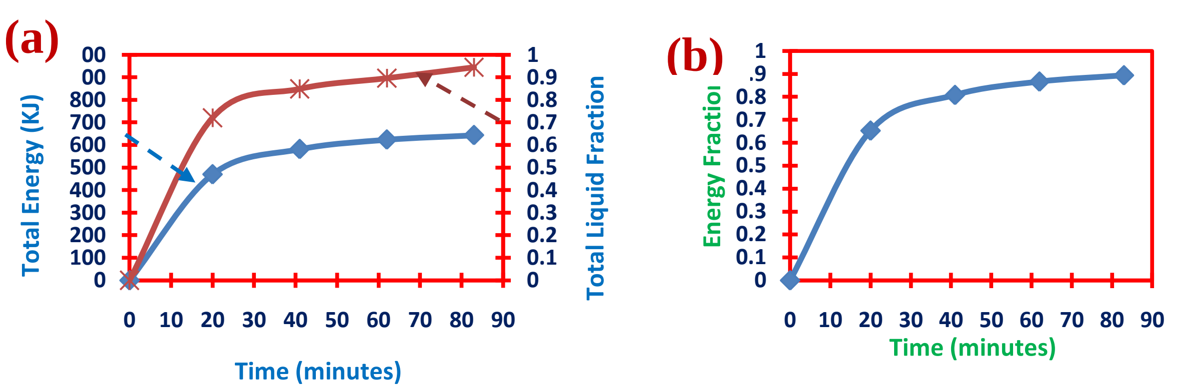

Figure 5.6: For T_{WALL}= 79.9 ^{0}C, Ste_i = 0.113 for a plain annulus: (a) transient evolutions of total stored energy (kJ) and total liquid fraction; (b) transient evolutions of energy fraction.

.

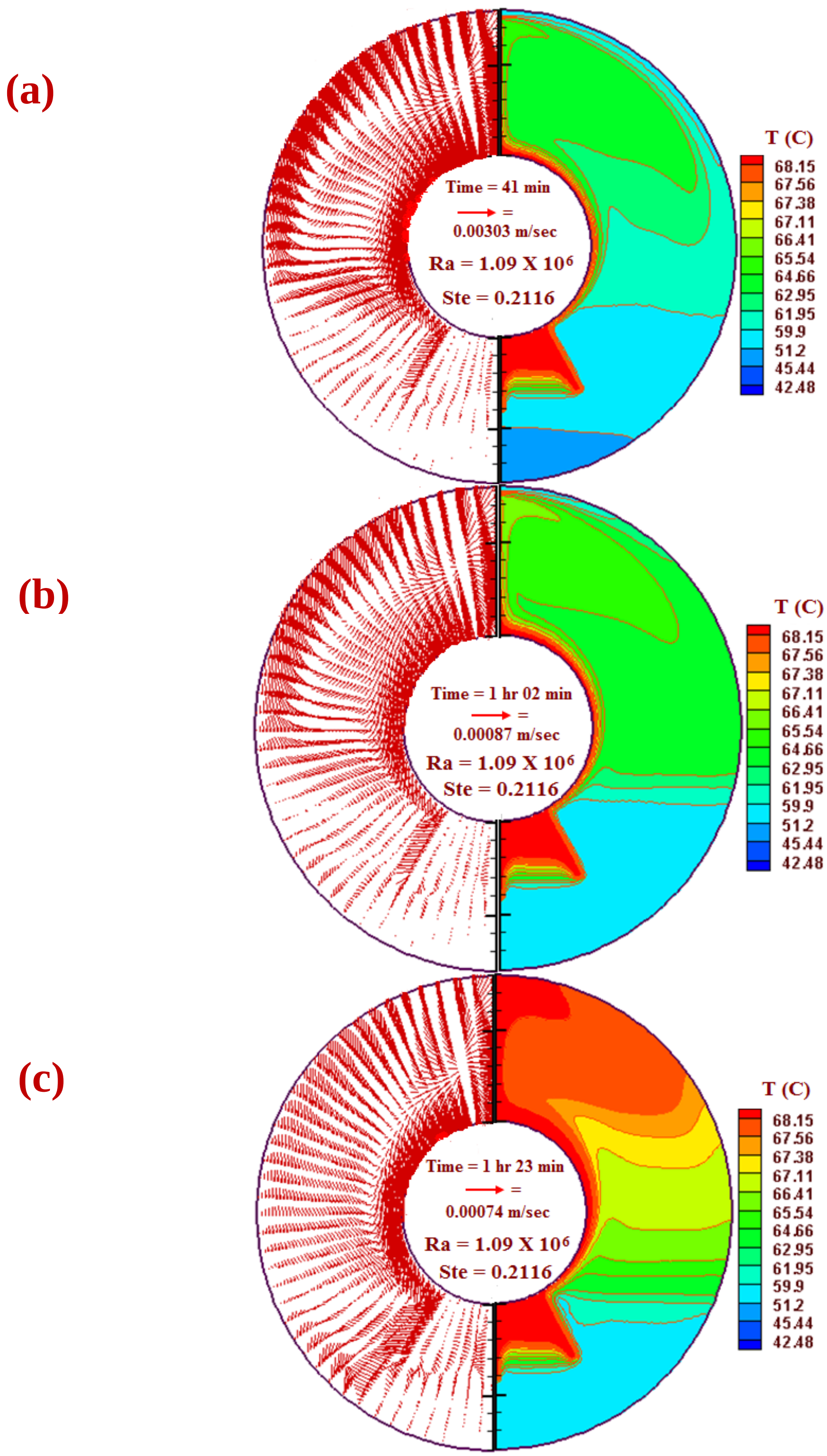

Figure 5.7: Temperature contours (right) and velocity vectors (left) for inner wall temperature of 69.9^{0}C for long-finned annulus: Ste_i =0.113, and at time, (a) 41min; (b) 62min; (c) 83 min.

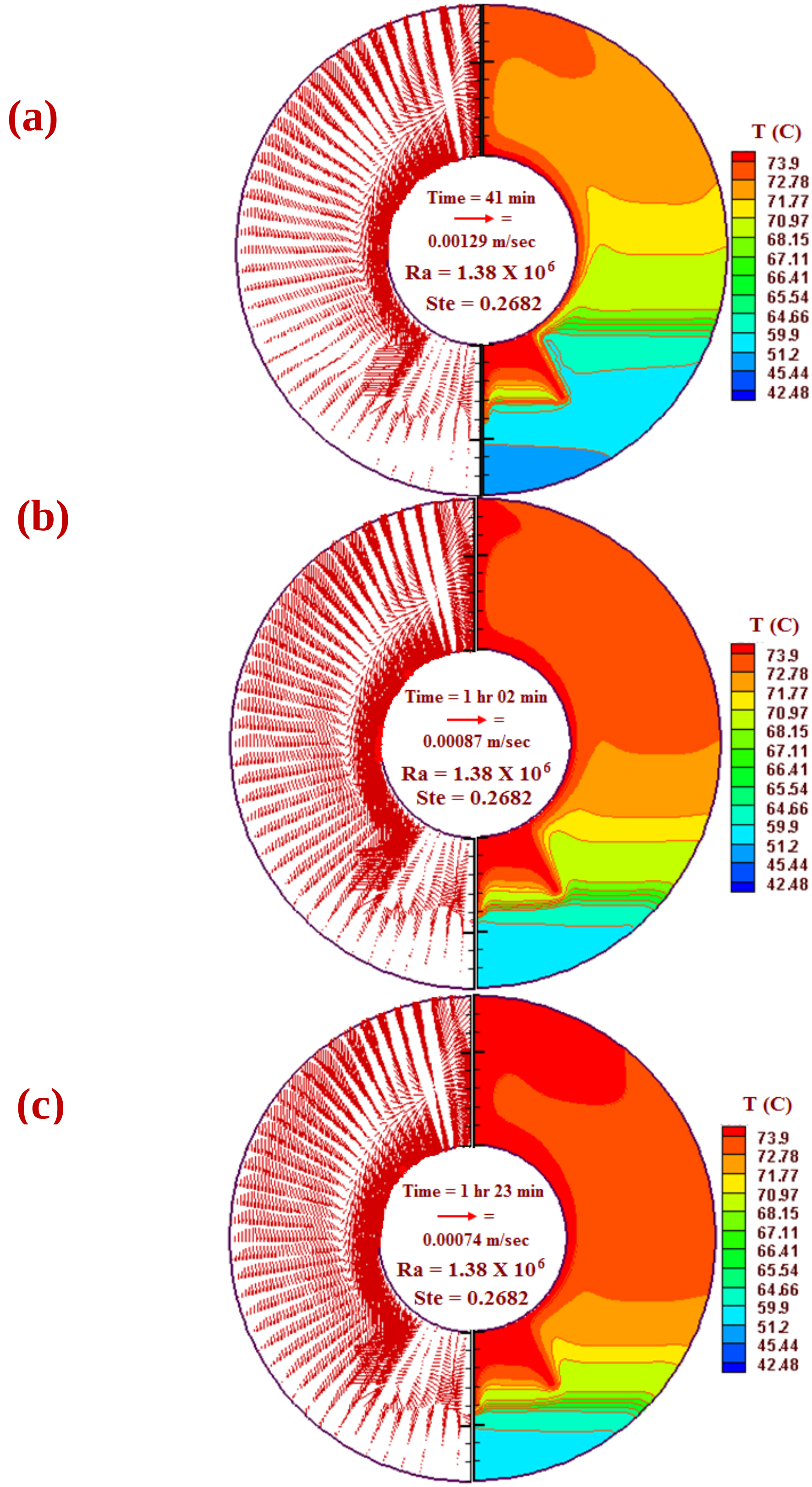

Figure 5.8: Temperature contours (right) and velocity vectors (left) for inner wall temperature of 74.9^{0}C for long-finned annulus: Ste_i =0.113, and at time, (a) 41 min; (b) 62 min; (c) 83 min.

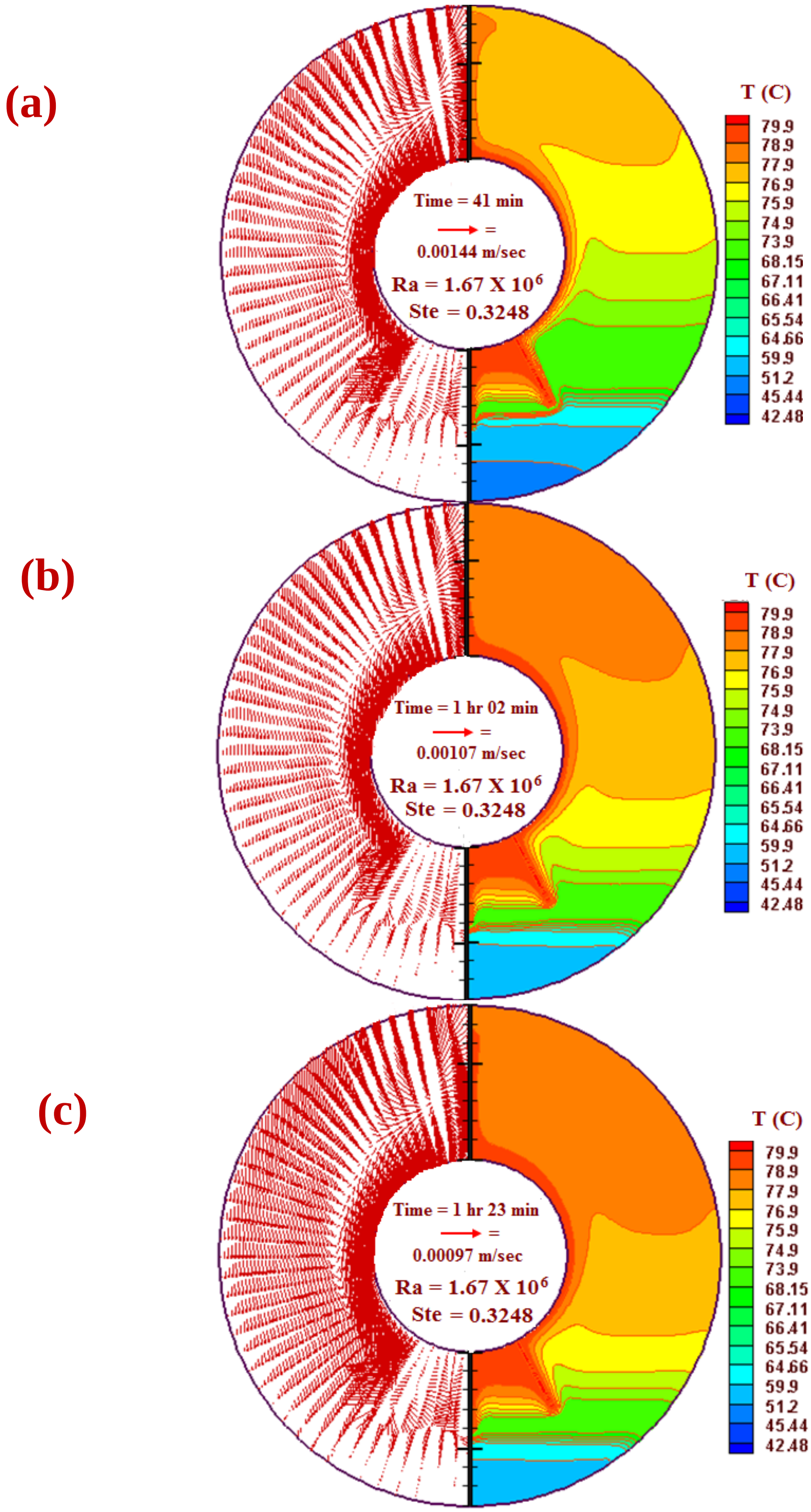

Figure 5.9: Temperature contours (right) and velocity vectors (left) for inner wall temperature of 79.9^{0}C for long-finned annulus: Ste_i = 0.113, and at time, (a) 41 min; (b) 62 min; (c) 83 min.

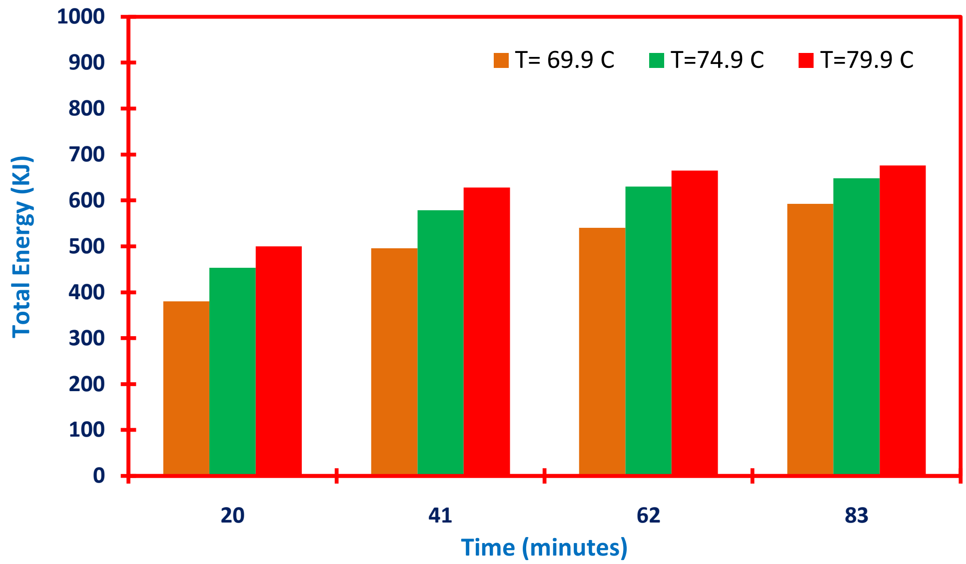

Figure 5.10: Total stored energy (kJ) at different times with $Ste_i = 0.113$ for three different inner cylinder wall temperatures, 69.9^0C, 74.9^0C , 79.9^0C for a long-finned annulus.

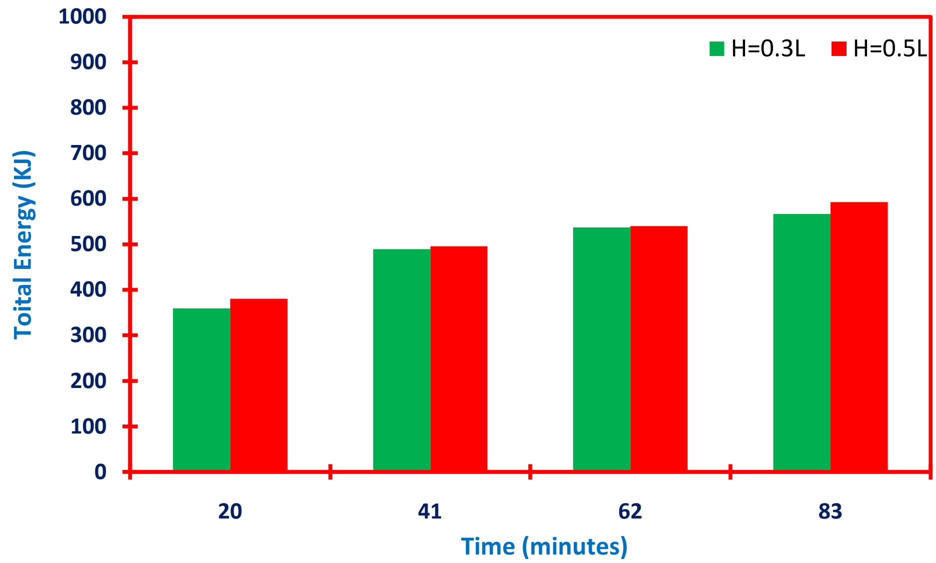

Figure 5.11: Comparison between short finned and long-finned annuli in terms of total stored energy (kJ) at different times for $T_{WALL}= 69.9^0$C and $Ste_i = 0.113$.

(a)

(b)

(c)

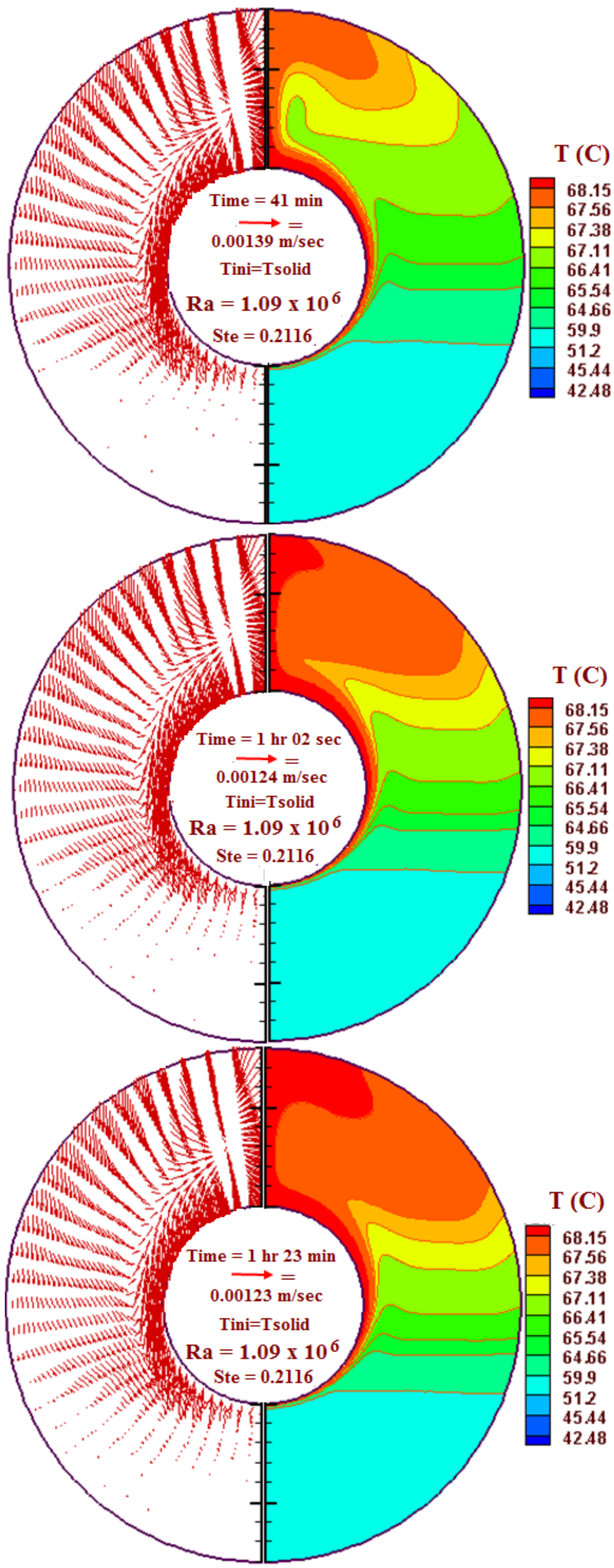

Figure 5.12: Temperature contours (right) and velocity vectors (left) for inner wall temperature of 69.9^0C for a plain annulus: $Ste_i = 0$, and at time, (a) 41 min; (b) 62 min; (c) 83 min.

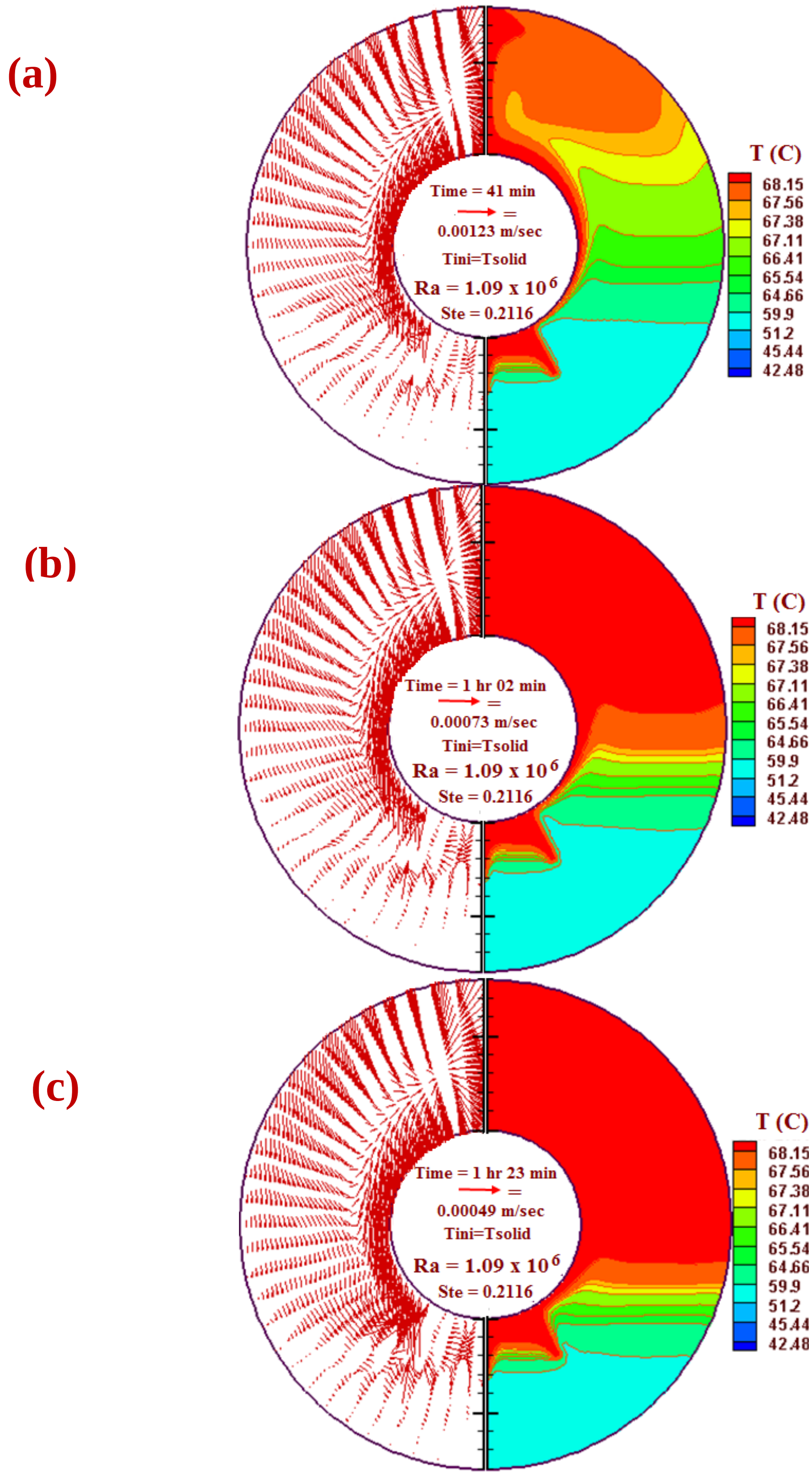

Figure 5.13: Temperature contours (right) and velocity vectors (left) for inner wall temperature of 69.9^0C for short-finned annulus: $Ste_i = 0$, and at time, (a) 41 min; (b) 62 min; (c) 83 min.

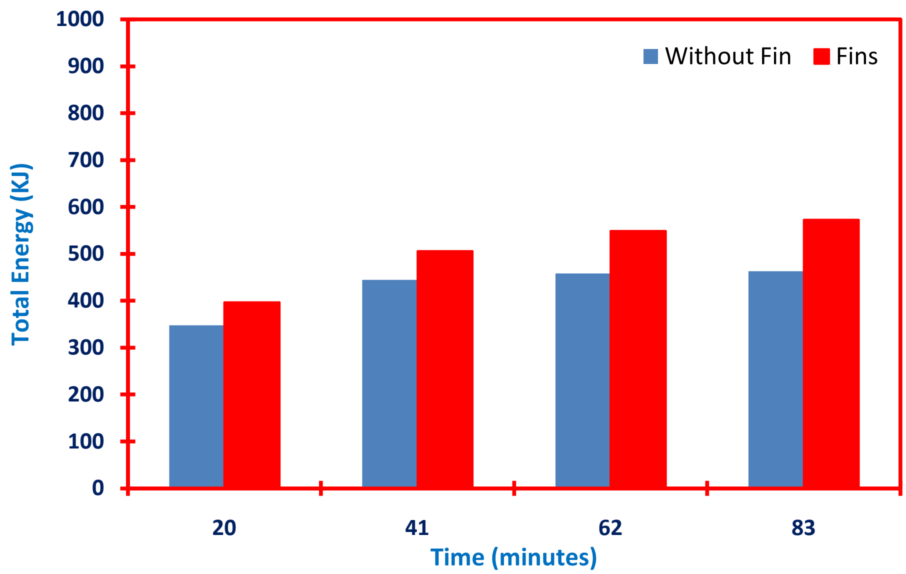

Figure 5.14 : Comparison between plain and short-finned annuli in terms of total stored energy (kJ) at different times for T_{WALL}= 69.9^{0}C and Ste_i = 0.

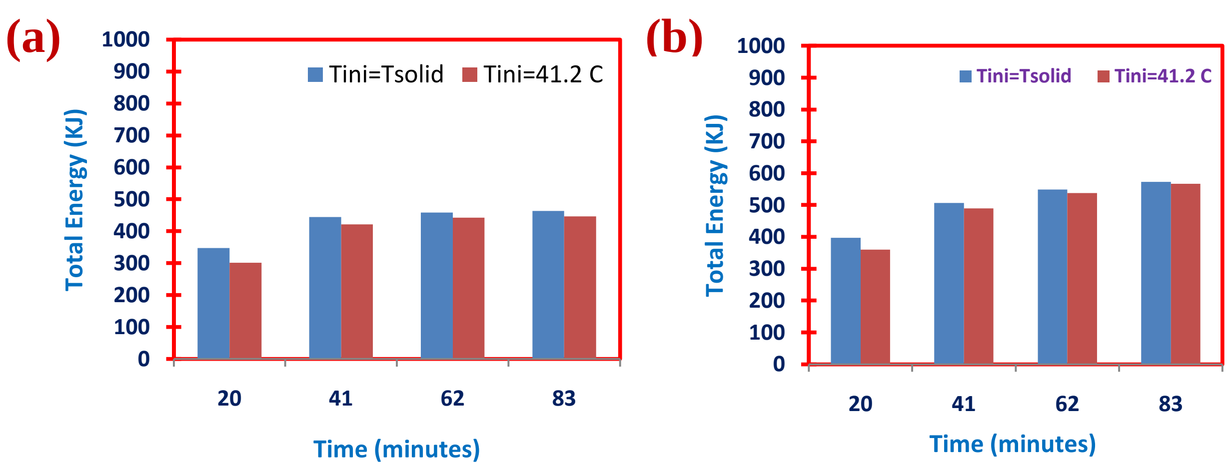

Figure 5.15: For T_{WALL} = 69.9 ^{0}C: (a) comparison between Ste_i =0 and Ste_i =0.113 in terms of transient evolution of total stored energy (kJ) for plain annulus, (b) comparison between Ste_i =0 and Ste_i = 0.113 in terms of transient evolution of total stored energy (kJ) for short-finned annulus.

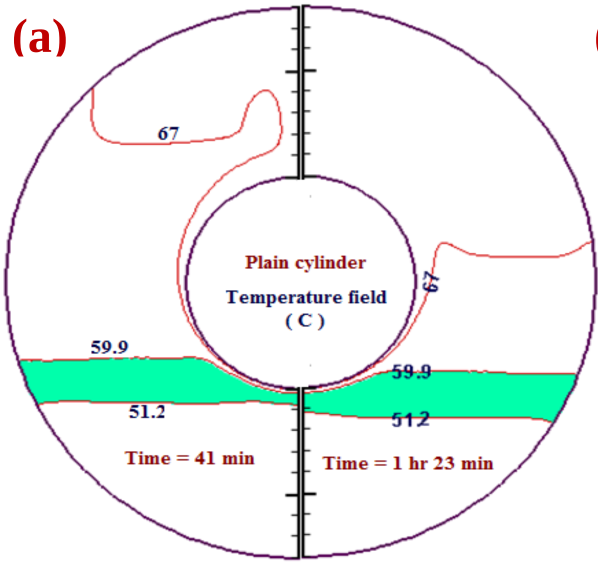

Figure 5.16: For T_{WALL} = 69.9 ^{0}C, and Ste_i = 0.113: (a) temperature contours (left) at 41 minutes and temperature contours (right) at 83 minutes for plain annulus, (b) temperature contours (left) at 41 minutes and temperature contours (right) at 83 minutes for short-finned annulus.

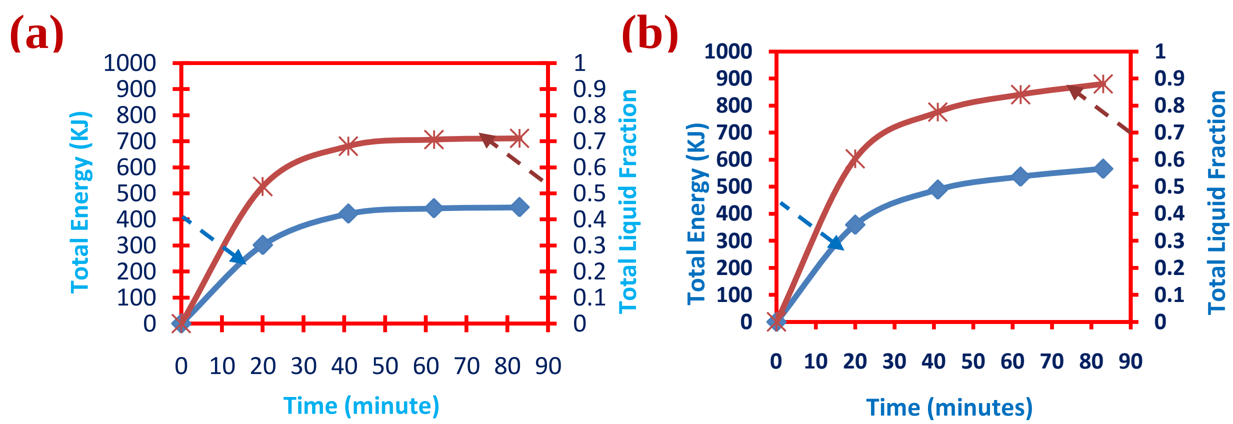

Figure 5.17: Evolution of total stored energy (kJ) and total liquid fraction at different melting times for T_{WALL} = 69.9 ^{0}C, and Ste_i = 0.113: (a) plain annulus, (b) short-finned annulus.

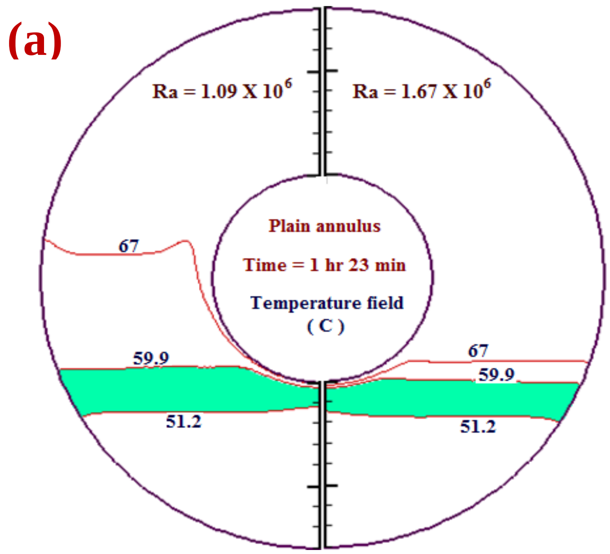

Figure 5.18: For 83 minutes of melting, and $Ste_i = 0.113$: (a) temperature contours (left) at $T_{WALL} = 69.9\ ^0C$ and temperature contours (right) at $T_{WALL} = 79.9\ ^0C$ for plain annulus, (b) temperature contours (left) at $T_{WALL} = 69.9\ ^0C$ and temperature contours (right) at $T_{WALL} = 79.9\ ^0C$ for short-finned annulus.

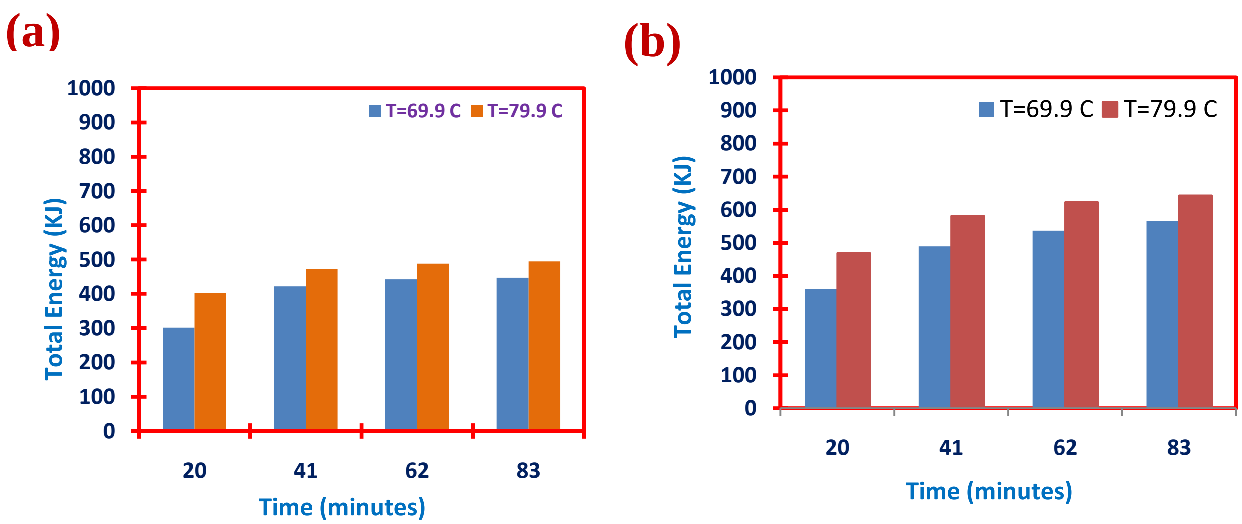

Figure 5.19: Transient evolution of total stored energy (kJ) for two different inner cylinder wall temperatures, $69.9\ ^0C$ and $79.9\ ^0C$ and $Ste_i = 0.113$: (a) plain annulus (b) short-finned annulus.

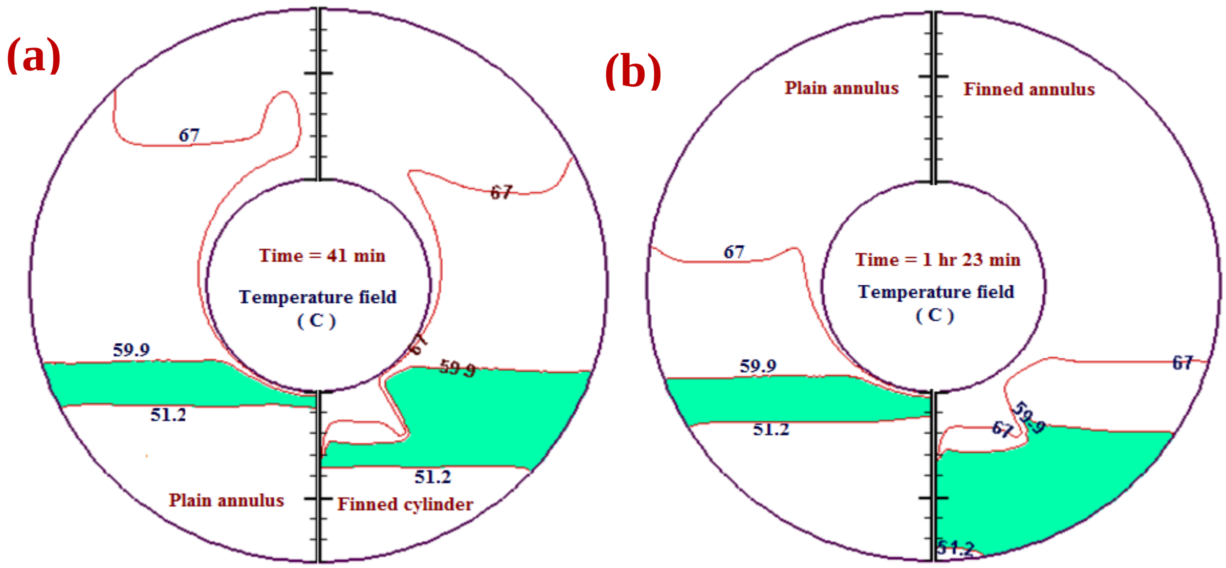

Figure 5.20: For T_{WALL} = 69.9 ^{0}C and Ste_i = 0.113: (a) temperature contours (left) for plain annulus and temperature contours (right) for short-finned annulus at 41 minutes (b) temperature contours (left) for plain annulus and temperature contours (right) for short-fin annulus at 83 minutes.

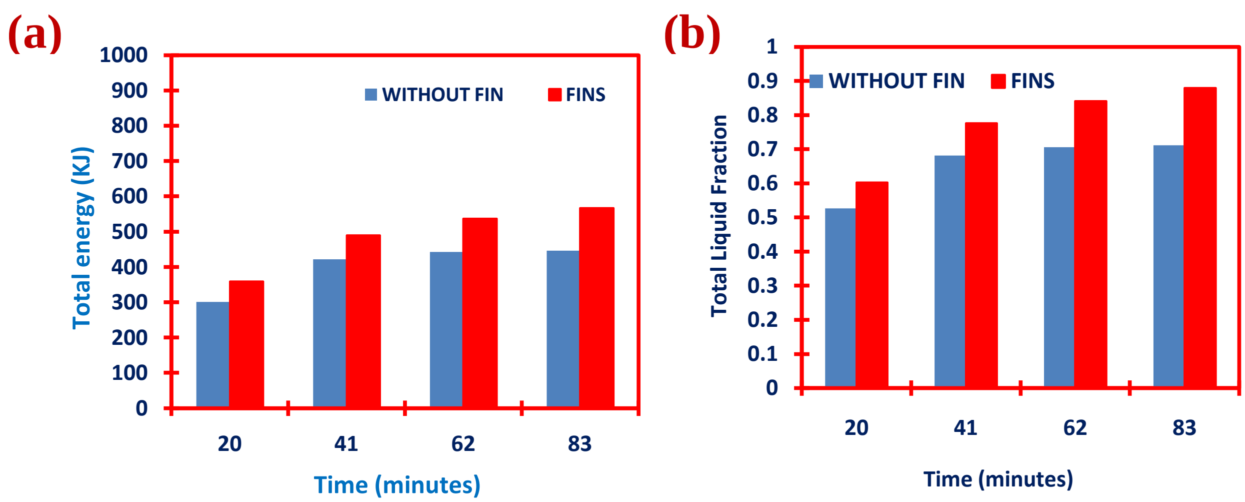

Figure 5.21: (a) Comparison between the plain and short-finned annuli in terms of transient evolution of total stored energy (kJ) at T_{WALL} = 69.9^{0}C and Ste_i = 0.113. (b) Comparison between the plain and short-finned annuli in terms of total liquid fraction at T_{WALL}= 69.9^{0}C and Ste_i = 0.113.

CHAPTER – SIX

Concluding Remarks and Suggestions for Future Work

6.1 Overall Conclusions

A computational model for the prediction of the thermal energy storage characteristics of a commercial paraffin wax during melting (charging phase) when it is embedded in plain and finned annuli formed between two horizontal concentric cylinders has been presented. The model rests on solving the Navier-Stokes equations and energy equation using a single domain enthalpy-porosity approach. An isothermal condition at the inner cylindrical surface and an adiabatic condition at the outer cylindrical surface of the annulus have been considered. Transient progressions of velocity vector and temperature distribution fields are obtained from the numerical solutions of the governing equations for plain and finned annuli. The obtained results have revealed the conductive and the complex conductive-convective heat transfer phenomena existing in the solid, the mushy zone, and the molten phases, respectively. The performance of the present model is verified with the available experimental findings of natural convection of a single phase fluid in a horizontal cylindrical annulus under steady state condition. The predicted results show good agreement with the experimental results.

Based on the findings of the present computational study of the combined conduction and buoyancy-driven melting of a commercial PCM within plain and finned annuli, the following conclusions are drawn:

1. Initially, with the increase in melting time melting rate is enhanced in all the cases.
2. As the buoyancy-driven convection is strengthened due to the growth of the melt zone, it is observed that melting in the top region of the annulus is much fastest than other regions for both geometries.

3. After a while, the melting response of the PCM is very slow. This is because with the increase in time, the melt temperature reaches very close to the inner cylinder wall temperature thereby reducing the heat transfer rate.

4. The strength of natural convection in the melting process is controlled by the Rayleigh number, as indicated from the pictorial views of the flow patterns where it is seen that the overall convective effects change markedly with the change in Rayleigh numbers. An increase in Rayleigh number leads to the increase of the thermal efficiency for both plain and finned annuli at each instant of time.

5. The computational results show that for various values of the sub-cooling parameter, the efficiency of the heat exchanger is enhanced compared to the case when the initial temperature of the PCM is at the solidus temperature, which is true for both plain and finned annuli.

6. At the later part of the melting process only conduction takes place in the lower part of the plain annulus. This makes the melting process very slow and as a result the development of melting zone is nearly stopped. The complex nature of the melting process for the concentric horizontal plain annulus is further aggravated due to the fact that the thermal conductivity of the commercial PCM used in this study is very low.

7. The high thermal conductivity aluminum fins at the lower part of the annulus play an important role in the melting process by generating strong convective and conductive modes of heat transfer near the bottom of the annulus. The finned cylinder, with identical boundary conditions as the plain annulus promote more heat transfer and bring about totally different melt flows and melting patterns. The presence of fins increased the thermal efficiency of the heat exchanger by increasing the melting rate of the PCM compared to the plain geometry.

8. When fin height is taken into consideration, it is observed that at the beginning of the melting process up to a certain time, the short fins show a better performance than the longer fins. If the cost of the fins is a concern, the above aspect of the melting process should be taken into consideration in designing a finned annulus. For shorter fins, due to the limited blockage, the convective melt flow between the fins is not hindered and a

good mixing of the melt between the top and bottom parts of the annulus still prevails. For a larger fin height, the flow blockage is higher and as a result initially the longer finned geometry is not able to open a flow channel in the solid PCM existing between the top and bottom zones of the annulus. As melting proceeds, melts overcome this barrier in the long-finned annulus and shows a better performance than the short finned geometry. Thus, overall the long-finned annulus stores more thermal energy during the charging process compared to the short-finned annulus. When the fin cost is of concern, the short-finned geometry is more advantageous than the long-finned geometry for the higher initial rate of melting.

9. From this study, it is revealed that for a horizontal cylindrical storage system a good way to enhance the latent heat thermal storage capacity is by placing long fins with high thermal conductivity at the lower part of the annulus.

6.2 Contributions to Knowledge

The following aspects of the present numerical modeling study concerning a double-pipe LETES system can be considered new:

1. To the best of the author's knowledge, the melting behavior of a commercial PCM in a horizontal cylindrical annulus has not been studied before either experimentally or numerically.
2. The melting characteristics of a PCM, either pure or reagent grade, in a cylindrical annulus with strategically placed longitudinal radial fins on the outer surface of the inner cylinder has not been studied earlier.
3. A comparative study with regard to the thermal energy storage efficiency of a plain versus finned annuli filled with a commercial PCM is a novel undertaking.
4. This study revealed for the first time the complex nature of the buoyancy-driven melting heat transfer in a partially finned annulus filled with an impure PCM.

6.3 Suggested Future Work

In order to increase the thermal storage efficiency, a number of possible modifications and extensions of the double-pipe LHTES system are suggested below:

1. High porosity and high thermal conductivity solid matrix should be considered in the lower part of the annulus to improve the thermal performance of a PCM energy storage system.
2. The implications of both local thermal equilibrium and non-equilibrium assumptions should be compared if high a thermal conductivity solid matrix is used in the lower part of the annulus.
3. The present study is restricted for a fixed value of the diameter of the inner pipe and also for a fixed value of the diameter ratio of the outer to the inner pipes. The energy storage efficiency should be further studied by varying the above two geometrical parameters of the problem.
4. Both melting (charging) and solidification (discharging) cycles should be consecutively considered to establish the overall thermal energy storage performance of the system.
5. The vertical orientation of the double-pipe LHTES system should be studied and the energy storage efficiency should be compared with the horizontal LHTES system.
6. In order to establish the effects of the inlet temperature and mass flow rate of the heat transfer fluid (HTF) through the inner pipe, the convective melting process in the annulus should be considered as a conjugate fluid flow and phase-change heat transfer problem.
7. With regard to the energy storage efficiency, an interesting numerical exercise would be to investigate two parallel (half length and equal heat capacity) LHTES instead of a one long LHTES.
8. From the energy storage point of view it would be interesting to see the outcome of placing a high melting point PCM near the inner cylinder and a lower melting point PCM in series between the first PCM and the outer wall of the annulus.
9. An interesting numerical undertaking would be to use two immiscible PCMs, one having a lower melting point and a higher density compared to the other, which will fill the

annulus gap with the lower melting point PCM at the bottom and the higher melting point PCM at the top portion of the annulus.

References

Abhat, A. “ Low temperature latent heat thermal energy storage system: Heat storage materials”. Solar Energy, Vol. 30(4), pp. 313-332, 1983.

Adetutu, O. and Prasad, V. “Effects of buoyancy on melting in a horizontal cylinder”, in: Transport Phenomena in Materials Processing and Manufacturing, HTD, Vol. 196, ASME, pp.125-134, 1992.

Agyenim, F., Eames, P., and Smyth, M. ‘A comparison of heat transfer enhancement in a medium temperature thermal energy storage heat exchanger using fins”. Solar Energy, Vol. 83, pp. 1509-1520, 2009.

Balikowski, J. R. and Mollendort, J. C. “Performance of phase change materials in a horizontal annulus of a double-pipe heat exchanger in a water-circulating loop”, Journal of Heat Transfer, Vol. 129, pp.265–271, 2007.

Brent, A. D., Voller, V. R. and Reid, K. J. "Enthalpy-porosity technique for modelling convection-diffusion phase-change: application to the melting of a pure metal”, Num. Heat Transfer, Vol. 13, pp.297-318, 1988.

Brooks, A. N. and Hughes, T. J. R. “Streamline upwind/Petrov-Galerkin formulations for convection dominated flows with particular emphasis on the incompressible Navier-Stokes equations”, Comp. Meth. Appl. Mech. Eng, Vol. 32, pp.199-259, 1982.

Cheddadi, A., Caltagirone, J. P., Mojtabi, A. and Vafai, K. “Free two-dimensional convective bifurcation in a horizontal annulus”, J. Heat Transfer, Vol. 114, pp. 99-106, 1992.

Chow, L. C., Zhong, J. K. and Beam, J. E. “Thermal conductivity enhancement for phase change storage media”, Int Commun Heat Mass Transfer, Vol.23, pp.91–100, 1996.

Chung, J. D., Lee, J. S. and Yoo, H. "Thermal instability during the melting process in an isothermal heated horizontal cylinder". Int. J. Heat Mass Transfer, Vol. 40, No. 16, pp.3899-3907, 1997.

Das, S. and Dutta, T. K. "Mathematical modeling and experimental studies on solar energy storage in a phase change material", Solar Energy, Vol. 51, pp.305-312, 1993.

Date, A. W. "A strong enthalpy formulation for the Stefan problem", Int. J. Heat Mass Transfer, Vol. 34, No. 9, pp. 2231-2235, 1991.

Devahastin, S., Siow, S. L. and Mujumdar, A. S. "Effect of inclination on free convective heat transfer during melting of a phase change material in a rectangular enclosure", Applied Mechanics and Engineering, Vol. 3, pp.491-515, 1998.

Dincer, I. and Rosen, M. (Editors)."Thermal energy storage systems and applications, Chap-7: Modeling of latent heat storage systems". New York, Wiley, 2003.

Dutta, R., Atta, A. and Dutta, T. K. "Experimental and numerical study of heat transfer in horizontal concentric annulus containing phase change material" , The Canadian Journal of Chemical Engineering, Vol. 86 pp.700-710, 2008.

Eftekhar, J., Sheikh, A. H. and Lou, D. Y. S. "Heat transfer enhancement in a paraffin wax thermal storage system", J Solar Energy Eng., Vol 106, pp.299–306, 1984.

Fant, D. B., Prusa, J. and Rothmayer, A. P. "Unsteady multicellular natural convection in a narrow horizontal cylindrical annulus, J. Heat Transfer, Vol. 112, pp. 379- 387, 1990.

Farid, M. M., Khudhair, A. M., Razack, S. A. K. and Al-Halliaj, S. A. " A review on phase change energy storage materials and applications". Energy Convers. Manage., Vol. 45, pp. 1593-1615, 2004.

Fath, H. E. S. "Heat exchanger performance for latent heat thermal energy storage system", Energy Conservation & Management, Vol. 31, No.2, pp.149-155, 1991.

Farinas, M. I., Garon, A. and Katia, S. L. "Study of heat transfer in a horizontal cylinder with fins", Rev Gen Therm, Vol. 36, pp. 398-410, 1997.

Gong, Z .X. and Mujumdar, A. S. "Flow and heat transfer in convection-dominated melting in a rectangular cavity heated from below". Int. J. Heat Mass Transfer, Vol. 41, pp. 2573-.80, 1998.

Hale, N.W. and Viskanta, R. "Solid-liquid phase change heat transfer and interface motion in materials cooled or heated from above or below". Int. J. Heat Mass Transfer, Vol. 23, pp.283-292, 1980.

Hendra, R., Hamdani, T. M., Mahlia, I. and Masjuki, H. H. "Thermal and melting heat transfer characteristic in a latent heat storage system using mikro". Applied Thermal Engineering, Vol. 25, pp.1503-1515, 2005.

Hessami, M. A., Pollard, A. and Rowe, R. D. "Numerical calculation of natural convective heat transfer between horizontal concentric isothermal cylinders-effects of the variation of the fluid properties", J. Heat Transfer, Vol. 106, pp. 668-671, 1984.

Ho, C. J. and Lin, K. C. "Outward melting in a cylindrical annulus", Transactions of the ASME, Vol. 108, pp.240–245, 1986.

Hu, H. and Argyropoulos, S. A. " Mathematical modeling of solidification and melting: A review". Modelling and Simulation in Materials Science and Enginering, Vol. 4(4), pp. 371-396, 1996.

Ismail, K. A. R., Alvies, C. L. F. and Modest, M. S. " Numerical and experimental study on the solidification of PCM around a vertical axially finned isothermal cylinder". Applied Thermal Engineering, Vol. 21, pp. 53-77, 2001.

Ismail, K. A. R. and da Silva, M. D. E. “Melting of PCM around a horizontal cylinder with constant surface temperature”, International Journal of Thermal Sciences, Vol. 42, pp.1145-1152, 2003.

Jewgadheeswaran, S. and Pokehar, S. D. “Performance enhancement in latent heat thermal storage system: A review”. Renewable and Sustainable Energy Reviews, Vol. 13, pp. 2225-2244, 2009.

Khillarkar, D. B., Gong, Z. X. and Mujumdar, A. S. “Melting of a phase change material in concentric horizontal annuli of arbitrary cross-section”, Applied Thermal Engineering, Vol. 20, pp.893-912, 2000.

Kim, C. J. and Kaviany, M. “A numerical method for phase-change problems with convection and diffusion, Int. J. Heat Mass Transfer, Vol. 35, pp. 457- 467, 1992.

Kim, C. J. and Ro, S. T. “Numerical investigation of bifurcative natural convection in air-filled horizontal annulus”, Proc. 10th Int. Heat Transfer Conf., pp. 85- 90, 1994.

Kuehn, T. H. and Goldstein, R. J. “An experimental and theoretical study of natural convection in the annulus between horizontal concentric cylinders”, J. Fluid Mech.,Vol. 74, pp. 695- 719, 1976.

Kuehn, T. H. and Goldstein, R. J. “An experimental study of natural convection heat transfer in concentric horizontal cylindrical annuli”. J. Heat Transfer, Vol. 100, pp. 635-640, 1978.

Lacoris, M., “Study of the heat transfer behavior of a latent heat thermal energy storage unit with finned tube”, Int. J. Heat Mass Transfer, Vol. 36, No. 8, pp. 2083-2092, 1993a.

Lacroix, M. “Numerical simulation of a shell and tube latent heat thermal energy storage unit”. Solar Energy, Vol. 50(4), pp. 357-367, 1993b.

Liu, Z. and Ma, C. "Numerical analysis of melting with constant heat flux heating in a thermal energy storage system", Energy Conversion Manage,Vol.43, pp. 2521–38, 2002.

Liu, Z., Sun, X. and Ma, C. "Experimental investigations on the characteristics of melting processes of stearic acid in an annulus and its thermal conductivity enhancement by fins". Energy Conservation & Management, Vol. 46, pp. 959-969, 2005.

Mbaye, M. and Bilgen, E. " Phase change process by natural convection-diffusion in rectangular enclosures". Heat and Mass Transfer, Vol. 37, pp. 35-42, 2001.

Medrano, M., Yilmaz, M. O., Nogues, M., Martorell, I., Roca, J. and Cabeza, L. F. "Experimental evaluation of commercial heat exchangers for use as PCM storage systems" . Applied Energy, Vol. 86, pp.2047-2055, 2009.

Mesalhy, O., Lafdi, K., Elgafy, A. and Bowman, K. "Numerical study for enhancing the thermal conductivity of phase change material (PCM) storage using high thermal conductivity porous matrix", Energy Conversion and Management, Vol. 46, pp.847-867, 2005.

Minakawa, S., Samarasekera, I. V. and Weinberg, F. "Centerline porosity in plate castings". Metall. Trans., Vol. 16B, pp. 245-255, 1987.

Ng, K. W., Gong, Z. X. and Mujumdar, A. S. "Heat transfer in free convection-dominated melting of a phase change material in a horizontal annulus", Int. Comm. Heat Mass Transfer, Vol. 25, No. 5, pp.631-640, 1998a.

Ng K. W., Devahastin, S. and Mujumdar, A. S. "Free convective melting of a phase change material in a horizontal cylindrical annulus", Transactions TSTU, Vol. 4, pp.40-52, 1998b.

Padmanabban, P. V. "Outward phase change in a cylindrical annulus with axial fins on the inner tube", Int. J. Heat Mass Transfer, Vol. 29, No. 12, pp. 1855-1866, 1986.

Patankar, S. V. “Numerical heat transfer and fluid flow”, Hemisphere/McGraw-Hill, Washington, 1980.

Rao, Y. F., Miki, Y., Fukuda, K., Takata, Y. and Hasegawa, S. “Flow patterns of natural convection in horizontal cylindrical annuli”, Int. J. Heat Mass Transfer, Vol. 28, pp.705-714, 1985.

Regin, A. F., Solanki, S. C. and Saini, J. S. “Heat transfer characteristics of thermal energy storage system using PCM capsules: Areview”. Renewable and Sustainable Energy Reviews, Vol. 12, pp. 2438-2458, 2008.

Reiger, H., Projahn, U. and Beer, H. “Analysis of the heat transport mechanism during melting around a horizontal circular cylinder”. Int. J. Heat Mass Transfer, Vol. 25, pp.137-147, 1982.

Sari, A. and Kaygusuz, K. “ Thermal performance of myristic acid as a phase change material for energy storage application”, Renewable Energy, Vol.24, pp.303–17, 2001.

Sari, A. and Kaygusuz, K. “Thermal and heat transfer characteristics in a latent storage system using lauric acid”, Energy Conversion Manage, Vol. 43, pp.2493–507, 2002.

Savnarskil, A. A., Vabishcherich, P. N., Iliev, O. P. and Ghurbanov, A. G. “Numerical simulation of convection/diffusion phase change problems: A review”. Int. J. Heat Mass Transfer, Vol. 36(17), pp. 4095-4106, 1993.

Smith, R. N. and Koch, J. D. “Numerical solution for freezing adjacent to a finned surface”, Proceedings of Seventh International Heat Transfer Conference, U. Grigulf, et. al., eds., Munchen, Germany, pp. 69-74, 1982.

Sparrow, E. M., Larson, E. D. and Ramsey, J. W. “Freezing on a finned tube for either conduction controlled or natural convection controlled heat transfer”, Int. J. Heat Mass Transfer, Vol. 24, pp. 273-284, 1981.

Swaminathan, C. R. and Voller, V. R. “On the enthalpy method”, Int. Num. Meth. Heat Fluid Flow, Vol. 3, pp. 233-244, 1993.

Swaminathan, C. R. and Voller, V. R. “Towards a general numerical method for analysis of solidification systems”. Int. J. Heat Mass Transfer, Vol. 40, pp. 2859-2868, 1997

Tong, X., Khan, J. A. and Amin, M. R. “Enhancement of heat transfer by inserting a metal matrix into a phase change material”. Numerical Heat Transfer, Part A, Vol. 30, pp.125–141, 1996.

Vafai, K. and Ettefagh, J. “An Investigation of Transient Three-Dimensional Buoyancy-Driven Flow and Heat Transfer in a Closed Horizontal Annulus”, Int. J. Heat Mass Transfer, Vol. 34, pp. 2555- 2569, 1991.

Velraj, R., Seeniraj, R. V., Hafner, B., Faber, C. and Schwarzer, K. “Experimental analysis and numerical modelling of inward solidification on a finned vertical tube for a latent heat storage unit”, Solar Energy, Vol. 60(5), pp.281–290, 1997.

Velraj, R., Seeniraj, R. V., Hafner, B., Faber, C. and Schwarzer, K. “Heat transfer enhancement in a latent heat storage system”, Solar Energy, Vol.65(3), pp.171–80, 1999.

Viskanta, R. “ Natural convection in melting and so9lidification”. S. Kakac et al. (Editors). Natural Convection: Fundamentals and Applications, Hemisphere, Washington, DC, pp. 845-877, 1995.

Viskanta, R. “Heat transfer during melting and solidification of metals”, Transactions of the ASME, J. Heat Transfer, Vol. 110, pp.1205-1219, 1988.

Voller, V. R. “Fast implicit finite difference method for the analysis of phase change problems”, Numerical Heat Transfer, Part. B, Vol. 17, pp. 155-169, 1990.

Voller, V. R. and Prakash, C. “A fixed grid numerical modelling methodology for convection-diffusion mushy region phase-change problems”, Int. J. Heat Mass Transfer, Vol.30, pp. 1709-1719, 1987.

Voller, V. R. and ., Swaminathan, C. R. “General source based method for solidification phase change”. Numerical Heat Transfer B-Fundamentals, Vol. 19 (2), pp. 175-189, 1991.

Voller, V. R., Swaminathan, C. R. and Thomas, B. G. “Fixed grid techniques for phase change problems: A review”. Int. J. Num. Methods in Eng., Vol. 30 (4), pp. 875-898, 1990.

Xavier, P., Regis, O. and Sylvain, M. “Parafin/porous-graphite-matrix composite as a high and constant power thermal storage material”, Int. J. Heat Transfer, Vol. 44, pp.2727-37, 2001.

Yang, H. Q., Yang, K. T. and Lloyd, J. R. “Natural convection suppression in horizontal annuli by azimuthal baffles”, Int. Heat Mass Transfer, Vol. 10, pp. 2123-2135, 1988.

Zalba, B., Marin, J. M., Cabeza, I. F. and Mealing, H. “ Review on thermal energy storage with phase change materials, heat transfer analysis and applications”. Appl. Therm. Eng., Vol. 23, pp. 251-283, 2003.

Zhang, Y. and Faghri, A. “Heat transfer enhancement in latent heat thermal energy storage system by using longitudinally finned tube’. Int. J. Heat Mass Transfer, Vol. 39(5), pp. 3165-3173, 1996.